

**Novel consolidation methods of Fe-base oxide dispersion strengthened powders produced  
via gas-atomization reaction synthesis**

by

**Rebecca Fer**

A thesis submitted to the graduate faculty  
in partial fulfillment of the requirements for the degree of

**MASTER OF SCIENCE**

Major: Materials Science and Engineering

Program of Study Committee:  
Iver E. Anderson, Major Professor  
Scott Chumbley  
Peter Collins

The student author, whose presentation of the scholarship herein was approved by the program of study committee, is solely responsible for the content of this thesis. Graduate College will ensure this thesis is globally accessible and will not permit alterations after a degree is conferred.

Iowa State University

Ames, Iowa

2020

Copyright © Rebecca Fer, 2020. All rights reserved.

## **DEDICATION**

For my husband Sam, without whom I never would have completed graduate school.  
Also to my parents, Bruce and Shaleigh, for teaching me that if I'm going to do something, to  
always do my best. That's all they have ever asked.

## TABLE OF CONTENTS

	Page
LIST OF FIGURES .....	vi
LIST OF TABLES .....	x
NOMENCLATURE .....	xi
ACKNOWLEDGMENTS .....	xiii
ABSTRACT.....	xiv
CHAPTER 1. INTRODUCTION .....	1
1.1 Thesis Organization .....	1
1.2 Purpose of Study.....	1
CHAPTER 2. WORLD ENERGY CONCERNS AND MATERIALS FOR NUCLEAR ENERGY DEVELOPMENT .....	4
2.1 World Energy Concerns .....	4
2.2 Nuclear Power Reactors .....	7
2.2.1 Uranium Fuel.....	7
2.2.2 Current Reactors (Generation II-III) .....	9
2.2.2.1 Loss of Cooling Accidents .....	10
2.2.2 Generation IV Reactors .....	13
CHAPTER 3. OXIDE DISPERSION STRENGTHENED ALLOYS .....	15
3.1 Strengthening Mechanism .....	15
3.2 Creep Resistance.....	19
3.3 Radiation Resistance.....	23
3.4 Brief overview of Fe-ODS alloys .....	25
3.4.1 FeCrAl Alloys .....	27
3.4.2 NFAs .....	28
3.5 Manufacturing .....	29
3.5.1 Mechanically Alloying .....	29
3.5.2 Traditional Consolidation.....	31
3.5.3 Traditional TMT and machining .....	31
CHAPTER 4. GAS ATOMIZATION REACTION SYNTHESIZED POWDERS .....	32
4.1 GARS Method.....	33
4.2. Previous GARS Consolidation Methods .....	37
4.2.1 Previous consolidation of GARS CR-96 – 166 alloys .....	37
4.2.2 Previous consolidation of GARS CR-198 and CR-204 alloys .....	38

CHAPTER 5. AI VS. NON-AI CONTAINING GARS ALLOY VHP CONSOLIDATION STUDY .....	41
5.1 Background.....	41
5.1.1 Vacuum Hot Press Consolidation.....	41
5.2 Experimental Methods.....	42
5.3 Results .....	44
5.3.1 VHP sample generation.....	44
5.3.2 VHP sample hardness.....	45
5.3.2 Microscopy .....	46
5.4 Discussion.....	52
5.4.1 VHP sample generation.....	52
5.4.2 VHP sample microhardness .....	52
5.4.3 Future Processing Options.....	54
5.4.3 VHP sample microscopy .....	54
5.5 Conclusion .....	55
CHAPTER 6. COLD SPRAY CONSOLIDATION STUDY.....	57
6.1 Background.....	57
6.1.1 Cold Spray Deposition .....	57
6.2 Experimental Methods.....	59
6.2.1 CS Sample Generation .....	59
6.2.2 Microscopy and Microhardness .....	60
6.2.2.1 Deadweight annealing.....	60
6.2.2.1 Differential Scanning Calorimetry .....	60
6.3 Results .....	61
6.3.1 CS Sample Generation .....	61
6.3.2 Microscopy and microhardness.....	63
6.3.2.1 Deadweight annealing.....	65
6.3.2.2 Differential Scanning Calorimetry.....	67
6.4 Discussion.....	70
6.4.1 Cold Spray Coupon Generation .....	70
6.4.2 Microscopy and Microhardness .....	71
6.4.2.1 Vickers Microhardness .....	71
6.4.3 DSC Analysis .....	73
6.5 Conclusion .....	75
CHAPTER 7. CONLCUSIONS .....	77
REFERENCES .....	79
APPENDIX. STANDARD OPERATING PROCEDURE FOR CENTORR HOT PRESS .....	84
Introduction .....	84
Important Notes: .....	84
Die Set Requirements .....	85
Graphite Requirements.....	85
Maximum Die Pressure and Applied Pressure Conversion .....	86
Vacuum System Operation.....	88

Opening Furnace Chamber.....	88
Closing Furnace Chamber.....	89
Furnace Operation .....	89
Cu and Sb Calibration .....	89
Furnace Operation and Programming .....	91
Die Pressing.....	91
Loading and Unloading Samples .....	91
Hydraulic System Operation .....	91
Alignment and Troubleshooting.....	92

## LIST OF FIGURES

	Page
Figure 2.1: U.S. electricity sources as of 2019. From [13] .....	4
Figure 2.2: Emissions intensity by energy source in g/kWh [16] .....	6
Figure 2.3: U-235 atoms split with the addition of a neutron starting a chain reaction. Additional nuclear fission products not shown. From [19]. .....	8
Figure 2.4: Schematic of a PWR and a BWR, from [17] .....	10
Figure 2.5: Schematic of Zircaloy fuel rod containing fuel pellets. Adapted from [21] .....	11
Figure 2.6: Thermal power and cumulative energy due to decay heat and Zr-base cladding oxidation. From [23] with permission from [24] .....	12
Figure 2.7: Parabolic oxidation rate for various cladding materials and resulting oxide in steam at elevated temperatures. From [23] .....	12
Figure 3.1: Random obstacles throughout matrix material holding up dislocation motion, where L denotes particle-particle spacing, and bending angle $\phi$ defines the strength of the obstacle [26] .....	16
Figure 3.2: The Orowan model for hard particle obstruction of edge dislocation motion [28] ....	17
Figure 3.3: Weak obstacle particle shear or dislocation bowing at two critical radii and two volume fractions of precipitates ( $f_2 > f_1$ ) [28] .....	18
Figure 3.4: Creep strain vs. time to failure for different temperatures at a constant stress [28] .....	19
Figure 3.5: (a) Schematic of cascade production of vacancies and self-interstitial atoms (SIA), and (b) SIA recombining with diffusing vacancy and vacancy trapped at precipitate. Adapted from [1] .....	25
Figure 3.6: Effect of Al additions on a-a' phase boundary for Fe-Cr binary alloy. From [39] .....	28
Figure 3.7: Example of a traditional manufacturing route for ODS alloys [43]. Oxide additions vary with alloy family to achieve the desired precipitate phase. ....	29
Figure 3.9: Schematic showing deformation behavior of starting metal powders during mechanical alloying [42] .....	30

Figure 5.1: Cross section of graphite die assembly inside of induction heated vacuum furnace chamber, with hydraulically activated rams. From [42].	41
Figure 5.2: Vickers hardness measurement locations for GARS VHP samples for the base (a) and the interior side (b).	43
Figure 5.3: VHP samples generated at 850°C under 100MPa pressure (a) CR-200 -53/+20 um powder and (b) CR-204 -45/+20um powder. The alumina spacer still attached to VHP-012 when the image was taken was covered for image clarity.	45
Figure 5.4: Vickers microhardness of CR-200 alloy as-pressed and after heat treatment.	45
Figure 5.5: Vickers hardness of CR-204 alloy as-pressed and after heat treatment	46
Figure 5.6: As-atomized CR-200 powder including (a) exterior powder surface morphology and (b) BSE image showing interior segregation of Y & HF along cell boundaries (yellow arrows).	46
Figure 5.7: As-atomized CR-204 powder including (a) exterior powder surface morphology and (b) BSE image showing interior segregation of Hf and Y along cell boundaries (yellow arrows). Smaller particle to the right to the larger has significantly less segregation network.	47
Figure 5.8: As-VHP consolidated microstructures at (a,c) 650x and (b,d) 2000x. Images taken on the base of the VHP sample, pressing direction coming out of the page.	47
Figure 5.9: Resulting microstructures at 650x for CR-200 and CR-204 powders after VHP consolidation and vacuum heat treatment at (a,b) 1100°C for 2.5h (d,e) 1200°C for 2.5h, and (e,f) 1200°C for 12hrs.	48
Figure 5.10: Example EDS output for CR-204 1100C for 2.5hr sample. Scale of image matches distance on the x-axis of the counts graph	50
Figure 5.11: Suspected cracking of CR-204 post VHP and HT at 1200°C for 12h.	51
Figure 5.12: Relative alpha-Fe atomic diffusion coefficient for alloying additions. From [9]	53
Figure 6.1: Schematic of CS deposition process [55]	58
Figure 6.2: Schematic of five hardness measurements taken along the top face of sample cut from as-CS specimen.	60
Figure 6.3: Heating path for DSC of as-CS deposited GA-1-200 samples. This path was repeated twice for each sample.	61

Figure 6.4: As-deposited cold sprayed sample of GARS powder onto aluminum substrate, (a) showing top down view of deposit and slice off of deposit, and (b) showing cross sectioned surface as-cut [54] .....	62
Figure 6.5: GA-1-200 CS Deposited Sample Porosity Gradient. Sections 1-4 are 1 mm in height, section 5 is 0.73 mm high.....	63
Figure 6.6: Backscattered SEM image of as-CS deposited CR-200 powder. Deposition direction points down in plane with the page [54] .....	64
Figure 6.7: BSE SEM image of deformed CR-200 alloy powder particle in the as-CS deposited sample. Deposition direction points down in plane with the page [54] .....	64
Figure 6.8: EBSD of as-CS grains from CR-200.....	65
Figure 6.9: Reference location for the annealed EDS/EBSD data. Scale bar is 25 $\mu$ m.....	65
Figure 6.10: EBSD map and EDS series spectra for annealed CR-200 sample. W, Cr, and C series were also captured, but showed even distribution across the scan, and thus are not included here.....	66
Figure 6.11: Post-CS annealed BSE image with EDS spectra noted.....	66
Figure 6.12: CR-200 As-CS deposited, DSC sample 1 with baseline subtracted, entire heating path. Suspected dislocation recovery window and curie temperature marked .....	67
Figure 6.13: CR-200 As-CS Deposited, DSC sample 1 with baseline subtracted, room temperature to 600°C. Suspected dislocation recovery and recrystallization/grain growth marked, in addition to Tc .....	68
Figure 6.14: CR-200 As-CS DSC sample with baseline subtracted, entire heating path. Suspected dislocation recovery window and curie temperature marked.....	68
Figure 6.15: CR-200 As-CS Deposited, DSC sample with baseline subtracted, room temperature to 600C. Suspected dislocation recovery and recrystallization/grain growth marked, in addition to Tc .....	69
Figure 6.16: CR-200 As-CS Deposited DSC sample 2 heating and cooling for runs 1 and 2. There is no noise in the cooling curve that matches suspected the recovery and recrystallization/grain growth from the heating curve. Tc is present in the heating and cooling curves. ....	69



Figure 6.17: Gas manifold pressure vs. gas velocity for He, N <sub>2</sub> and Ar [58] .....	70
Figure 6.18: Vickers microhardness of CR-200 alloy as-CS and as-annealed .....	72

## LIST OF TABLES

	Page
Table 2.1: Commercial nuclear power plants in commercial and operational as of April 2020, adapted from [17] .....	9
Table 2.2: Generation IV reactor designs under development by GIF. Adapted from [17] .....	13
Table 3.1: Strengthening mechanisms in metals [9] .....	15
Table 3.2: Creep stress exponent values per dominating creep mechanism [29] .....	20
Table 3.3: Defect production timescales for irradiated metals. From [34] .....	23
Table 3.4: Compositions of some commercially available Fe-ODS alloys, from [9] .....	26
Table 3.5: Compositions of 14 and 12YWT alloys .....	26
Table 4.1: Brief overview of consolidation experiments using CR-96 to CR-166 Fe-ODS GARS precursor powders .....	37
Table 4.1 continued: Brief overview of consolidation experiments using CR-96 to CR-166 Fe-ODS GARS precursor powders .....	38
Table 4.2: Measured Auger oxide thickness of CR-198 and CR-204. From [10] .....	39
Table 5.1: CR-200 and CR-204 as-atomized compositions .....	42
Table 5.2: Heat Treatment Schedule for CR-200 and Cr-204 alloy quarters (Q1-4) after VHP consolidation .....	44
Table 5.3: Density of VHP samples after VHP and heat treatment, as calculated from stitched base images via ImageJ threshold analysis. ....	49
Table 6.1: GA-1-200 CS deposited sample porosity gradient by section area .....	63
Table 6.2: Point Spectrum EDS analysis of post-CS annealed microstructure .....	67
Table 0.1: Die wall radius ratios for $Cti$ .....	86
Table 0.2: Applied Pressure vs. HP Line Pressure Gauge .....	87

**NOMENCLATURE**

ATF	Accident Tolerant Fuel
BWR	Boiling Water Reactor
CS	Cold Spray
DSC	Differential Scanning Calorimetry
EBSD	Electron Backscattered Detection
EDS	Energy Dispersive Spectroscopy
EIA	U.S. Energy Information Administration
FeCrAl	Family of alloys containing Fe, Cr, & Al
GARS	Gas Atomization Reaction Synthesis
GIF	Generation IV International Forum
HIP	Hot Isostatic Pressing
HT	Heat Treatment
IEA	International Energy Agency
INCO	International Nickel Company
LANL	Los Alamos National Laboratory
LOCA	Loss of Cooling Accident
LWR	Light Water Reactor
MA	Mechanically Alloyed
NFA	Nano-Ferritic Alloys
ODS	Oxide Dispersion Strengthened
OIM	Orientation Imaging Microscopy
ORNL	Oak Ridge National Laboratory

PKA	Primary knock-on atom
PWR	Pressurized Water Reactor
SEM	Scanning Electron Microscopy
SIA	Self Interstitial Atom
TEM	Transmission Electron Microscopy
TMT	Thermal-mechanical Treatment

## ACKNOWLEDGMENTS

This work was supported by the U.S. Department of Energy (DOE) Fossil Energy and Nuclear Energy funding under contract number DE-AC02-07CH11358. Ames Laboratory is operated for the DOE by Iowa State University. The document number assigned to this thesis is IS-T3280.

I would like to thank my committee chair, Iver Anderson, and my committee members, Scott Chumbley, and Peter Collins, for their guidance and support throughout the course of this research.

In addition, I would like to thank Tim Eden and Todd Palmer at the Pennsylvania State University Applied Research Laboratory for cold spray depositing samples for the purpose of this thesis.

Lastly, I would also like to thank my friends & colleagues in the Powder Group. Thank you all for making research fun. I'm grateful to have had the chance to be a part of such a wonderful group. I also extend thanks to the MSE department students, faculty, and staff for making my time at Iowa State University a wonderful experience.

## ABSTRACT

Mechanically alloyed Fe-base oxide dispersion strengthened (ODS) alloys are strong candidates for application as drop-in accident tolerant fuel claddings for existing nuclear power plants and as structural materials in Generation IV nuclear power plants due to their retained high temperature strength and corrosion resistance, in addition to their resistance to void swelling and failure under radiative environments. Mechanically alloying (MA) processes for generating Fe-ODS materials require long (40+h) high energy milling times, and the resulting powders may vary in composition from batch to batch due to contamination from milling materials. Gas atomized reaction synthesized (GARS) Fe-ODS precursor powder production offers an alternative higher efficiency method of producing Fe-ODS materials, but so far have only been consolidated via hot isostatic pressing. Novel application of vacuum hot pressing and cold spray deposition are investigated as alternative methods for consolidation of GARS Fe-ODS precursor powders.

Vacuum hot pressing compared the as-pressed microstructures of Al containing GARS Fe ODS precursor powder CR-200 to the non-Al containing CR-204. The powders were pressed under 100MPa load for 4h at 850°C. The as-pressed compacts were not fully sintered and had ~90% density in the as-pressed state. Heat treatment at 1100 and 1200°C for 2.5h and at 1200°C for 12h resulted in development of coarsened IMCs and limited oxide phases primarily located along PPBs. It was determined that both powders show insufficient oxygen content ratios to develop the desired concentration of nano-metric oxide dispersoids. Also, it was determined that before heat treating to initiate the oxygen exchange reaction, VHP samples will need to be further deformed to break up PPBs and introduce greater dislocation densities as nucleation sites for the dispersoid phase.

Cold spray deposition (CS) of CR-200 resulted in generation of a flat test coupon that was sectioned and evaluated. The as-deposited sample had an average of 93% density. Differential scanning calorimetry was used to confirm the presence of stored energy due to plastic deformation from the deposition without the use of transition electron microscopy (TEM) techniques. If CS-deposition is explored in the future for consolidation of these powders, it is recommended that a higher temperature or higher velocity accelerating gas be used for the deposition to promote complete cold welding of the powder particles and resulting higher as-deposited density.

## **CHAPTER 1. INTRODUCTION**

### **1.1 Thesis Organization**

Chapter 1 of this thesis presents an outline of the topics covered in the thesis and introduces the purpose of performing this research. The state of global electricity concerns is also addressed in Chapter 1, and Chapter 2 discusses the state of nuclear power reactors, including the need for Fe-ODS materials in existing and future generation nuclear power reactors. Chapter 3 discusses the strengthening mechanism and creep and radiation resistance of Fe-ODS alloys, and provides a brief history of the alloys, alloy families of interest, and traditional manufacturing methods.

Chapter 4 introduces the gas atomization reaction synthesis (GARS) method of manufacturing Fe-ODS precursor powders and provides a summary of previous consolidation methods and research findings with Fe-ODS GARS alloys. Chapter 5 investigates vacuum hot pressing as a method of consolidating GARS alloys and investigates the effects of aluminum containing versus non-aluminum containing alloy properties. Chapter 6 discusses the outcomes of GARS Fe-ODS consolidation via cold spray deposition and characterizes the properties of a Fe-ODS GARS alloy coupon cold sprayed at Penn State Applied Research Laboratory for this study. Lastly, Chapter 7 presents the overall conclusions from the work.

### **1.2 Purpose of Study**

Fe-base oxide dispersion strengthened (ODS) materials are important for application in advanced and Generation IV nuclear power plants, due to their retained high temperature strength, creep resistance, and resistance to neutron induced void swelling [1-3]. Fe-ODS materials, and the further refined nano-ferritic alloys (NFAs) have a large number density of nano-metric oxides to pin dislocations and fine grain sizes. Traditional methods of



manufacturing Fe-ODS materials include lengthy mechanical alloying (MA) processes for up to 40 hours to sufficiently dissolve refractory oxides (i.e.  $\text{Y}_2\text{O}_3$ ) into ferritic Fe-Cr steels, but MA can introduce contaminants into the powders that has led to research devoted to designing around milling contaminants [4]. Commercially available Fe-ODS products (e.g. MA956) were so costly to manufacture that they are no longer available for purchase. The commercial alloys did not have the refined structures and properties shown by higher purity alloys currently being researched (e.g. 14YWT, ODS FeCrAl) [5]. More cost-effective and reliable methods of preparing a variety of Fe-ODS materials with the desired refined grain structures and fine nano-metric oxides are needed, which inspired the work contained in this thesis

This thesis continues work with the gas atomization reaction synthesis (GARS) method of producing Fe-ODS precursor powders [6-10] that are generated in reactive, oxygen containing atomization gases that oxidize the powder surfaces. The surface oxides preferentially form kinetically favorable Cr-enriched phases. Upon consolidation, the surface oxides are trapped as prior particle boundaries [9]. Elevated temperature heat treatments are used to dissociate the Cr-oxide phases to form more thermodynamically stable oxides, i.e. dispersoid phases via oxygen exchange reactions in which the oxygen diffuses away from the prior particle boundaries to less mobile alloying additions, such as Y and Hf. The thermodynamically stable oxides become the dispersed oxide dispersion phase for the alloy.

Previous studies of the Fe-ODS GARS precursor powders extensively characterized the behavior of the resulting alloy samples from post-hot isostatic press (HIP) consolidation. Alternative consolidation methods novel to Fe-ODS GARS precursor powders, including vacuum hot pressing (VHP) and cold spray (CS) deposition, are the subject of this thesis. A procedure for consolidating Fe-ODS GARS precursor powders via VHP was generated, and the

behavior of Al-vs. non-Al-containing powder compacts post consolidation and heat treatment were evaluated. Next, the Al-containing powder was CS deposited onto a test coupon to test the behavior of Fe-ODS GARS precursor powders during CS deposition, and the ensuing as-deposited and annealed microstructures were evaluated.

## CHAPTER 2. WORLD ENERGY CONCERNS AND MATERIALS FOR NUCLEAR ENERGY DEVELOPMENT

### 2.1 World Energy Concerns

As of 2016, electricity generation was responsible for 42.5% of global CO<sub>2</sub> emissions, and prior to 2020 global electricity demand was projected to increase by 80-130% from 2016 demand by 2050 [11]. Figure 1 shows the distribution of electricity production sources in the U.S. as of 2019 for 4.12 trillion kilowatt-hours of electricity. However, In the face of a global pandemic, electricity demand in 2020 has seen an unprecedented decline with the demand in the first quarter of 2020 being 2.5% less than the first quarter of 2019 [12] . Similarly, global CO<sub>2</sub> emissions were reported as 5% lower in the first quarter of 2020 than in 2019. Global electricity demand is expected to drop by as much as 5% in 2020, which is eight times the effect of the global financial crisis in 2009 [12].

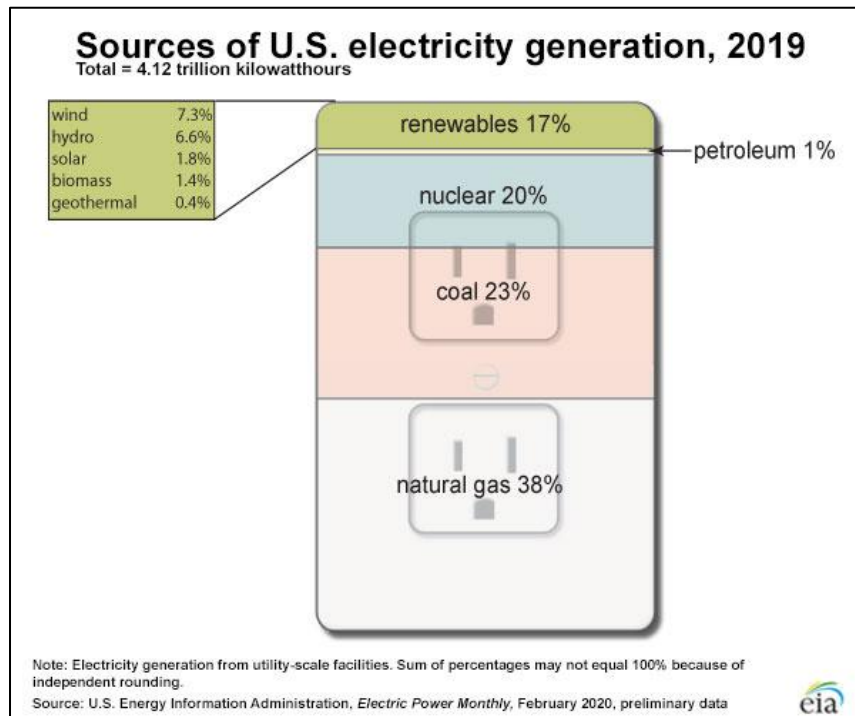


Figure 2.1: U.S. electricity sources as of 2019. From [13]

Although residential electricity demand has increased with stay at home orders, the decline in demand in the services and industry sectors outweighs residential use, leading to an overall demand decrease. Assuming the world returns to “normal” with development and distribution of a vaccine for COVID-19, global energy demand will again be expected to rise [12].

In order to meet the increased demand, new and updated electricity generation sources will be built to increase generation capacity. The International Energy Agency (IEA) has released a sustainable recovery plan to use the unprecedented drop in CO<sub>2</sub> emissions brought about by the global pandemic as “a base to put emissions into structural decline” (Figure 2) [14]. Although the pandemic has temporarily reduced emissions, the cooling effects will be negligible with only  $0.01 \pm 0.005^{\circ}\text{C}$  cooling by 2030 as a direct effect of quarantine without further action [15].

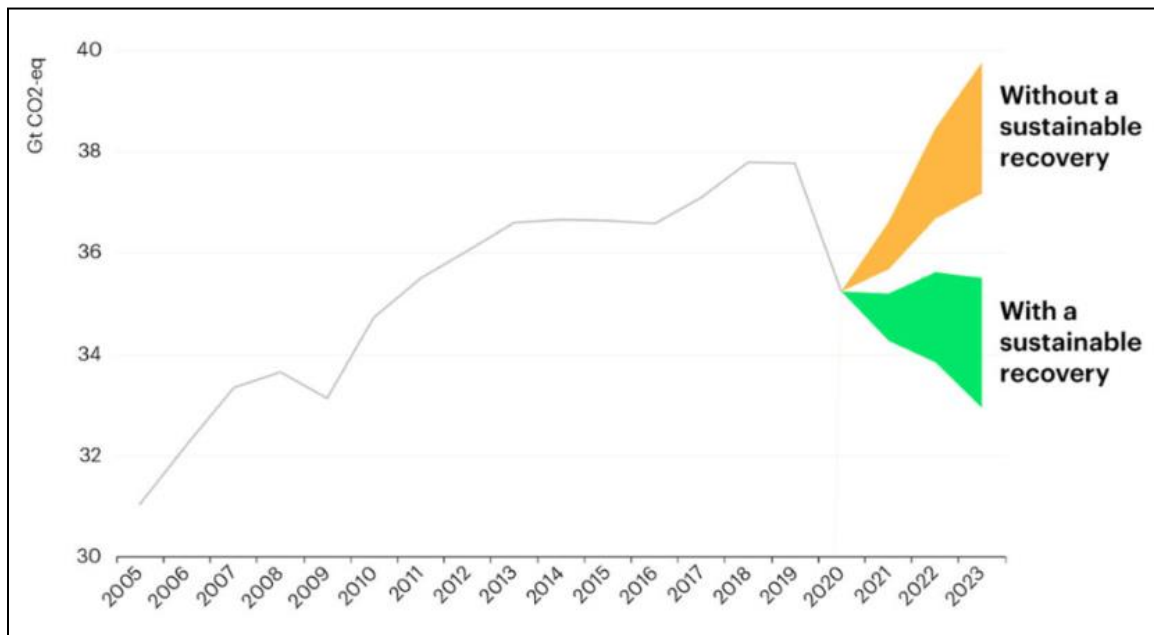


Figure 2.2: Emissions trajectories (green) and without (orange) with the IEA's sustainable recovery plan [12].

As new electricity generation sources are built, there is the opportunity to direct effort to building more sustainable and efficient energy sources with minimal CO<sub>2</sub> emissions, rather than relying on historically dominant sources like coal-fired power plants. Figure 3 shows CO<sub>2</sub> emission intensity by energy source. The IEA's sustainable recovery plan emphasizes investment into new and updated renewable and low-carbon energy source infrastructure for rapid job creation post-quarantine. Together nuclear and hydroelectric power accounted for 30% of world electricity generation, or 70% of the world's low carbon power in 2019 [14].

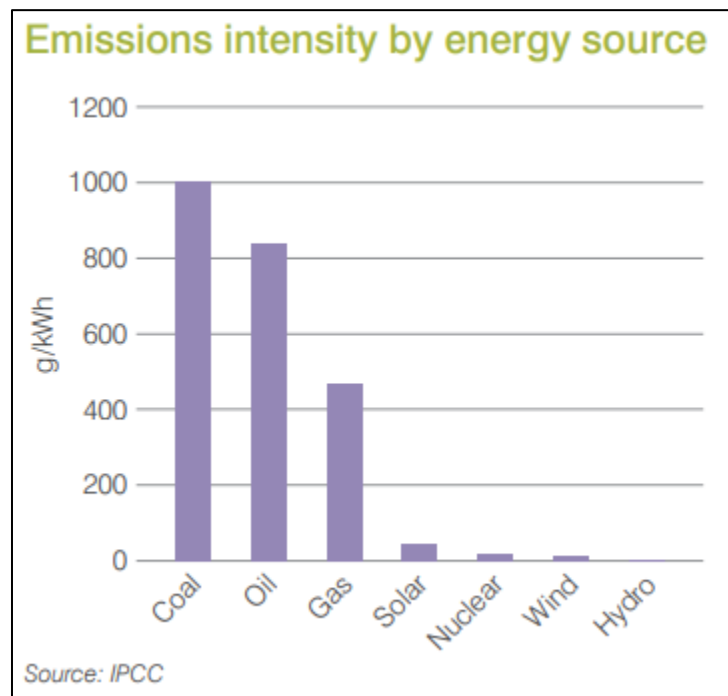


Figure 2.2: Emissions intensity by energy source in g/kWh [16]

According to the IEA, 40% of the existing nuclear power fleet in advanced economies will be retired by 2030 without additional lifetime extensions [14]. In the US alone, over one hundred nuclear power plants will be granted lifetime extension from 40 to 60 years after major upgrade investment [17]. Nuclear power reactors are further discussed in the following section 2.2.

## 2.2 Nuclear Power Reactors

Like in other industries, engineering to improve the efficiency and safety of nuclear power reactors is ongoing. Conventional light water reactor (LWR) types currently in use as commercial electricity sources are the pressurized water reactor (PWR) and the boiling water reactor (BWR). These LWRs are part of Generation II reactor designs, first developed in the 1950s. Improvements to and evolution of the Generation II reactors make up Generation III reactor designs, also known as advanced reactor designs, which are engineered to be safer and more accident tolerant. Generation II reactors are currently in use around the world, and as of 2018 advanced reactor designs (Generation III) were in operation in Japan, China, and the UAE [17]. Future reactor designs make up Generation IV designs are currently being researched for expected deployment in the next decade.

### 2.2.1 Uranium Fuel

As mined, uranium has only about 0.7% of its fissile isotope, U-235, and about 99.2% of the non-fissile isotope U-238 [17]. Enrichment increases the U-235 content to 3.5-5%. Enriched uranium is typically manufactured into ceramic  $\text{UO}_2$  pellets and stacked inside long zirconium alloy (zircaloy) rods referred to as fuel rods. These rods are typically 10-15 ft long, and depending on the reactor type, one reactor may use thousands  $\text{UO}_2$  fuel rods to generate electricity [17].

Fission of the U-235 happens by introducing a neutron to the  $\text{UO}_2$  fuel, resulting in the release of fission products (atomic masses 95-135, e.g., Ba, Kr, Sr), additional neutrons, and energy (~85% kinetic) [18]. Energy is also released in the form of gamma rays. The  $\text{UO}_2$  pellets limit the distance the released kinetic energy can travel, and it is converted to heat. Neutrons may be released immediately after fission or may be delayed by a few seconds, depending on the

half-life of the fission product. Delayed neutron release enables a chain reaction of controlled nuclear fission to be used for nuclear power (figure 2.3).

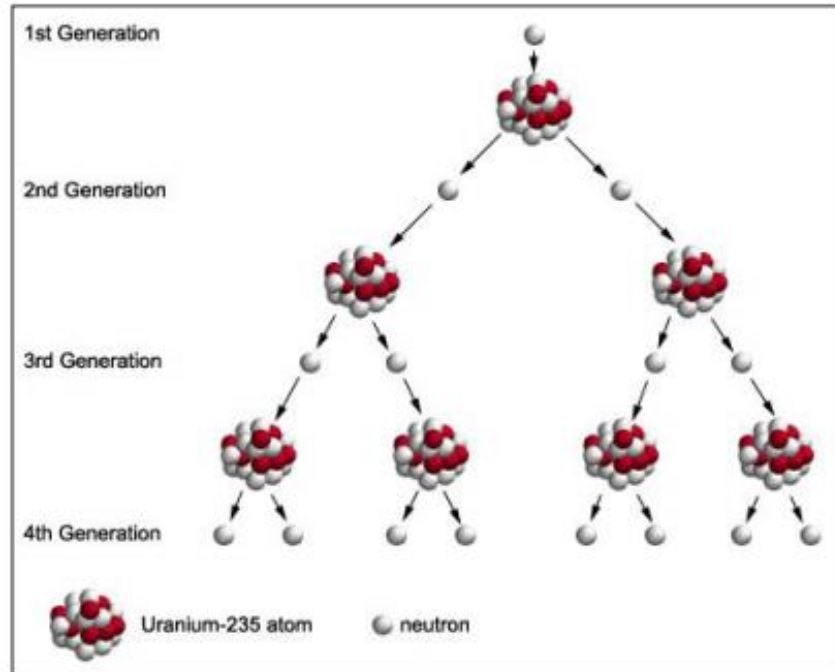


Figure 2.3: U-235 atoms split with the addition of a neutron starting a chain reaction. Additional nuclear fission products not shown. From [19].

A system is critical when neutrons produced by fission is constant in the system [18]. A moderator is also included in the core (e.g., Water, heavy water, graphite) to further slow the neutrons released from fission and aid in sustaining the chain reaction. Power of the reactor is increased or decreased by using the control rods made of neutron-absorbing material, allowing for control of the number of neutrons in the system [17].

Although nuclear reactors have a very high emission intensity, they are not typically categorized as a renewable energy source due to the generation of spent nuclear fuel. Over years of use, fission products slowly accumulate in the fuel rods which act as neutron absorbers in the system. After about 3 years, the fuel rods must be replaced. Burnable poisons (e.g., Gd) may be

added to the fuel or coolant to compensate for excess neutron absorbers in the system [17]. In the U.S., spent nuclear fuel is stored in pools or in dry cask storage, and is heavily regulated for safety. As of 2017, the U.S. Nuclear Regulatory Commission reported storing over 100,000 spent fuel assemblies [19].

### 2.2.2 Current Reactors (Generation II-III)

LWRs were designed after designs for nuclear powered submarines in the 1950s, and use heat generated by the nuclear fuel to generate steam that is used for electricity. Of the designs in place today, all use a form of  $\text{UO}_2$  fuel. LWRs make up approximately 82.5% of nuclear power plants in use commercially today (table 2.1) [17].

Table 2.1: Commercial nuclear power plants in commercial and operational as of April 2020, adapted from [17]

Reactor Type	Main countries	Number	GWe	Fuel	Coolant	Moderator
Pressurized water reactor (PWR)	USA, France, Japan, Russia, China, South Korea	299	283	Enriched $\text{UO}_2$	water	Water
Boiling water reactor (BWR)	USA, Japan, Sweden	65	65	Enriched $\text{UO}_2$	Water	Water
Pressurized heavy water reactor (PHWR)	Canada, India	48	24	natural $\text{UO}_2$	Heavy water	Heavy water
Gas-cooled reactor (AGR)	UK	14	8	Natural U (metal), enriched $\text{UO}_2$	$\text{CO}_2$	Graphite
Light water graphite reactor (LWGR)	Russia	13	9	Enriched $\text{UO}_2$	Water	Graphite
Fast neutron reactor (FNR)	Russia	2	1.4	$\text{PuO}_2$ and $\text{UO}_2$	Liquid sodium	None
<b>Total</b>		441	390			



Both PWRs and BWRs make use of water as the coolant and as the moderator, which absorbs neutrons and slows them [17]. The PWR uses pressurized water throughout the primary circuit that can reach temperatures  $>300^{\circ}\text{C}$  in the reactor core. The secondary circuit uses the heat generated by the primary circuit to boil water for steam generators (figure 2.4).

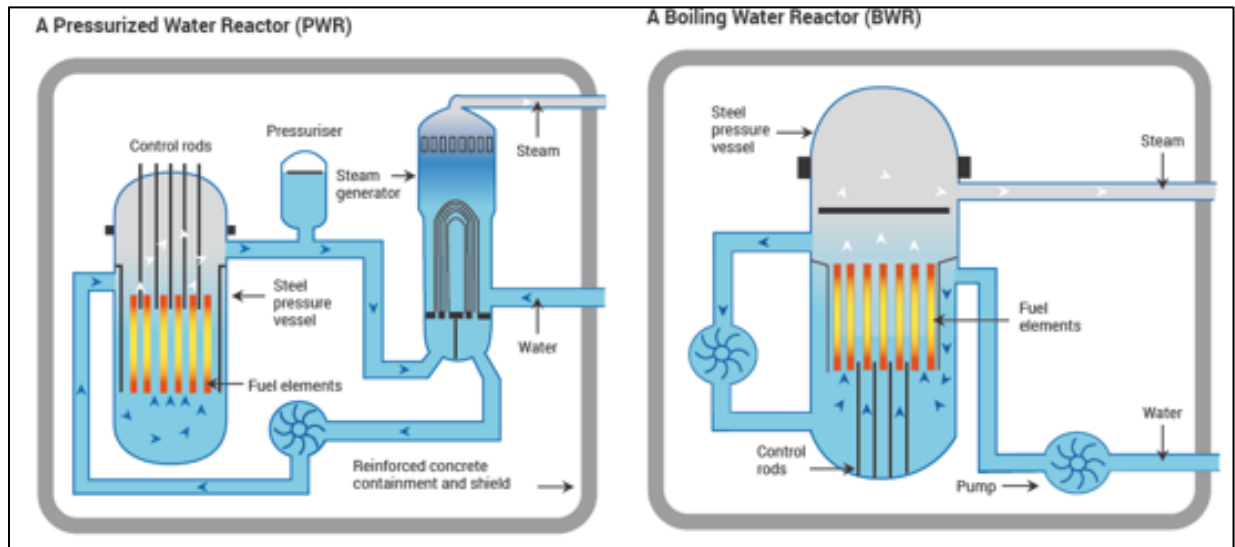


Figure 2.4: Schematic of a PWR and a BWR, from [17]

A BWR only has one circuit. The system is held at pressure such that water in the core will boil at  $285^{\circ}\text{C}$ , generating steam [17]. Turbines driven by the steam are included in the reactor circuit. Other commercial reactor types will not be discussed here. Descriptions of each can be found in reference [17].

### 2.2.2.1 Loss of Cooling Accidents

Zr-based alloys have long been used as the fuel cladding in LWRs (figure 2.3). During normal operating conditions, the Zircaloy is transparent to neutrons, and maintains corrosion

resistance and strength with direct exposure to nuclear fuel. One current commercial zircaloy is Zircaloy-4 (Zr-1.14Sn-0.32Fe-0.17Cr at%) [20].

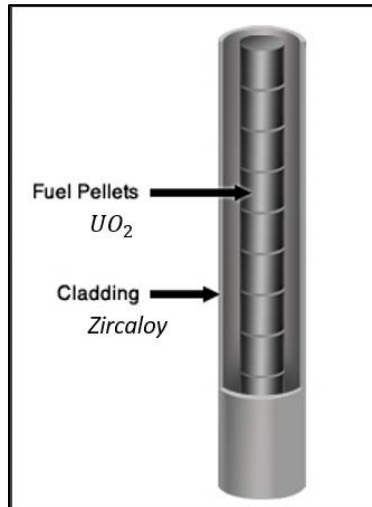


Figure 2.5: Schematic of Zircaloy fuel rod containing fuel pellets. Adapted from [21]

Unfortunately, the events of the Fukushima disaster in March 2011 showed that the accident behavior of Zr cladding could become catastrophic when core cooling is interrupted. The Fukushima Daiichi BWR operated by Tokyo Electric Power Company experienced loss of coolant due to the Great East Japan Earthquake and subsequent tsunami waves. Units 1-3 and 4 (later on) lost backup generator power and the pumps for the Residual Heat Removal (RHR) cooling system were damaged [22]. When cooling was interrupted, the decay heat in the reactor core increased the temperature to beyond normal operating conditions of 300-400°C. The emergency core cooling system (ECSS) had been designed to respond to known accident scenarios, or design basis accidents (DBAs), and did not include a plan for the events that took place on March 11, 2011 [22]. The zircaloy cladding failed first by physically degrading, ballooning and bursting at temperatures 700-1000°C, then degraded chemically at temperatures >1000°C via exothermic steam oxidation of Zr, adding to the heat of the core (figure 2.6) [23].

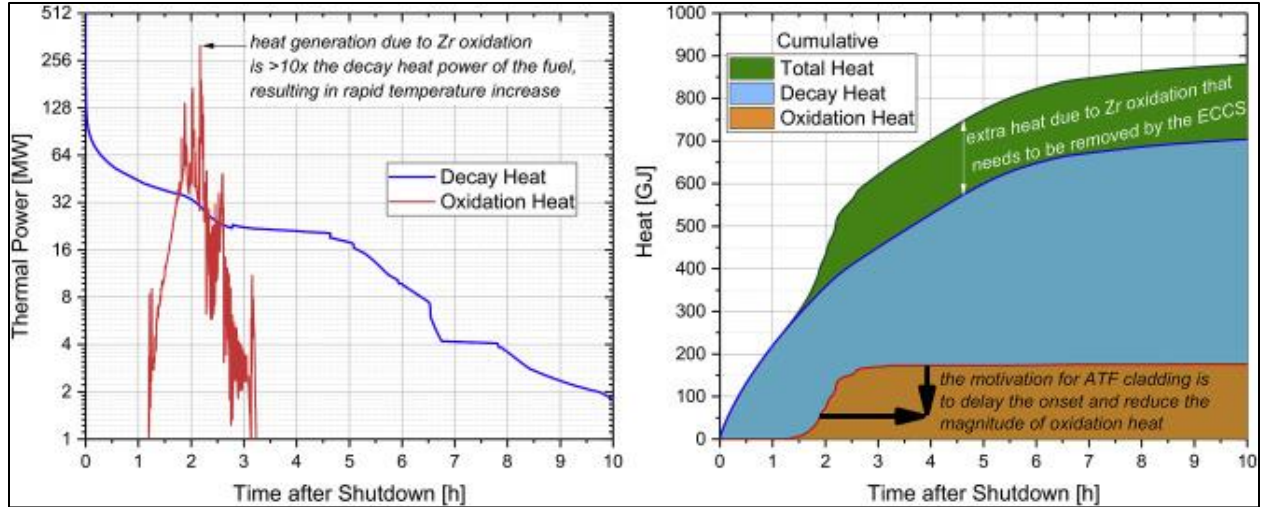


Figure 2.6: Thermal power and cumulative energy due to decay heat and Zr-base cladding oxidation. From [23] with permission from [24].

Since 2011, research developing accident tolerant fuel (ATF) cladding materials drop-in replacement has been underway. In this work, FeCrAl alloys have been identified as a potential candidate, based on their corrosion resistance with stable Cr and Al-oxide scale and retained strength at high temperatures via oxide dispersion strengthening (ODS) (figure 2.7).

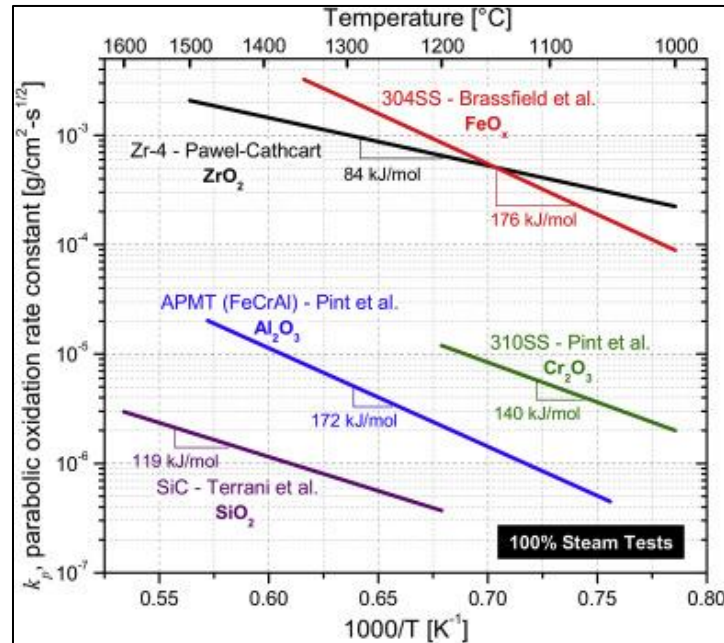


Figure 2.7: Parabolic oxidation rate for various cladding materials and resulting oxide in steam at elevated temperatures. From [23].

The Fe-base oxide dispersion strengthened (ODS) gas atomization reaction synthesized (GARS) powders discussed in this thesis have potential application as drop-in cladding replacement ATF materials.

### 2.2.2 Generation IV Reactors

Generation IV reactor designs are currently being researched, with expected deployment between 2020 and 2030. The Generation IV International Forum (GIF) has several designs under development (Table 2.2)

Table 2.2: Generation IV reactor designs under development by GIF. Adapted from [17]

	Neutron spectrum (fast/thermal)	Coolant	Temperature (°C)	Pressure*	Fuel	Fuel cycle	Size (MWe)	Use
Gas-cooled fast reactors	fast	helium	850	high	U-238+	Closed, on site	1200	Electricity & hydrogen
Lead-cooled fast reactors	fast	Lead or Pb-Bi	480-570	low	U-238+	Closed, regional	20-180** 300-1200 600-1000	Electricity & hydrogen
Molten salt fast reactors	fast	Fluoride salts	700-800	low	UF in salt	closed	1000	Electricity & hydrogen
Molten salt reactor – <b>advanced high-temperature reactors</b>	thermal	Fluoride salts	750-1000		UO <sub>2</sub> particles in prism	open	1000-1500	hydrogen
Sodium-cooled fast reactors	fast	sodium	500-550	low	U-238 & MOX	closed	50-150 600-1500	electricity
Supercritical water-cooled reactors	Thermal or fast	water	510-625	Very high	UO <sub>2</sub>	Open (thermal) closed (fast)	300-700 1000-1500	Electricity
Very high temperature gas reactors	thermal	helium	900-1000	high	UO <sub>2</sub> prism or pebbles	open	250-300	Hydrogen & electricity

\*high = 7-15 MPa

+ = with some U-235 or Pu-239

\*\* battery model with long cassette core life (15-20 yr) or replaceable reactor module

All of the Generation IV reactor designs operate at higher temperatures than current commercial designs. Consequently, the materials used for these will require greater reliability, along with high strength and high creep and corrosion resistant properties in extremely corrosive environments. ODS materials are one family of materials being researched for use in Gen IV reactors. The Fe-ODS GARS process discussed in this thesis has potential application for use in generating ODS materials for Gen IV reactors.

### CHAPTER 3. OXIDE DISPERSION STRENGTHENED ALLOYS

As materials for energy applications experience increasingly extreme environments, the necessity for those materials to reliably operate in and withstand corrosive environments, high temperatures, and high stresses has increased. Oxide dispersion strengthened (ODS) alloys have long been of interest for application in these environments due to their retained high-temperature mechanical properties and improved radiation resistance over traditional ferritic or martensitic steels [1].

#### 3.1 Strengthening Mechanism

Although there are several hardening mechanisms that contribute to the strength of ODS materials, one primary component is the network of nano-metric oxides dispersed throughout the matrix that add strength via Zener pinning. Unlike precipitate hardened alloys, ODS alloys gain their strength from a refractory oxide phases dispersed throughout the structure that are not soluble in the matrix phase, and therefore cannot re-dissolve at high temperatures [25]. Similarly, at elevated temperatures other methods of strengthening metals may become ineffective (table 3.1); for example, dislocation densities generated during work hardening may be released and allow the material to recrystallize after annealing.

Table 3.1: Strengthening mechanisms in metals [9]

<b>Strengthening Mechanism</b>	<b>Effective Temperature</b>
Work hardening	$\sim 0.3T_m$
Grain Size	$\sim 0.3 T_m$
Solid Solution Strengthening	$\sim 0.4 T_m$
Precipitation Strengthening	$\sim 0.6 T_m$
Oxide Dispersion Strengthening	$\sim 0.9T_m$

Like in precipitate strengthened materials, dispersoids in ODS materials act as obstacles to dislocations moving through the matrix (Figure 3.1). The strength of an obstacle is defined as the critical angle  $\phi_c$  required to overcome it. For strong obstacles,  $\phi_c \simeq 0$ , as the dislocation has to almost double back on itself to move past the obstacle. For weaker obstacles,  $\phi_c \simeq \pi$ , as very little bending is sufficient to overcome the obstacle [26]. The critical stress to overcome a strong or weak obstacle can be defined as a function of  $\phi_c$ , and obstacle spacing  $L$  (equations 1, 2) [27].

$$\tau_{Strong} \cong \frac{Gb}{L} \cos \frac{\phi_c}{2} \quad \text{Equation 1 [27]}$$

$$\tau_{weak} \cong \frac{Gb}{L} \left( \cos \frac{\phi_c}{2} \right)^{\frac{1}{2}} \quad \text{Equation 2 [27]}$$

$G$  = shear modulus

$b$  = burgers vector

$L$  = obstacle spacing

$\phi_c$  = critical bend angle

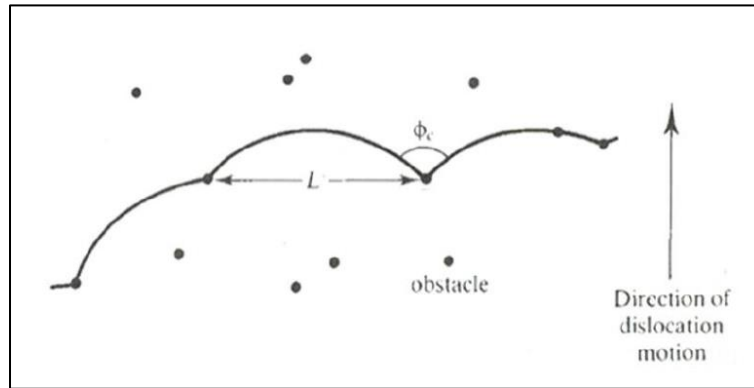


Figure 3.1: Random obstacles throughout matrix material holding up dislocation motion, where  $L$  denotes particle-particle spacing, and bending angle  $\phi$  defines the strength of the obstacle [26]

For hard particles impenetrable to dislocations, segments will be forced to bow around the obstacle leaving behind dislocation loops (figure 3.2) [28]. These loops were first discovered by E. Orowan in 1948, and consequently are commonly referred to as Orowan loops.

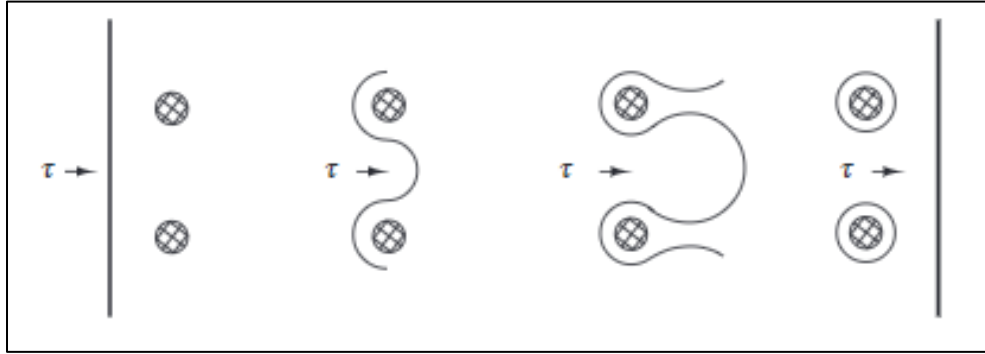


Figure 3.2: The Orowan model for hard particle obstruction of edge dislocation motion [28]

Orowan defined the maximum yield stress of a strong obstacle by using the elastic energy of a line dislocation and substituting in the radius of the particles as  $r = L/2$  (equation 3) [26, 28].

$$\tau_{max,Orowan} \approx \frac{Gb}{2r} = \frac{Gb}{L} \quad \text{Equation 3 [26, 28]}$$

The Ashby-Orowan equation incorporates the effects of particle size and spacing (equation 4) to calculate the yield stress,  $\tau_y$ , of an alloy strengthened by dispersed phases or incoherent precipitates [28].

$$\tau_y = \tau_m + \left[ \frac{Gb}{2.38\pi(1-\nu)^{1/2}} \ln \left( \frac{r_o}{b} \right) \right] / L \quad \text{Equation 4 [28]}$$

$\tau_y$  = yield strength

$\tau_m$  = critical shear stress for matrix without precipitate

$G$  = shear modulus

$b$  = burgers vector

$\nu$  = Poisson's ratio

$r_o$  = radius of precipitate

$L$  = precipitate spacing



In precipitate strengthened alloys, particles will shear until critical radius  $r_c$  is reached during the aging process. As particles grow to  $r_c$ ,  $\tau_{max,Orowan}$  decreases until the shear stress required for dislocations to bow between particles is less than shearing particles (figure 3.3) [28]. Maximum strength for the alloy is obtained by aging such that precipitates reach  $r_c$  in size. Underaging will result in sheared precipitates, and overaging will result in a loss of strength as precipitates coarsen and precipitate spacing,  $L$ , becomes too large [28].

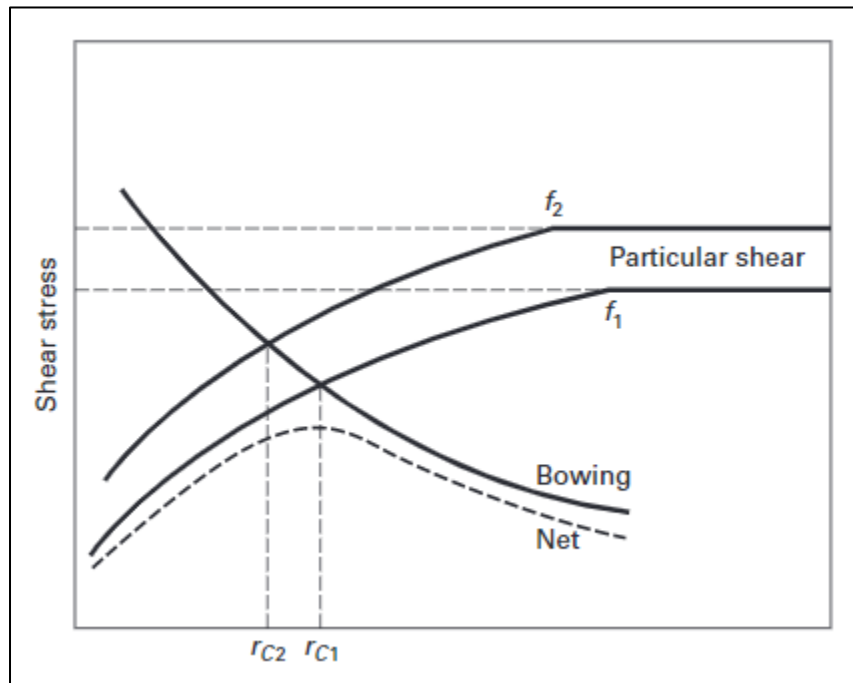


Figure 3.3: Weak obstacle particle shear or dislocation bowing at two critical radii and two volume fractions of precipitates ( $f_2 > f_1$ ) [28]

Additional mechanisms that contribute particle strengthening include coherency hardening, surface or chemical hardening, ordered hardening, and modulus hardening. These mechanisms will not be discussed here, but a detailed discussion can be found in [29].

In ODS materials, the dispersed nano-metric oxide phases act as strong obstacles. As predicted by equation 3, Fe-ODS alloys show a decrease in strength with increasing dispersoid size and spacing.

### 3.2 Creep Resistance

Fe-ODS materials are desirable for their retained high temperature strength, including creep resistance. Creep is especially important for materials operated in the range  $0.5T_m < T < T_m$ , when diffusion is thermally activated, and operating at stresses  $\sigma < \sigma_y$  [28]. As operating temperature increases for a given engineering stress, time to failure decreases (figure 3.4) [28].

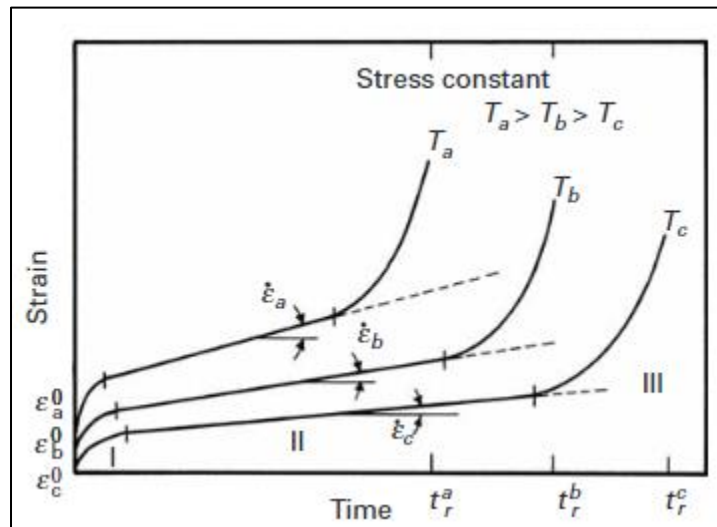


Figure 3.4: Creep strain vs. time to failure for different temperatures at a constant stress [28]

Creep can be broken into three identifiable stages: Primary or transient creep, secondary or steady state creep, and tertiary creep. Primary or transient creep is analogous to work hardening, as the material plastically deforms, and dislocations are generated. Secondary or steady state creep is dominated by dislocation motion and is highly temperature dependent. As fine grained materials deform at intermediate temperatures, secondary creep is controlled by Coble creep, where atomic diffusion takes place primarily along grain boundaries[29]. At high

temperatures, Nabarro-Herring creep mechanisms take over for deformation in coarser-grained metals, where atomic diffusion takes place throughout the lattice, no longer restricted to the grain boundaries [29].

At temperatures  $>0.5T_m$  the function for axial strain rate,  $\dot{\epsilon}$ , at intermediate to high temperatures is given by equation 5 [29].

$$\dot{\epsilon} = A \frac{D_{\text{eff}}Gb}{kT} \left( \frac{\sigma}{G} \right)^n \quad \text{Equation 5 [29]}$$

$A$  = dimensionless constant

$D_{\text{eff}}$  = effective diffusion coefficient. Function of lattice diffusion and diffusion through dislocation cores

$G$  = shear modulus

$b$  = burgers vector

$k$  = Boltzmann constant

$T$  = absolute temperature

$\sigma$  = applied stress

$n$  = stress exponent. Values shown in table (3.2)

Table 3.2: Creep stress exponent values per dominating creep mechanism [29]

<b>Dominating Mechanism</b>	<b><math>n</math></b>
Glide-controlled creep, $T < 0.5T_m$	$\sim 3$
High-temperature dislocation glide plus climb or lattice diffusion	$\sim 5$
Lower temperature core diffusion	$\sim 7$
Lattice diffusion through constant substructure	$\sim 8$

Equation 5 can be adopted to express Coble and Nabarro-Herring creep by changing the dimensionless constant A, effective diffusion coefficient  $D_{\text{eff}}$ , and stress exponent to reflect each mechanism (equations 6 & 7) [29].

$$\dot{\epsilon}_{Co} = \frac{A_{Co} D_{gb} G b}{kT} \left(\frac{b}{d}\right)^3 \frac{\sigma}{G} \quad \text{Equation 6 [29]}$$

$$\dot{\epsilon}_{NH} = \frac{A_{NH} D_L G b}{kT} \left(\frac{b}{d}\right)^2 \frac{\sigma}{G} \quad \text{Equation 7 [29]}$$

In addition to temperature, creep rate is highly dependent on grain size. Smaller grains have greater grain boundary area to provide vacancies, and consequently creep rate increases [29].

ODS alloys possess a fine grain structure with nano-metric oxides dispersed throughout and are often used in applications up to 1000°C, and consequently do not follow Nabarro-Herring or Coble creep mechanisms exactly. Strengthening contributions from solid solution hardening, dislocation interactions, coherency hardening, and Orowan strengthening all play a role in ODS creep behavior [30]. A general Arrhenius type model was developed for ODS materials by Rösler and Arzt in 1990, termed the RA model (equations 8, 9) that reported dispersion strengthened alloys to behave more like materials with a strong attractive particle-dislocation interaction with weaker energy phase boundaries [30].

$$\dot{\epsilon} = \epsilon_0 \cdot \exp\left(-\frac{E_d}{k_B T}\right) \quad \text{Equation 8 [30]}$$

$$\epsilon_0 = \frac{D_v \lambda \rho}{b} \quad \text{Equation 9 [30]}$$

$\dot{\epsilon}$  = strain rate

$E_d$  = activation energy required for dislocation detachment

$k_B$  = Boltzmann's constant

T = absolute temperature

$D_v$  = volume diffusivity

$\lambda$  = particle spacing

$\rho$  = particle density

$b$  = burgers vector

$E_d$  is defined as a function of dislocation line tension, relaxation parameter, and applied stress (equation 10) [30].

$$E_d = Gb^2r \left[ (1 - k) \left( 1 - \frac{\sigma}{\sigma_d} \right) \right]^{\frac{3}{2}} \quad \text{Equation 10 [30]}$$

$G$  = shear modulus

$b$  = Burgers vector

$r$  = dispersoid radius

$\sigma$  = applied tensile stress

$\sigma_d$  = detachment stress

$k$  = relaxation parameter

( $k=1$ , no attraction between dispersoids and dislocations;  $k \ll 1$  strong particle-dislocation attraction)

The RA model reported that the detachment stress required to overcome the attractive force of a dispersoid in an ODS material after slow creep deformation is far greater than the stress predicted for dislocation climb, and thus the strain rate is reported as a function of the activation energy required for dislocation detachment,  $E_d$  [30]. The relaxation parameter is dependent on dispersoid spacing, size, and volume fraction. Experimental data can be used to determine  $k$  for specific polycrystalline alloy systems by using equation 11 [9, 30].

$$\tau_d = \tau_0 \sqrt{1 - k^2} \quad \text{Equation 11 [9, 30]}$$

$\tau_d$  = detachment resolved shear stress

$\tau_0$  = Orowan resolved shear stress

As relaxation parameter  $k$  increases, dispersoid radius increases and the creep strength of the ODS alloy decreases with decreasing strain rate [30]. Due to differences in alloy compositions and dispersoid and dislocation densities, creep models specific to individual alloy families based off of the RA model have been developed, and corroborated with experimental data [31-33].

### 3.3 Radiation Resistance

Radiation effects take place very rapidly in materials (table 3.3), and microstructures and chemistries will continue to evolve with sustained radiation exposure throughout their lifetime. Defect production takes place very rapidly in materials exposed to neutron radiation (table 3.3).

Table 3.3: Defect production timescales for irradiated metals. From [34]

Time (s)	Event	Result
$10^{-18}$	Energy transfer from the incident particle	Creation of a primary knock-on atom (PKA)
$10^{-13}$	Displacement of lattice atoms by the PKA	Displacement cascade
$10^{-11}$	Energy dissipation, spontaneous recombination, and clustering	Stable Frenkel pairs (single interstitial atoms (SIA) and vacancies) and defect clusters
$>10^{-8}$	Defect reactions by thermal migration	SIA and vacancy recombination, clustering, trapping, defect emission

The order of radiation damage processes is given by G. Was et al. as follows [34]. Please note that accompanying each generation of a displaced atom is a Frenkel pair vacancy:

- “1. The interaction of an energetic incident particle with a lattice atom.
2. The transfer of kinetic energy to the lattice atom giving birth to a primary knock-on atom (PKA).
3. The displacement of the atom from its lattice site.

4. The passage of the displaced atom through the lattice and the accompanying creation of additional knock-on atoms.
5. The production of a displacement cascade (collection of point defects created by the PKA).
6. The termination of the PKA as an interstitial ” [34]

A schematic of the cascading effect of a displaced atom is shown below in figure 3.5, with resulting point defects from cascade of Frenkel pairs throughout the lattice. At reactor operating temperatures  $> 300^{\circ}\text{C}$ , materials may receive a neutron dose of as much as 200 displacements per atom (dpa) [1]. Self-interstitial atoms (SIAs) may recombine with vacancies after a few jumps, but almost  $1/3$  will undergo long range diffusion through the lattice [1]. Defects may be trapped or annihilated at so called “defect sinks” where they are more stable if they do not recombine on their own in the lattice [35]. Defect sinks include grain boundaries, voids, interfaces, and dislocations. Oxide dispersoids in Fe-ODS alloys (Y, O containing) have been shown to be very stable, and are unaffected by the flow defects, and the dispersoid-matrix interface is a known strong sink for point defect removal [35]. Dislocation sink strength is proportional to the dislocation density of the material, but is enhanced by bias for “SIAs to preferentially annihilate at dislocations” [1].

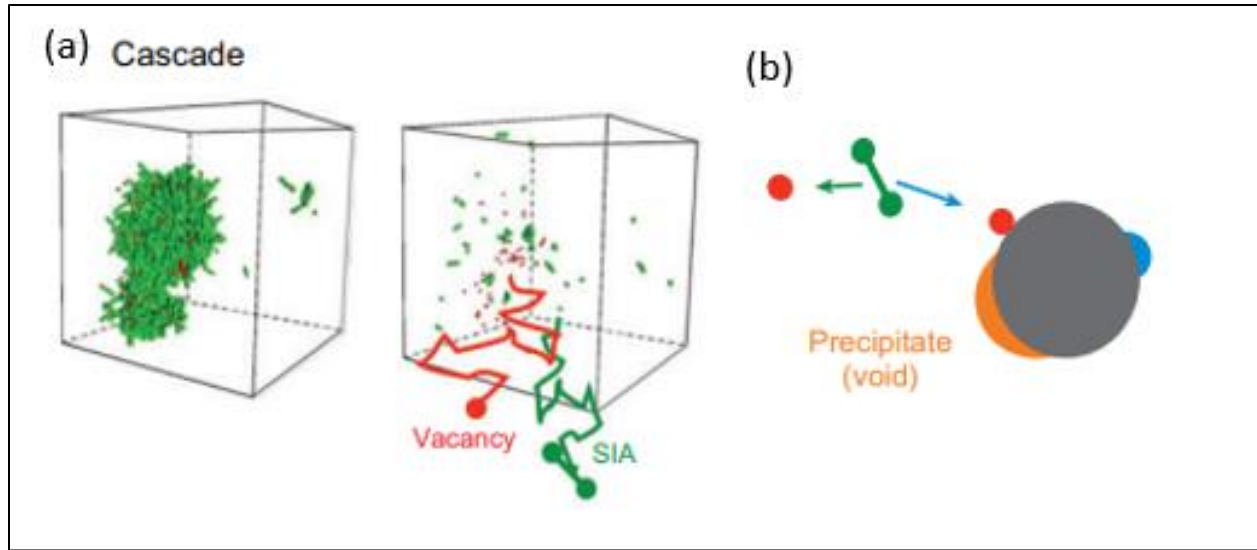


Figure 3.5: (a) Schematic of cascade production of vacancies and self-interstitial atoms (SIA), and (b) SIA recombining with diffusing vacancy and vacancy trapped at precipitate. Adapted from [1]

Radiation may also induce solid transmutation products, including H through  $(n, p)$  reactions, He through  $(n, \alpha)$  reactions, among others. Although H is chemically active, He collects in bubbles that can cause voiding swelling of the material, leading to failure if unchecked [1].

### 3.4 Brief overview of Fe-ODS alloys

Mechanically alloying was developed in 1968 by the International Nickel Company (INCO) in the US, and found immediate application through the generation of Ni-base Inconel alloys with increase in upper operating temperatures [36]. INCO went on to introduce MA956 and later MA 957, which were commercially available Fe-ODS products [5]. Metallwerk Plansee GmbH in Germany developed PM2000 which was made commercially available [5]. The compositions of these alloys can be found in table 3.4. Early applications of Fe-ODS steels were for heat exchanger tubes for fossil energy power plants, but interest grew in MA-957 for nuclear applications because of the higher yield stress and tensile strength of the alloys and high radiation resistance [5, 37].



Table 3.4: Compositions of some commercially available Fe-ODS alloys, from [9]

<b>Alloy</b>	<b>Fe at%</b>	<b>Cr at%</b>	<b>Y at%</b>	<b>Al at%</b>	<b>Ti at%</b>	<b>W at%</b>	<b>Mo at%</b>	<b>O at%</b>
<b>MA956</b>	Bal.	21.54	0.23	11.09	0.32	--	--	0.65
<b>MA957</b>	Bal.	14.5	0.17	--	1.13	--	0.17	0.72
<b>PM2000</b>	Bal.	18.92	0.23	9.84	0.54	--	--	0.65

Oak Ridge National Laboratory (ORNL) developed 12YWT, with 12 wt% Cr, in 2004, specifically designing with intent for use in Gen IV fission reactor high temperature environments [5]. In the lab setting, ORNL was able to start with higher purity materials to reduce alloy contamination from the MA process [5]. This first heat of 12YWT was found to have comparable properties and dispersoid concentrations to MA957, and both had superior properties to those of MA956 [5]. ORNL went on to develop a second alloy, 14YWT, with 14 wt% Cr, which is now one of the frontrunner nanostructured ferritic alloys (NFAs) of today for application in Gen IV reactor settings (see section 3.4.1). The term NFA was used to distinguish the fine grain and dispersoid sizes and improved properties from the commercially available Fe-ODS alloys. The compositions of 12 and 14YWT are given in table 3.5:

Table 3.5: Compositions of 14 and 12YWT alloys

<b>Alloy</b>	<b>Fe at%</b>	<b>Cr at%</b>	<b>Y at%</b>	<b>Al at%</b>	<b>Ti at%</b>	<b>W at%</b>	<b>Mo at%</b>	<b>O at%</b>	<b>Ref.</b>
12YWT	Bal.	21.54	0.23	11.09	0.32	--	--	0.65	[5]
14YWT	Bal.	16.23	0.08	--	0.54	0.28	--	0.14	[2]

There are many other Fe-ODS alloy compositions not mentioned here, including 9Cr-ODS alloys and advanced austenitic steels. The work for this thesis centered around ferritic steels because austenitic steels are known to have inferior radiation resistance to ferritic steels and may be subject to void swelling. Two other Fe-based alloy families of interest are discussed in the following sections.

### 3.4.1 FeCrAl Alloys

To avoid disaster in the event of a nuclear accident in existing light water fusion reactors, accident tolerant fuel (ATF) cladding materials are being developed as drop-in replacements that outperform the oxidation resistance of existing Zr-containing cladding materials [3]. Fe-Cr-Al alloys or “FeCrAl” alloys display optimal oxidation resistance at high temperatures ( $T \sim 1400^\circ\text{C}$ ) and corrosion resistance and mechanical properties at normal operating temperatures ( $T < 400^\circ\text{C}$ ) [3] for LWR systems. Although radiation induces precipitation of the embrittling Cr rich  $\alpha'$  or  $\sigma$  phases out of solution at normal operating temperatures for alloys containing  $>12$  wt% ( $\sim 13$  at%) Cr, compositions including  $>3$  wt% (6 at%) Al were effective in reducing the stability of the Cr  $\alpha'$  phase (figure 3.6) [3, 38]. FeCrAl alloys are currently in production, though not produced via powder metallurgy (PM) routes due to the high production costs. The benefit of PM routes is that they allow for additional alloying elements to added for FeCrAl ODS alloys, which have oxide precipitates (Y/Ti oxides) dispersed throughout the alloy that increase strength and prevent grain boundary sliding via Zener pinning [3].

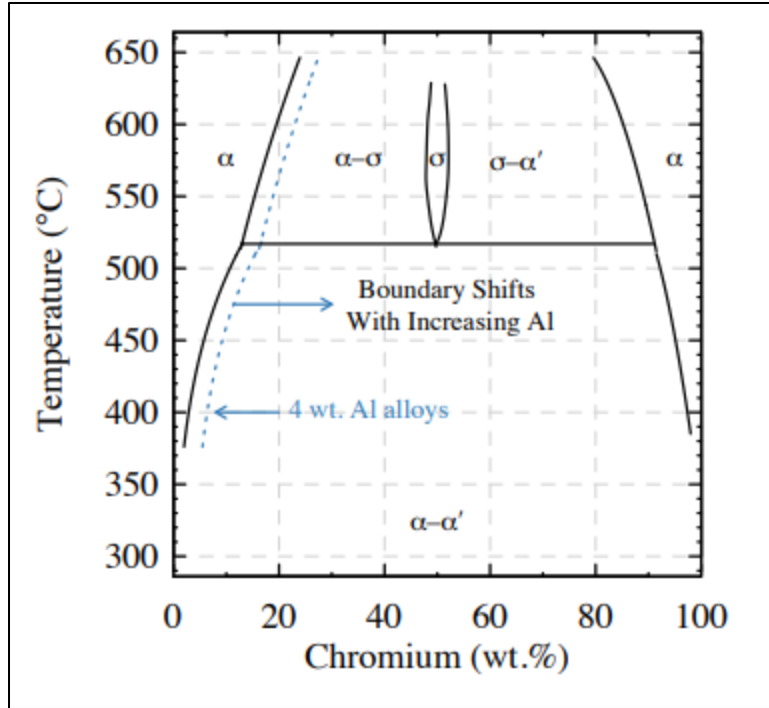


Figure 3.6: Effect of Al additions on  $\alpha$ - $\alpha'$  phase boundary for Fe-Cr binary alloy. From [39]

### 3.4.2 NFAs

Nano-Ferritic Alloys (NFAs) were distinguished from traditional Fe-ODS materials by Oak Ridge National Lab [1]. ORNL increased the milling intensity and energy compared to commercial Fe-ODS alloys by increasing times in high energy ball mills, and as a result saw increased microstructure refinement [5]. NFAs generally contain ~13-22 at% Cr in addition to Y, Ti, W and O. Fine Y-Ti-O nanofeatures (NFs) are dispersed throughout the microstructure with sizes on the order of a few nanometers and have primarily been shown with TEM analysis to contain complex oxides including the pyrochlore  $\text{Y}_2\text{Ti}_2\text{O}_7$  and  $\text{Y}_2\text{Ti}_2\text{O}_5$  [1]. Examples of NFAs include 14YWT, and MA957. Extensive research is being conducted on NFAs for structural application materials for Generation IV reactors [1, 2, 40, 41].

### 3.5 Manufacturing

The production of Fe-ODS alloys for application consists of powder production, consolidation, thermal-mechanical treatment (TMT), and final machining (Figure 3.7). These basic manufacturing steps are commonly used to produce Ni-base ODS superalloys, such as Inconel 754, but are also used for Fe-base ODS materials [42]. The following sections describe traditional and novel methods for manufacturing steps of Fe-ODS materials.

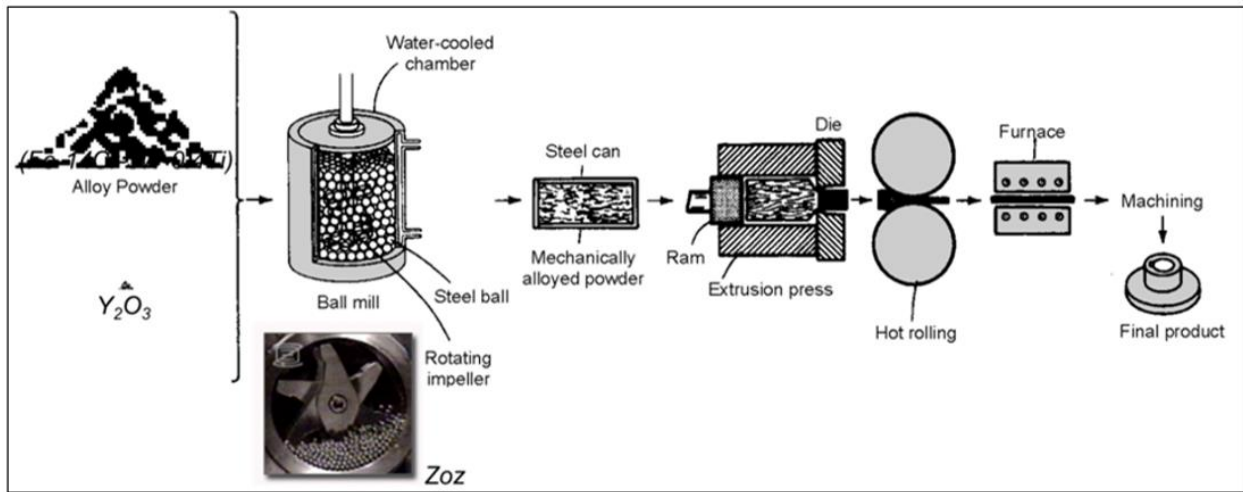


Figure 3.7: Example of a traditional manufacturing route for ODS alloys [43]. Oxide additions vary with alloy family to achieve the desired precipitate phase.

#### 3.5.1 Mechanically Alloying

Traditionally, mechanical alloying has been used to manufacture Fe-ODS alloys because it allows for dissolution of a refractory oxide phase (e.g.,  $Y_2O_3$ ) with a base alloy family (e.g., Ferritic steels), and generates a high dislocation density, even distribution of oxides, and highly misoriented grains with local grain sizes as fine as 1-2 nm [36, 44]. The refractory oxide phase powder and the base alloy powder are combined in a high energy ball mill (e.g., SPEX shaker mill or Zoz attritor mill) and milled under inert atmosphere where alloy powders and oxide phases are repeatedly cold welded and fractured in the mill after impact with milling media

(Figure 3.8) [4]. Ratios of balls to powder is usually around 10 to 1 [4]. Mechanical alloying is optimal for alloys containing reactive alloying elements, such as aluminum, titanium, and chromium [42]. Milling for more than 40 hours may be needed to achieve the desired hardness, fine grain size, and to fully dissolve refractory oxides [36, 42].

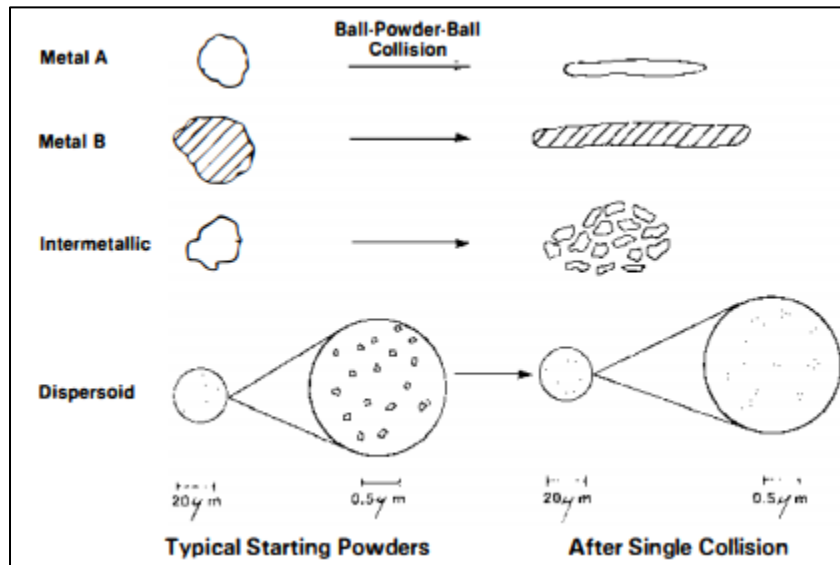


Figure 3.8: Schematic showing deformation behavior of starting metal powders during mechanical alloying [42]

Contaminants, however, may arise during the milling process; wear of the ball milling media and/or the canister, along with entrapment of inert gasses are common in MA powders [42]. Batch-to-batch variability is also a problem, as there will be slight differences in contaminants between each batch of powder, which can affect the integrity of the final microstructure [9]. The sources of and effects of these contaminants on the performance of the MA alloys has consequently developed into a field of study in order to predict alloy behavior [40]. Mechanically alloyed powders have high hardness, and consequently are not amenable to cold-compaction methods [36, 44].

### 3.5.2 Traditional Consolidation

The highly cold worked mechanically alloyed powder is first canned and vacuum degassed and then consolidated via extrusion or by hot isostatic pressing (HIP). These methods can produce either raw material in the form of sheet, bar stock, or an expendable core can be used to produce tubes. Consolidation usually takes place between 900 and 1100°C [42]. HIPed material usually has a very fine grain size ( $<0.5\ \mu\text{m}$ ) [42], whereas extruded material will have anisotropic and textured grains, with as much as a 10/1 length-to-diameter ratio [1]. Both extruded and HIPed materials require further thermomechanical treatment (TMT) before application.

### 3.5.3 Traditional TMT and machining

For application in high temperature and environments, the consolidated material must be recrystallized in order to increase creep resistance, or to mitigate anisotropic effects of extrusion [1, 44]. TMT may consist of hot working (hot rolling) or cold deformation (pilgering, swaging, drawing) and annealing. Cold deformation processes followed by annealing may be preferred to hot working in order to reduce recrystallization temperatures by reducing the stored energy of the alloy [44]. In Ni-base superalloys produced via MA powders, the recrystallized grain structure may be controlled by isothermal annealing or by zone annealing at high speeds, as the precipitate particles distribute more uniformly [42]. In iron-based alloys, though, annealing has little effect on development of columnar grains parallel to the extrusion direction due to the alignment of dispersoids along the working direction, which can result in creep strengths lower by as much as half in the hoop direction compared to the extrusion direction [1, 44].

## CHAPTER 4. GAS ATOMIZATION REACTION SYNTHESIZED POWDERS

Manufacturing methods that avoid the batch to batch variability and long milling times are currently being researched. One such method is the subject of this work and is termed the gas atomization reaction synthesis (GARS) method [6-8]. The GARS method produces powders that were reacted with oxygen during the atomization process to generate metastable oxides on the powder surface. The surface oxides can be dissolved upon TMT and will react with intermetallic compounds (IMCs) in the interior material to form dispersoid particulates. One of the largest advantages to the GARS method is that atomization allows for production of large batches of powder at faster processing rates and at lower cost than long milling times (Figure 5) [9].

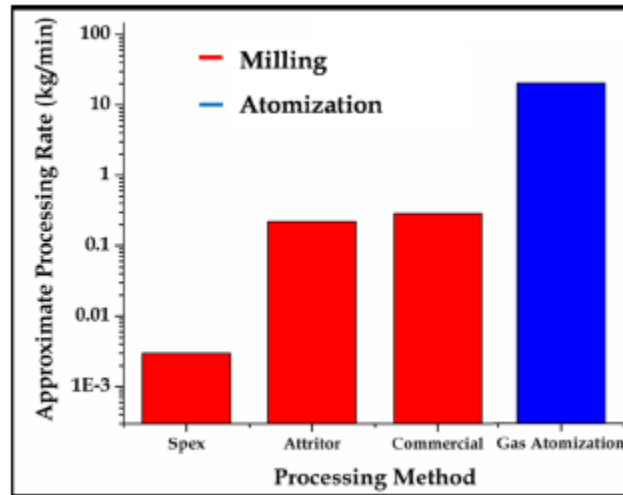


Figure 4.1: Processing rate comparison between common MA methods and gas atomization

The GARS method has been used to produce Fe- and Ni-base ODS precursor powders. [9, 45] The specific adaption of GARS production of Fe-base ODS precursor powders has been most extensively studied and is discussed in the following section.

#### 4.1 GARS Method

The gas atomization process for GARS powder production uses a reactive atomization gas (such as Ar-O<sub>2</sub>) to surface oxidize molten alloy droplets during primary breakup and solidification (Figure 4.2) [6-8]. The powder particles solidify rapidly during atomization, and an ultra-thin (<150nm) Cr-enriched metastable oxide forms on their surface [9]. Secondary alloying element concentrations were carefully selected to limit the mobility of Y during atomization. Formation of mixed intermetallic compounds (IMCs), such as Fe-(Hf, or Ti)-Y in the powder particle interior help to limit Y consumption as a stable oxide during atomization. The oxygen content of the resulting powder has been shown to have a direct linear relationship to the oxygen content in the reactive atomization gas [9].

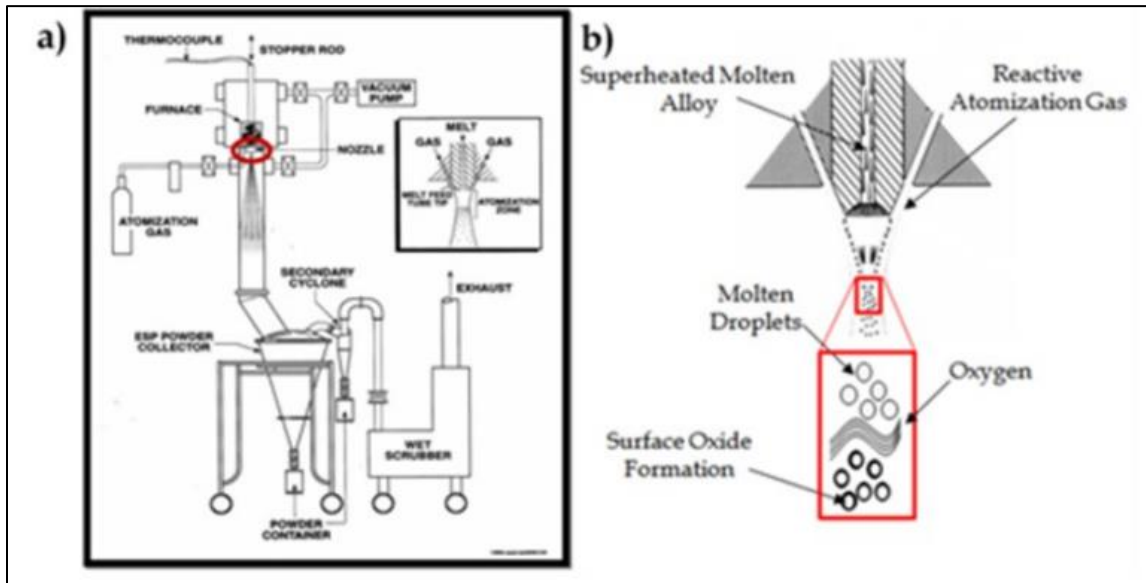


Figure 4.2: High pressure gas atomizer with highlighted reaction zone (a) and (b) [9]

No dispersoids are present in the as-atomized material. Rather, during hot consolidation, the Cr-oxide layer is dissociated from the prior particle boundaries (PPBs), and the O diffuses into the  $\alpha$ -(Fe,Cr) matrix to form more thermodynamically stable oxides (eg, with Y) (Figure



4.3) [23, 46]. Due to the diffusion of O from the initial O reservoir, the Cr-oxide phase, the alloys have been termed chemical reservoir (CR) alloys [9].

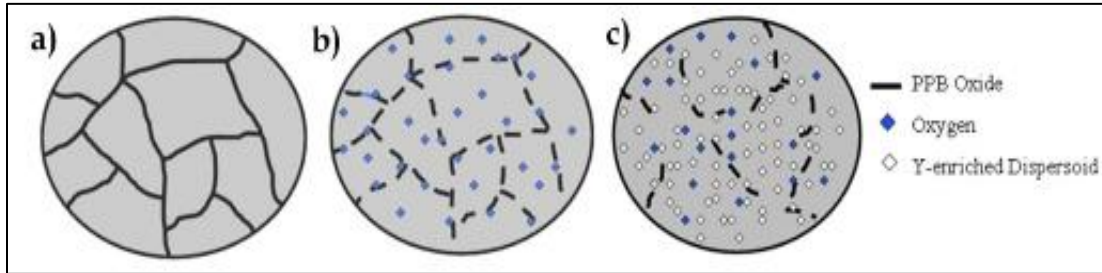


Figure 4.3: Microstructure evolution of GARS-ODS precursor powder during hot consolidation or heat treatment: “(a) initial low temperature consolidation showing intact PPBs, (b) dissociation of the PPBs (simulating heat treatment) and O diffusion into the  $\alpha$ -(Fe,Cr) matrix, and (c) formation of Y-enriched oxide dispersoids throughout the microstructure.” [9].

The Ames Lab has developed several GARS-ODS alloys of varying compositions. The Fe-ODS GARS alloys were designed specifically for Fe-Cr systems with Y-containing oxide dispersoids as the strengthening phase, and adjustments were made to the alloy composition and to the atomization process. The following table shows the compositions of the first generation Fe-ODS GARS precursor powders (Table 4.2).

GARS Fe-ODS precursor alloys all contain  $\geq 14.3$  at% Cr to stabilize the  $\alpha$ -Fe structure throughout consolidation, heat treatment, and elevated operation temperatures, and also to add corrosion and oxidation resistance [47, 48]. Al was not included in CR-112 to CR-166 to avoid the formation of Y-Al mixed oxide precipitates that are prone to coarsening, but was added into CR-198 and CR-204 after the publication of work by Kimura et. al that showed improved alloy corrosion resistance with small Al additions. Hf and Ti were added to the alloys to stabilize Y-oxide dispersoid size during high temperature TMT, and Hf is additionally known to increase creep strength [48]. However, the Hf addition is deleterious for application in radiation environments due to the high thermal neutron capture cross section. The first-generation GARS

alloys (table 4.1) were developed under fossil energy funding, and for future generations of GARS alloys to be successful in nuclear applications, Hf will need to be exchanged for Zr, as has been shown possible by Kimura et. al [49]. Zr has a preferable low thermal neutron capture cross section making it almost transparent to neutrons, and is already in use in existing nuclear power plants in the form of zircaloy cladding [20].

Table 4.1: Generation I Fe-ODS GARS precursor powder compositions

<b>Alloy</b>	<b>Fe (at%)</b>	<b>Cr (at%)</b>	<b>Al (at%)</b>	<b>W (at%)</b>	<b>Ti (at%)</b>	<b>Hf (at%)</b>	<b>Y (at%)</b>
<b>CR-112</b>	83.24	15.52					0.09
<b>CR-118</b>	83.47	15.84			0.5		0.2
<b>CR-126</b>	82.75	15.13		0.9	0.56		0.09
<b>CR-144</b>	82.55	16.16		0.94		0.27	0.08
<b>CR-156</b>	84.49	15.84				0.11	0.18
<b>CR-160</b>	78	20.88			0.58		0.09
<b>CR-162</b>	83.01	16.23			0.31		
<b>CR-164</b>	83.59	15.55				0.12	0.09
<b>CR-166</b>	83.53	15.91			0.12		0.09
<b>CR-198</b>	71.30	14.88	12.35	0.90		0.24	0.19
<b>CR-200</b>	71.08	15.49	12.12	0.98		0.24	0.09
<b>CR-204</b>	83.06	15.54	--	0.91	--	0.24	0.24

Full analysis of CR-112 through CR-166 can be found in reference [9] and analysis of CR-198 and CR-204 can be found in reference [10]. CR-200 and CR-204 are highlighted in blue as they are the alloys used for this thesis work. A further discussion of the contributions of alloying elements can be found in Chapter 3 of reference [9]. The alloy composition is balanced specifically for the most thermodynamically stable desired oxide phases to be formed upon heating (Figure 4.4), such that the free energy of the system is lowered by dissociating the metastable  $\text{Cr}_2\text{O}_3$  surface oxide and forming the desired oxide dispersoid phases.

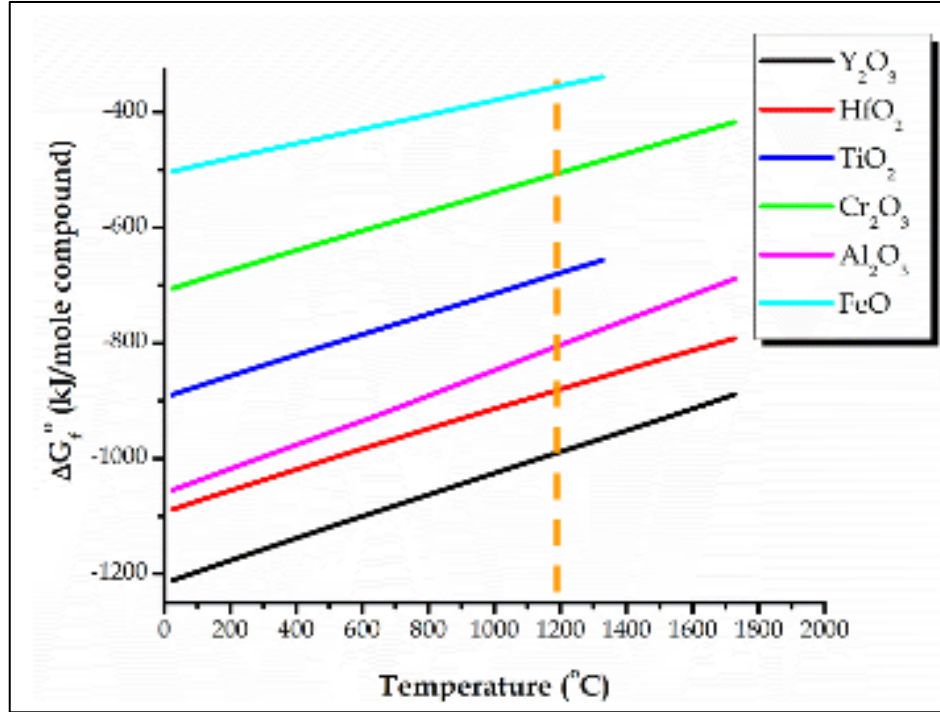


Figure 4.4: Thermodynamic stability of oxide phases based on free energy of the compound [50]

Unlike mechanically alloying, the GARS method does not present the opportunity for cold work and deformation during powder production. High plastic deformation is necessary for generating the desired high dislocation density in the final alloy structure to act as precipitate nucleation sites, increase hardness of the alloy, and to reduce the diffusion distance of oxygen from the metastable surface oxides to the powder interior. For the GARS-ODS alloys, plastic deformation must be added through alternative processing, either before or during initial consolidation of the GARS powder or after full consolidation and before heat treatment to form the nano-metric dispersoids.

## 4.2. Previous GARS Consolidation Methods

The following contains a brief summary of the consolidation studies completed on the first-generation Fe-ODS GARS alloy precursor powders. Full details of each study can be found in the accompanying references. Consolidation was completed mainly via HIP for all GARS alloys, and consequently there are many opportunities to explore the behavior of the GARS alloys with different consolidation methods.

### 4.2.1 Previous consolidation of GARS CR-96 – 166 alloys

Extensive work completed by Rieken et al. [9] established procedures for generating the first GARS Fe-ODS precursor powders, and further alloy developments began characterization of reactive gas and alloying element behaviors during the process. A very brief overview of the consolidation experiments conducted using CR-96 to CR-166 is given in table 4.1.

Table 4.1: Brief overview of consolidation experiments using CR-96 to CR-166 Fe-ODS GARS precursor powders

<b>GARS Alloy</b>	<b>Method</b>	<b>Results</b>
CR-96 CR-112 CR-118	HIP 850 and 1300°C 300 MPa 4h	Evidence of O-exchange reaction in CR-112 and CR-118 after HIP at 1300°C
CR-112 CR-118 CR-126	HIP 850 and 1300°C 303 MPa 4h	Y additions to alloy to investigate optimal O/Y ratios. Amorphous surface oxides identified via AES and He-XRD analysis. Surface oxide thickness as a function of oxygen in reactive atomization gas investigated. Evidence of O-exchange reaction at 1300°C
CR-118 CR-144 CR-156	HIP 700°C 303 MPa 4h  Post-HIP Heat Treat 1000-1300°C	O content in reaction gas found to have linear effect on O content in as-atomized powders. Microsegregation of Hf and Y along as-solidified cell boundaries in as-atomized CR-144 and CR-156 powders. Stabilization of PPB oxide phase prior to dispersoid formation found to be unfavorable, as could lead to coarsening of IMC precipitates. Heat treatment of as-HIPed structure (1000-1300°C) identified greater dispersoid stability by replacing Ti with Hf to form Y-Hf-O dispersoids.

Table 4.2 continued

<b>GARS Alloy</b>	<b>Method</b>	<b>Results</b>
CR-164 CR-166	HIP 700°C 300 MPa 4h Post-HIP Heat Treat 1200°C	Heat treatment at 1200°C successfully dissociated PPB oxide, and O was consumed via internal oxidation of Y-containing IMC precipitates, forming Y-(Hf or Ti)-O dispersoids. Y-Hf-O dispersoids showed greater resistance to coarsening than Y-Ti-O dispersoids with longer heat treatment times, which agreed well with calculated decrease in molar volume between the two.
CR-156	HIP 700°C 20 MPa 4h  Post-HIP heat treat 1200°C  Cold Rolled 20-80% reduction Anneal 500-600°C for 1hr	Size divisions 20-53 $\mu\text{m}$ , 5-20 $\mu\text{m}$ , and <5 $\mu\text{m}$ . O content increased with decreasing powder size division. Powder <5 $\mu\text{m}$ showed even distribution of dispersoids, due to higher solidification rate during atomization that resulted in uniformly distributed Y-Hf enriched nano-metric clusters.  Annealing at 600°C led to partial recrystallization and significant loss in microhardness. When annealing was reduced to 500°C, dislocations recovered to dispersoid interfaces, which resulted in formation of fine sub-grain dislocation structure, and significant increase (~2X) in alloy microhardness

#### 4.2.2 Previous consolidation of GARS CR-198 and CR-204 alloys

Atomization and consolidation of CR-198 and CR-204 are presented in reference [10], and the as-atomized powder compositions can be found in table 4.1. The purpose of the study was to generate an Al-containing alloy (CR-198) to observe its effects on alloy corrosion resistance and dispersoid sizes, based on the work by Kimura et al. [48].

Auger depth profiling revealed that oxide thickness on the as-atomized powders was dependent on powder size (figure 4.5, table 4.2). Surface oxide of as-atomized powders contained Y rather than Cr oxides for larger powder particles, and more Fe, Cr, and Al oxides for smaller powders, due to the slower cooling rate for larger powder particles. Oxide thicknesses were taken as the crossover point between O and Fe majority counts, which is equivalent to the 50% maximum count for both elements, the normal level considered to represent the thickness.

Oxide layer thicknesses were found to be higher for CR-204 than for CR-198 by 1-2 nm, which corresponds to a slightly higher oxygen content in CR-204 than in CR-198. This was confirmed with LECO elemental analysis. Both alloys had segregation of Y and Hf in a cellular structure in powders  $>7\mu\text{m}$  in size.

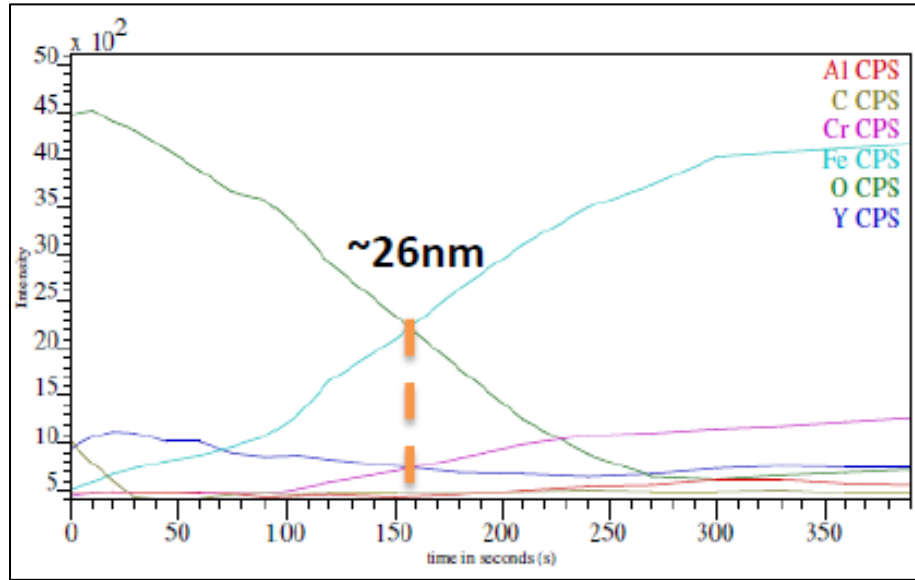


Figure 4.5: Example of auger depth profiling measurement taken of CR-204 powder  $\sim 35\mu\text{m}$  particle size. From [10].

Table 4.3: Measured Auger oxide thickness of CR-198 and CR-204. From [10]

Alloy	$\sim 13\mu\text{m}$ Powder	$\sim 35\mu\text{m}$ Powder	$\sim 68\mu\text{m}$ Powder
<b>CR-198</b>	9 nm	25 nm	32 nm
<b>CR-204</b>	11 nm	26 nm	34 nm

The two alloys were consolidated via HIP. CR-198 was HIPed for 13h at  $850^\circ\text{C}$  and 200 MPa pressure, then for 4h at  $850^\circ\text{C}$  and 300 MPa. CR-204 was consolidated at  $850^\circ\text{C}$  and 300 MPa for 4h. Both alloys were heat treated at various temperatures ( $1000\text{--}1300^\circ\text{C}$ ), and post HT showed spheroidized Hf-containing IMCs ( $\text{FeHf}_2$ ) on PPBs. Precipitation of  $\text{FeHf}_2$  at PPBs was lowest for the sample heat treated at  $1200^\circ\text{C}$  for 5h.

Post HT at 1200°C for 5h, the HIPed bars were hot rolled at 1000°C to 70% reduction in thickness, then annealed for 1 hr at 1000°C. XRD analysis of the as-atomized powder versus HIP and rolled states showed the presence of  $Y_2Hf_2O_7$  oxides in the HIP + HT and HIP + HT + rolled samples.

A 15-25  $\mu\text{m}$  cut of CR-198 was ball milled for 5h to increase oxygen content, then HIPed and heat treated at 850°C and 300 MPa for 4h, then HT at 1200°C for 5hrs. XRD of the milled + HIPed + HT sample revealed refined  $Y_2Hf_2O_7$  dispersoid size as compared to as-atomized + HIPed + HT samples. Analysis of the samples included tensile strength measurements, and steam and air corrosion resistance testing. Strengths of CR-198 and CR-204 were shown to be comparable to commercial MA965 and PM2000 alloys. CR-204 was not protective to corrosion in either atmosphere, and CR-198 spalled in air but developed a protective oxide layer in the steam atmosphere. CR-198 was found to have a sub-optimal oxygen content.

At the laboratory scale, HIP sample generation results in a high amount of waste from the 316L HIP can, the less-dense ends of a consolidated billet, and having the can machined off of the consolidated billet. The process is time intensive and expensive when producing small samples, and the process costs only grow for larger HIP production. The goal for this study was to identify novel consolidation methods for the Fe-ODS GARS precursor powders that could, if possible, enhance dislocation densities in the consolidated microstructure to increase oxide dispersion nucleation, but also retain a fine distribution of dispersoids throughout the material.

## CHAPTER 5. AI VS. NON-AI CONTAINING GARS ALLOY VHP CONSOLIDATION STUDY

### 5.1 Background

#### 5.1.1 Vacuum Hot Press Consolidation

Vacuum hot pressing (VHP) is commonly used for the production of beryllium or titanium parts [42]. Graphite dies are filled with the desired powder weight and placed inside of the vacuum furnace box. The furnace is evacuated to vacuum, and then the tools are heated to the desired compaction temperature ( $\sim 850\text{--}950^\circ\text{C}$  for Ti parts) [42]. Uniaxial pressure is applied using a hydraulic system for the desired compaction time (figure 5.1).

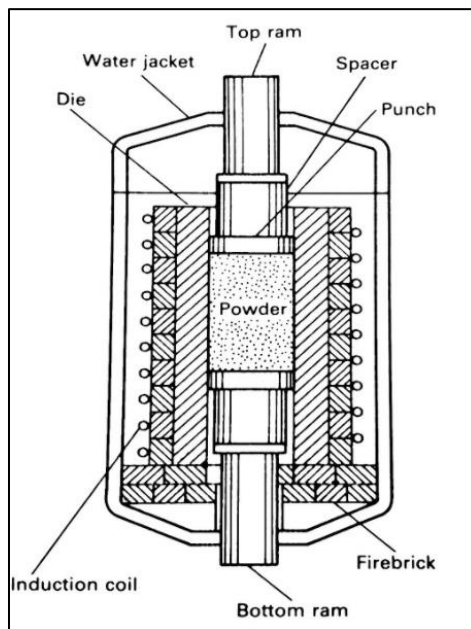


Figure 5.1: Cross section of graphite die assembly inside of induction heated vacuum furnace chamber, with hydraulically activated rams. From [42]

Once the furnace is cooled, and pressure is removed, the sample can be removed. The Centorr hot press used in this work is water cooled, but other systems may cool with inert gas or simply furnace cool [42].



Commercial VHP systems can produce billets up to 350kg (770lbs) [42]. Prealloyed aluminum powders can be hot pressed using 40-70MPa above 400°C to produce extrusion billets or forging blanks, but more complex forms are generally HIPed. Low production rates make VHP processing uneconomical for iron and steel alloy production, and HIP or CIP methods are chosen over uniaxial hot pressing [42]. Ni-base superalloys have successfully been hot pressed to full density, but as they are more reactive, superalloys may be pressed in dies made of TZM, or HIPed instead.

Vacuum hot pressing was chosen for these experiments as an alternative consolidation method to HIP for as-atomized Fe-ODS GARS alloys. This study aimed to develop a procedure for VHP processing of as-atomized GARS alloys, and to study the effects of Al additions in CR-200 as compared to non-Al alloy CR-204 (table 5.1). The CR-200 alloy VHP used -53/+20  $\mu\text{m}$  cut powder, whereas the CR-204 alloy used -45/+20  $\mu\text{m}$ .

Table 5.1: CR-200 and CR-204 as-atomized compositions

<b>Alloy</b>	<b>Fe (at%)</b>	<b>Cr (at%)</b>	<b>Al (at%)</b>	<b>W (at%)</b>	<b>Ti (at%)</b>	<b>Hf (at%)</b>	<b>Y (at%)</b>	<b>O (at%)</b>
<b>CR-200</b>	Bal.	15.49	12.12	0.98		0.24	0.09	0.14
<b>CR-204</b>	Bal.	15.54	--	0.91	--	0.24	0.24	0.14

Consolidation and heat treatment times and temperatures for the VHP samples were selected based off of prior consolidation studies with XRD results revealing dispersoid formation and phase stability in CR-164 (Hf-Y alloy similar to CR-200 and CR-204) and CR-166 (Ti-Y), in chapters 8 & 10 of reference [9].

## 5.2 Experimental Methods

CR-200 and CR-204 alloys were consolidated in a 0.25" diameter die in a Centorr Hot Press (HP). Samples were placed in the chamber until vacuum was pulled  $\leq 8 \times 10^{-6}$  torr, and the

temperature was first raised to 400°C for 30 min for adsorbed moisture outgassing. The samples were pressed under 100MPa of pressure, and intended to be held at 850°C for 4h. Unfortunately, a tornado warning meant that the CR-204 sample was only at pressure and temperature for 3hrs and 9 min, rather than the full 4h. Powder cut to size  $-53/+20\ \mu\text{m}$  was selected for CR-200, and  $-45/+20\ \mu\text{m}$  was selected for CR-204. The standard operating procedure (SOP) for operation and sample generation of the Centorr HP can be found in the appendix for the benefit of future students and staff, since this was not previously collected for the operation of this important unit.

The resulting sample was massed, and height was measured. The samples were then cut into quarters, using electrical discharge machining (EDM). Vickers microhardness measurements were taken on the base and interior of the quarters in the as-VHP condition (see figure 5.2).

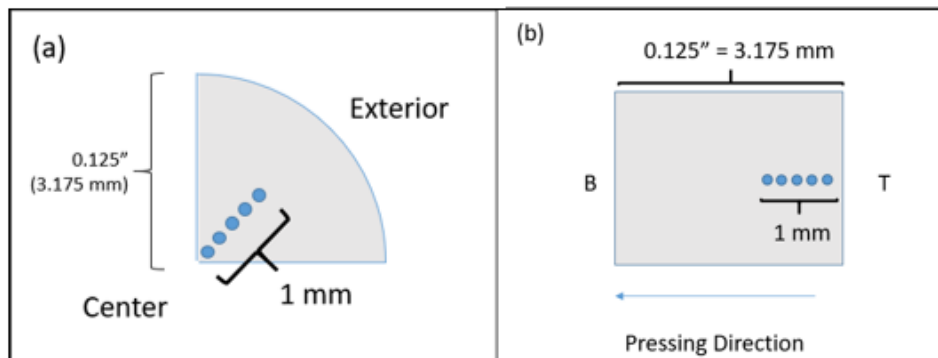


Figure 5.2: Vickers hardness measurement locations for GARS VHP samples for the base (a) and the interior side (b).

The samples were heat treated at elevated temperatures ( $>1000^{\circ}\text{C}$ ) using the following heat treatment schedule (Table 5.2) in a GCA vacuum furnace to prevent oxidation.

Table 5.2: Heat Treatment Schedule for CR-200 and Cr-204 alloy quarters (Q1-4) after VHP consolidation

	Time (hrs)	Temperature (°C)
<b>Q1</b>	--	--
<b>Q2</b>	12	1200
<b>Q3</b>	2.5	1200
<b>Q4</b>	2.5	1100

Hardness measurements were taken on the base of each of the quarters following heat treatment, using the same base indent location as in figure 5.2 (b). The samples were then prepared for orientation imaging microscopy (OIM) analysis [51]. Samples were mounted in bakelite and ground with SiC grit paper, then polished using alumina polishing media, with 10-minute ultrasonic baths prior to and between polishing steps to reduce scratching from residual porosity in the samples.

Sample analysis methods included scanning electron microscopy (SEM) and energy dispersive X-Ray spectroscopy (EDS) with a FEI Teneo SEM. The as-polished SEM samples were also etched using a ferritic stainless-steel etchant (i.e., 30 ml hydrochloric acid, 30 ml glycerol, and 10 ml nitric acid) for ~60s, and optical micrographs were captured for grain size analysis. The grain size was measured using lineal intercept method according to ASTM E112-96 (2004).

## 5.3 Results

### 5.3.1 VHP sample generation

Both powders were successfully sintered into a compact (figure 5.3), but note that for the CR-204 sample the furnace had to be shut off after 3h and 9 minutes (see above) at applied pressure of 100 MPa at 850°C.

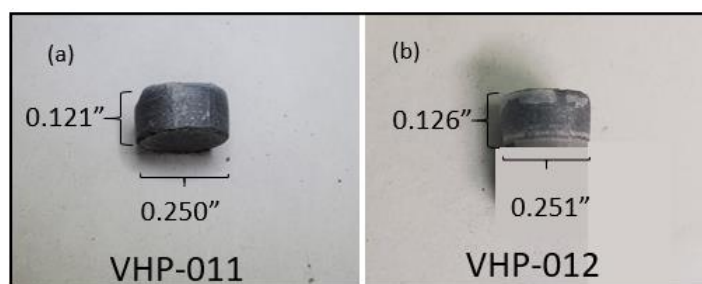


Figure 5.3: VHP samples generated at 850°C under 100MPa pressure (a) CR-200 -53/+20 um powder and (b) CR-204 -45/+20um powder. The alumina spacer still attached to VHP-012 when the image was taken was covered for image clarity.

### 5.3.2 VHP sample hardness

Vickers hardness measurements were taken with a 500 gm load on the base (// press direction) of each VHP sample as-pressed and after heat treatment. The results are shown in figures 5.4 and 5.5.

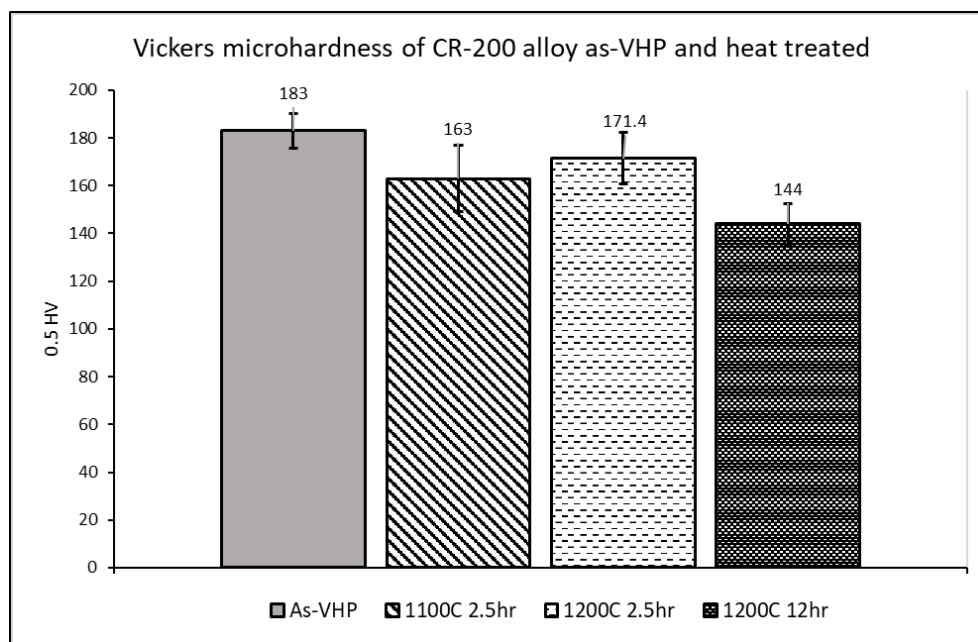


Figure 5.4: Vickers microhardness of CR-200 alloy as-pressed and after heat treatment

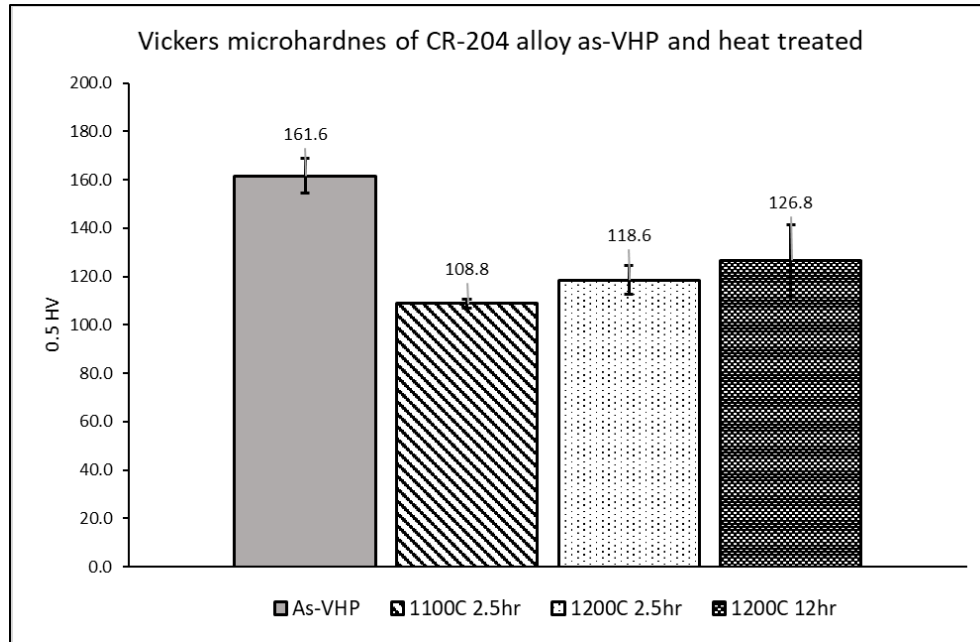


Figure 5.5: Vickers hardness of CR-204 alloy as-pressed and after heat treatment

### 5.3.2 Microscopy

The starting powder morphologies are shown in figures 5.6 and 5.7.

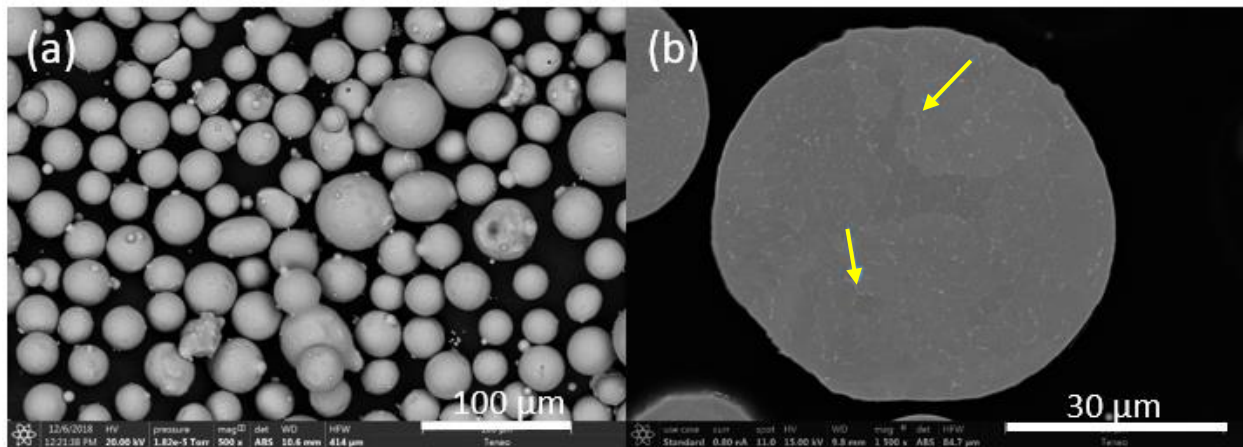


Figure 5.6: As-atomized CR-200 powder including (a) exterior powder surface morphology and (b) BSE image showing interior segregation of Y & HF along cell boundaries (yellow arrows).

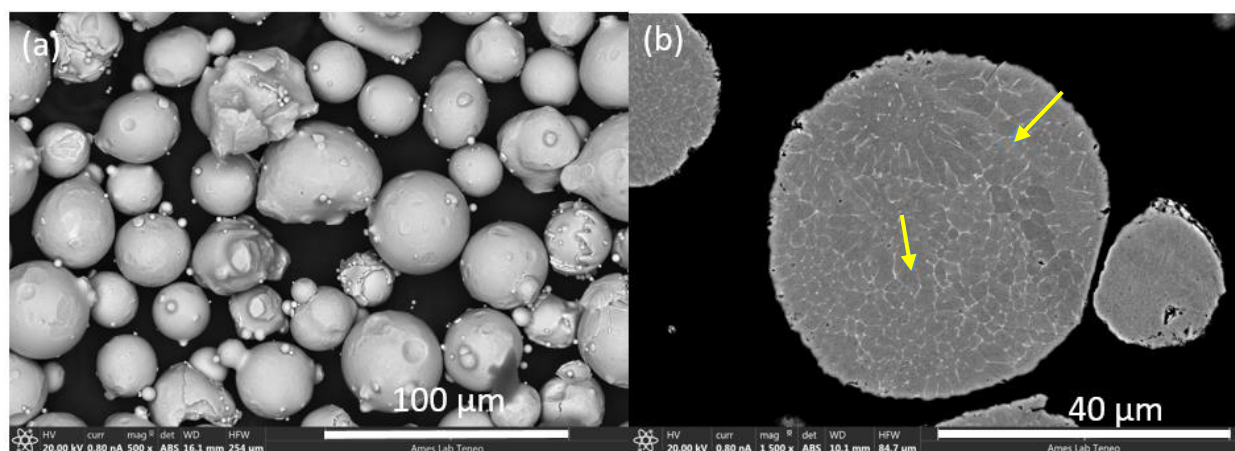


Figure 5.7: As-atomized CR-204 powder including (a) exterior powder surface morphology and (b) BSE image showing interior segregation of Hf and Y along cell boundaries (yellow arrows). Smaller particle to the right to the larger has significantly less segregation network.

Figure 5.8 shows the as-VHP microstructures of the two alloys as VHP consolidated.

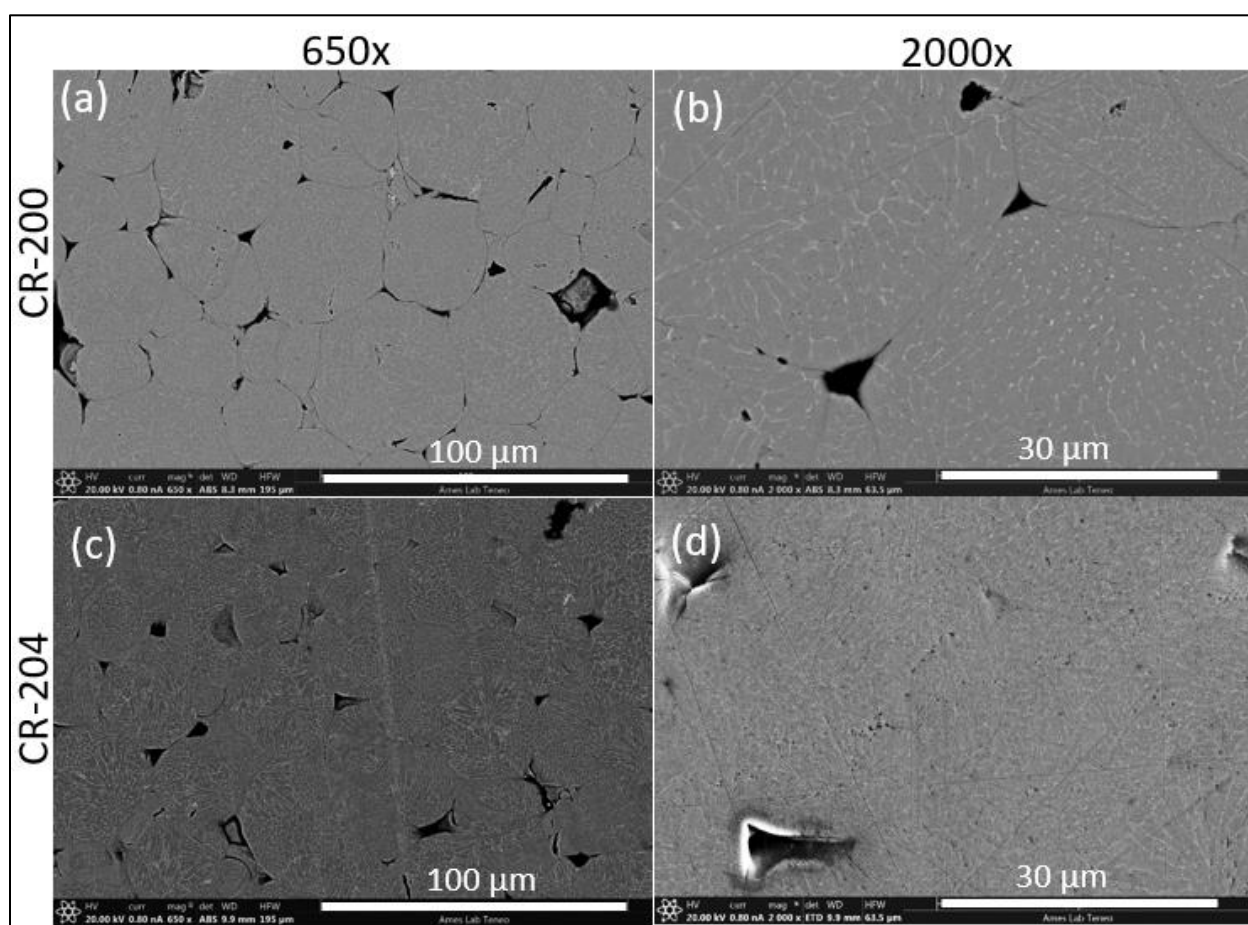


Figure 5.8: As-VHP consolidated microstructures at (a,c) 650x and (b,d) 2000x. Images taken on the base of the VHP sample, pressing direction coming out of the page.



The VHP samples were cut into quarters using EDM machining and then each quarter received a separate heat treatment in a GCA vacuum furnace. The resulting microstructures are shown below (figure 5.9).

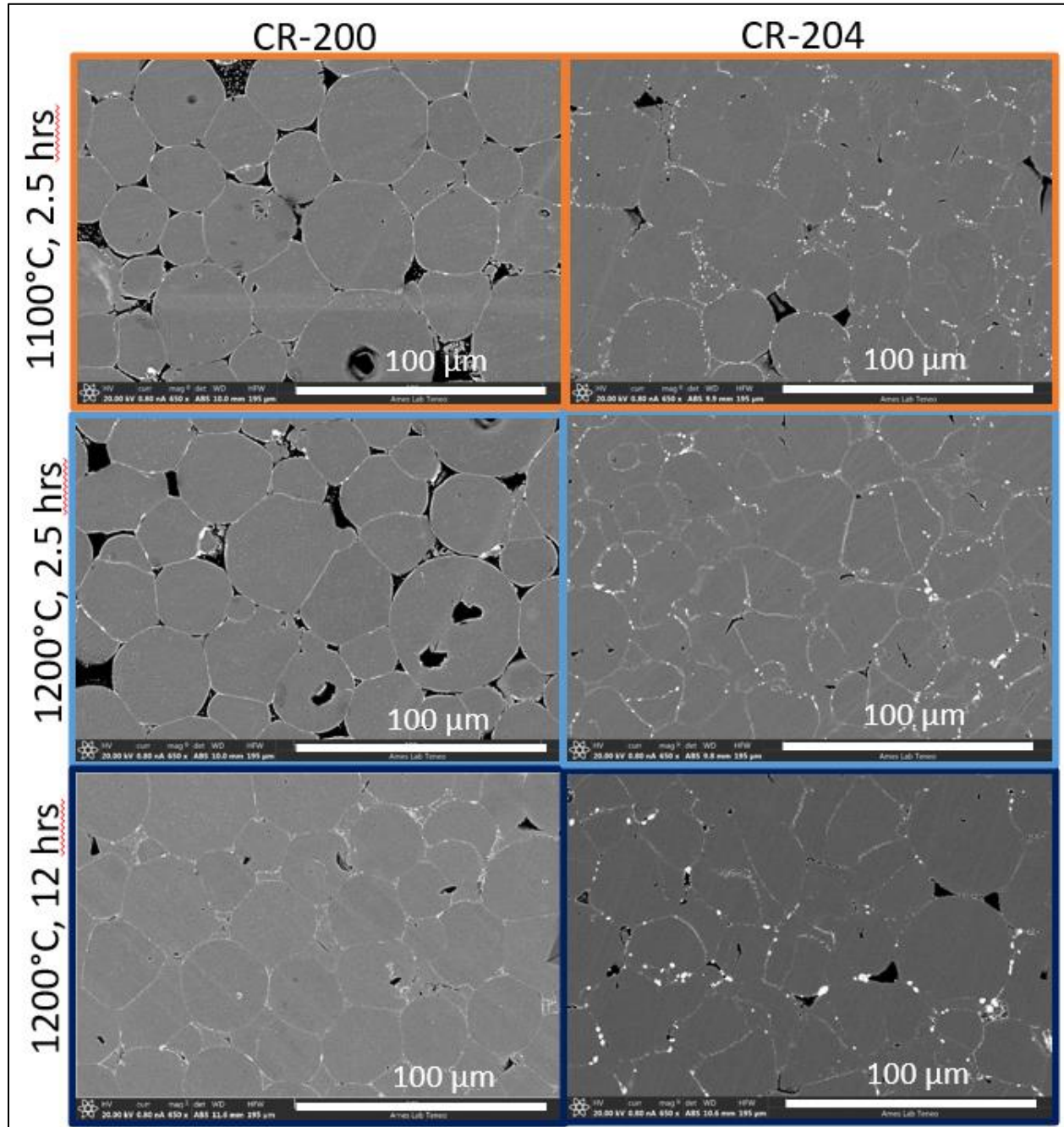


Figure 5.9: Resulting microstructures at 650x for CR-200 and CR-204 powders after VHP consolidation and vacuum heat treatment at (a,b) 1100°C for 2.5h (d,e) 1200°C for 2.5h, and (e,f) 1200°C for 12hrs.

Porosity of each quarter of the VHP samples was measured after heat treatment using imageJ threshold analysis of a stitched 150x image of the quarter (table 5.3) [52]. The samples were then etched and optical micrographs at 100x were captured of the densest parts of the surface to best represent the grains in a fully compacted sample. Grain size measurements (table 5.4) were taken using ASTM E112-13 grain size standard [53].

Table 5.3: Density of VHP samples after VHP and heat treatment, as calculated from stitched base images via ImageJ threshold analysis.

<b>Density</b>	<b>CR-200</b>	<b>CR-204</b>
<b>As-VHP</b>	89.5% *	93.8%
<b>1100°C, 2.5h</b>	96.9%	97.1%
<b>1200°C, 2.5h</b>	96.0%	96.8%
<b>1200°C, 12h</b>	98.5%	97.1%

\*Not base density data. Base of sample was chipped during mounting for polish and had to be ground further to generate flat surface.

Table 5.4: Etched VHP sample grain size measurements calculated via line intercept method

<b>Grain Size</b>	<b>CR-200</b>		<b>CR-204</b>	
	Average (µm)	Standard Deviation (µm)	Average (µm)	Standard Deviation (µm)
<b>1100°C, 2.5h*</b>	26.0	2.3	17.0	2.1
<b>1200°C, 2.5h</b>	18.4	3.2	12.86	4.5
<b>1200°C, 12h</b>	26.6	4.6	15.6	1.6

\*The densest parts of the 1100°C samples were not as sintered as the 1200°C samples, and consequently grain size measurements are larger than in reality due to number of line intersections including large pores.

EDS data was collected on each sample to identify a general elemental composition of the IMCs, matrix, and dispersoid phases. EDS plots were generated using the Oxford Aztec software. An example line scan from each powder is provided here (Figure 5.10), and the results of the remaining line scans are summarized (table 5.5).



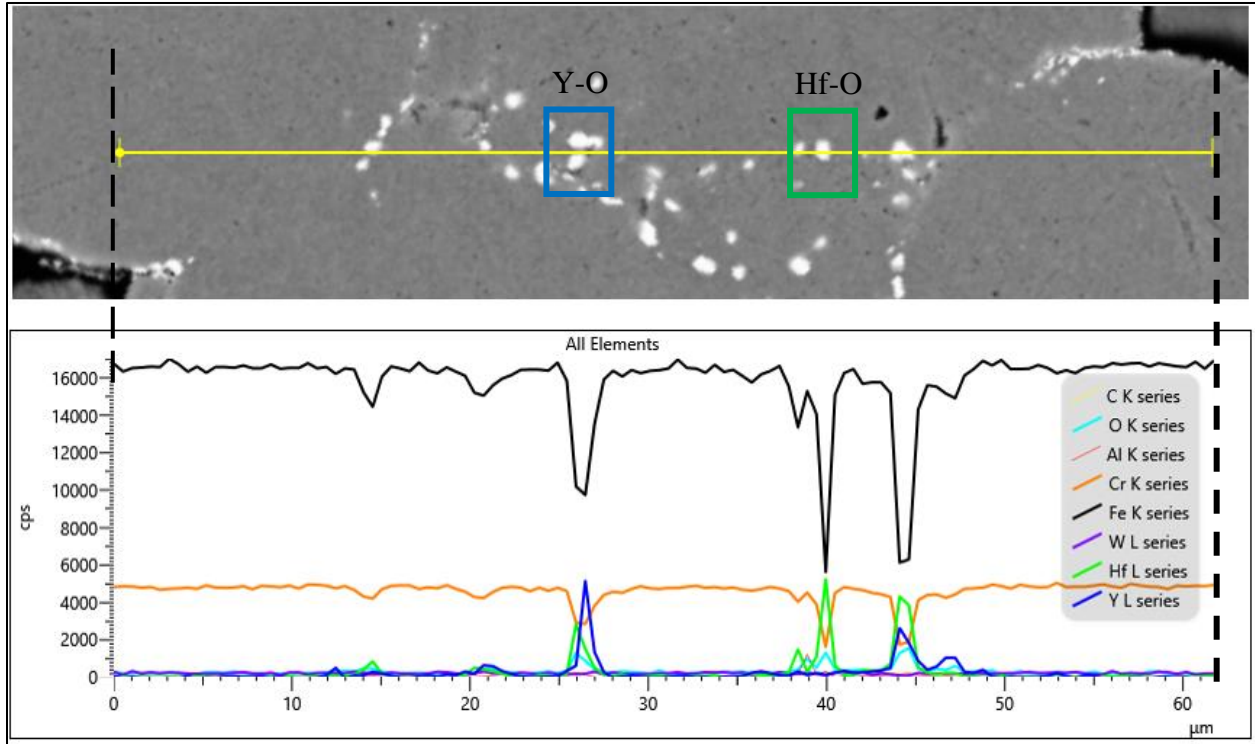


Figure 5.10: Example EDS output for CR-204 1100C for 2.5hr sample. Scale of image matches distance on the x-axis of the counts graph

Table 5.5: EDS line scan results summary for CR-200 and CR-204 as VHP and post-HT

EDS Results	CR-200	CR-204
<b>As-VHP</b>	Retained as-atomized cellular segregated structure. No distinguishable oxide phase along PPBs	Retained as-atomized segregated structure. No distinguishable oxide phase along PPBs
<b>1100°C, 2.5h</b>	Spheroidized Fe-Hf IMCs inside prior powder particles. Large coarsened Fe-Hf IMCs along PPBs, interspaced with occasional Fe-O peaks from small spherical particles all along PPBs	Interior of prior powder particles are completely free of IMCs, and PPBs show strong peaks for decreased Fe content, with increased Hf, Y, O. In areas with better consolidation (PPBs not visible), light, high contrast phases trail through matrix material, show strong Y, O peaks, and coarse spheroidized Fe-Hf-O phases (~1 μm) distributed in matrix near PPBs.

Table 5.5 continued

EDS Results	CR-200	CR-204
<b>1200°C, 2.5h</b>	Spheroidized Fe-Hf IMCs dispersed throughout prior particles. Fine, bright phase along PPBs with small increase O content.	Faint outlines of bright phases along sintered PPBs show increased Y, Hf, O content and decreased Fe.
<b>1200°C, 12h</b>	Fe-Hf IMCs along PPBs ~1-2um in size. Some faint Y-O and Hf-O signals near to PPBs. Bright dispersed phase retained in interior of some larger prior particles show increased Y-Hf-O content.	Massive (1-5um) Y-Hf-O particles along PPBs. Interior of prior particles devoid of dispersed phases. Some faint outlines with Y, Hf, O content seen in matrix as in 2.5hr sample, some evidence of cracking in smaller particles (see figure 5.11)

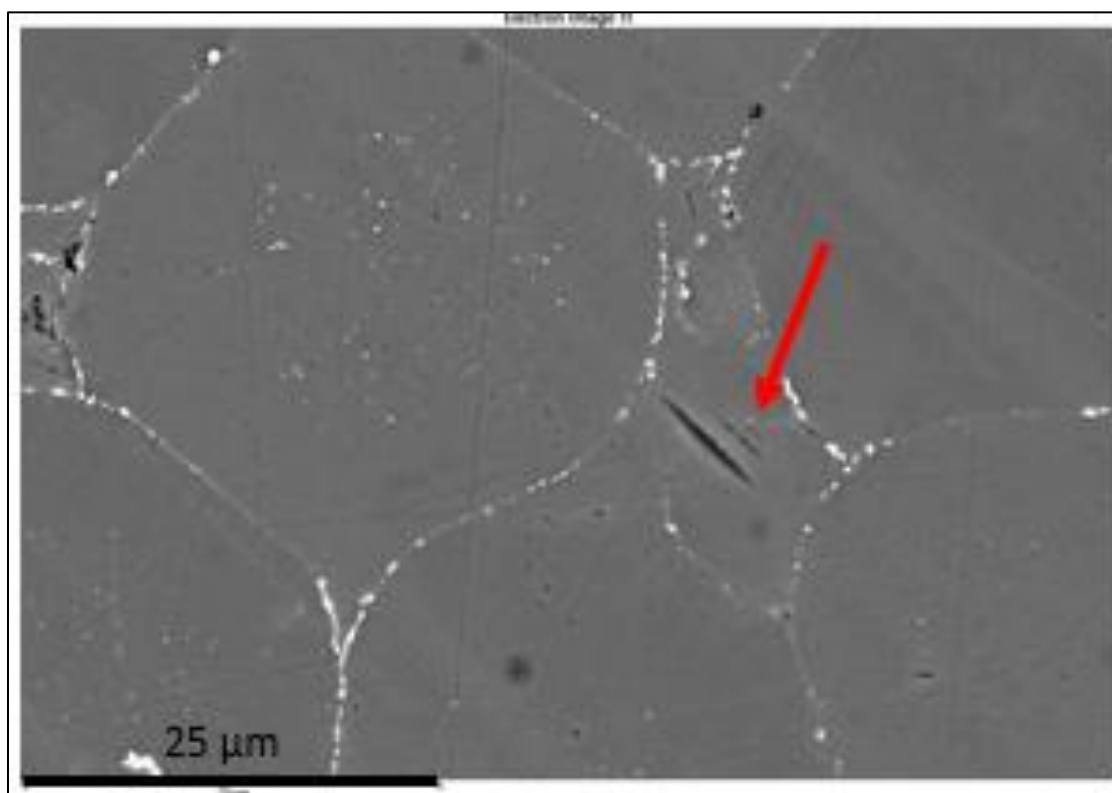


Figure 5.11: Suspected cracking of CR-204 post VHP and HT at 1200°C for 12h.

## 5.4 Discussion

### 5.4.1 VHP sample generation

VHP samples 011 and 012 were the first successfully sintered samples generated using the Centorr VHP by the author. Although previous HIP consolidation was conducted at 300 MPa, the die set used for VHP sample generation had predicted failure limit of 274 MPa. Consolidation of alloys unrelated to this study with this die set at higher pressures (200 MPa) resulted in crushing of boron nitride and hard fired alumina die liners into the sample alloy powders, resulting in an uneven sample thickness and density. Consequently 100 MPa was selected for consolidation of the GARS alloys in order to preserve the integrity of the die liners.

The as-VHP samples showed ~10% porosity for CR-200, and ~7% porosity for CR-204. In the as-atomized state, a higher pressure than 100 MPa should be used in the future to generate samples with greater as-VHP density in order to be competitive with HIP consolidation, which can consistently generate consolidated material  $\geq 98\%$  dense for Fe-ODS materials [42]. The lack of fully dense microstructure also been observed at lower temperature (700°C), lower pressure HIP (200 MPa) in chapter 10 of [9], when consolidated powder  $<5\mu\text{m}$  diameter was unsuccessful at eliminating porosity. It was suspected that the primary impediment to consolidation was the lack of plastic deformation to maximize interparticle contact area to minimize open porosity, not the slower sintering kinetics of larger powder particles [9]. Based on this recommendation, VHP samples will need to be consolidated at higher pressures in the future.

### 5.4.2 VHP sample microhardness

Based on the work completed with these alloys previously [9, 10], it was expected that samples heat treated at elevated temperatures post-consolidation would promote the O-exchange

reaction between the Cr-metastable surface oxide and Y-enriched IMCs, leading to development of dispersoid phases. The 1200°C samples were expected to show higher hardness than the 1100°C samples due increased diffusion coefficients of the oxygen after Cr-oxide dissociation and alloying additions, as higher temperatures allow for greater development of the strengthening dispersoid phase during the short, 2.5 hr heat treatment (figure 5.12) [9]. The CR-200 sample followed this trend, but the CR-204 did not, and instead hardness increased from the 2.5 hour heat treat to the 12 hour. One speculated explanation is that the Y content supersaturated the Fe-Cr matrix in the small particles. As noted in section 4.2.2, in powders >7µm diameter, the excess Y segregated out along cell boundaries in the interior of the powder particles. However, Y is trapped in a supersaturated solution in powders <7µm. Upon consolidation and heat treating for 12 hours at 1200°C, the Y had sufficient time to fall out of solution onto the PPBs, leaving small particles with leftover stresses great enough to cause cracking in the interior of small prior particles. This was not seen in any other GARS alloy to date due to the comparatively high Y content. The buildup of stresses led to increased hardening of the alloy.

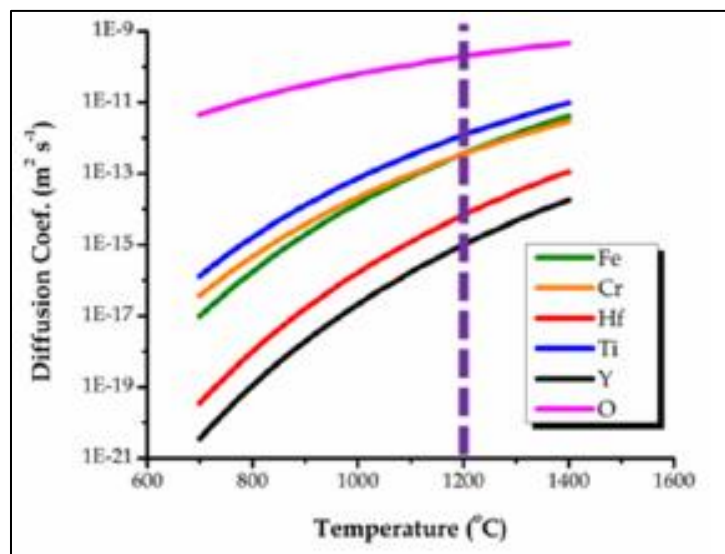


Figure 5.12: Relative alpha-Fe atomic diffusion coefficient for alloying additions. From [9]

### 5.4.3 Future Processing Options

Further work will be needed to identify non-reactive die liners that will not crush into sample powders at pressures  $>100\text{MPa}$ . Without doing so, generating samples  $> 90\%$  dense will be difficult, as pressures  $\leq 200\text{ MPa}$  have been insufficient for eliminating porosity here and with HIP consolidation [9]. If VHP consolidation is used only for low-temperature consolidation of Fe-ODS GARS precursor powders, not the high temperature O-exchange reaction, reusable die liners made from MarM-247 spray coated with BN on the interior may suffice. If vacuum hot pressing is pursued further as a method of generating Fe-ODS GARS alloys, an intermediate step between consolidation and heat treatment for dispersoid generation will be required to increase dislocation densities and refining grain size to a level that will break up PPBs and promote an even dispersion of oxides. At the commercial scale, vacuum hot pressing operations like used for existing high-purity Ti systems and Ni-base superalloys could be used for to produce Fe-ODS GARS ingots up to 125lb (55 kg) in size [42]. If large samples of consolidated Fe-ODS GARS precursor alloy could be produced into large ingots without activation of the O-exchange reaction, the ingots could undergo further deformation processing (hot rolled or cross rolled) to the final desired sheet or plate thickness to introduce the necessary dislocations for dispersoid nucleation sites and to break up the segregated Y-Hf cellular structures in the as-atomized powders. This sheet or plate material could then be heat treated and annealed to activate the O-exchange reaction and reach the desired dispersoid concentration and size.

### 5.4.3 VHP sample microscopy

Dispersoid size was expected to increase from 2.5hr hold at  $1200\text{C}$  to 12h at  $1200^{\circ}\text{C}$  based on coarsening results from heat treatment studies with CR-144 and Cr-160 (Table 4.1), resulting in decreased hardness and increased grain size. For CR-204, this was the case, but

with CR-200, EDS primarily revealed coarse Fe-Hf IMC phases, rather than oxides. Notably, no complex Y-Al oxides were identified, which is supported by the work of Kimura et al. which states Hf or Zr additions to Fe-ODS alloys help to prevent deleterious Y-Al-O phases [48, 49].

Etched micrographs of each heat-treated sample revealed grain growth from the 1200°C 2.5h HT to the 12h. Because the oxide phases and IMCs were seen to greatly coarsen with the heat treating, grain growth was able to continue uninhibited. In ideally balanced Fe-ODS GARS alloys, the heavy Y atoms in matrix and in IMCs are nearly immobile, so more mobile oxygen diffuses into the matrix after hot consolidation and is taken up by Y, forming the most thermodynamically stable oxide after dissolution of metastable surface oxide. Previous work showed that the oxides that formed were affected by the Y/Hf ratios; when  $Y/Hf < 1$ , dispersoids formed more as  $HfO_2+Y$ , and when  $Y/Hf > 1$ , dispersoids formed more as  $Y_2O_3+Hf$  [9]. The Y/Hf ratios for CR-200 and CR-204 are 0.375 and 1, respectively. EDS data is not sufficient to determine the exact compositions of the oxides and IMCs present, so future work will need to include detailed XRD to identify the behavior of Y and Hf in both of these alloys.

## 5.5 Conclusion

Vacuum hot pressing was able to successfully generate a sintered compact to ~90% density in the as-VHP state using CR-200 and CR-204 GARS precursor alloys. Upon VHP, the alloys showed their highest hardness. This was expected, as no further work hardening was introduced to increase the dislocation densities or decrease grain size of the alloys before heat treating. After heat treatment, both alloys showed greater hardness after 2.5h at 1200°C than at 1100°C, due to better sintered microstructures with increased densities. CR-200 showed decreased hardness after 12h at 1200°C as compared to 2.5h, which was expected, because of

IMC and dispersed phase coarsening accompanied by grain growth. CR-204, however, showed increased hardness after 12hrs at 1200°C. CR-204 had an unprecedentedly high Y content compared to the other Y alloys. Future work should characterize fully the effect of the high Y content in the alloy.

## CHAPTER 6. COLD SPRAY CONSOLIDATION STUDY

### 6.1 Background

For the GARS method of manufacturing ODS materials to surpass traditional MA pathways, the dislocation densities present must be equal to those in the MA materials to achieve high hardness and to present enough nucleation sites for sufficient nano-metric dispersoid formation to gain effective strengthening. except for GARS powders with diameters  $< 5\mu\text{m}$ , which were found to contain a supersaturated solid solution of Y in Fe-Cr, but a typical atomization yield batch is  $< 5\%$  superfine powder. Thus, as GARS precursor powder is atomized only, dislocations must be introduced post-powder processing, e.g. by short time ball milling. However, cold spray (CS) deposition offers a dynamic consolidation method, in which the powder particles are deformed as they are consolidated. The benefit of deforming the precursor-powder before heat treatment is two-fold, as it potentially both introduces the needed dislocation densities into the powder as nucleation sites for dispersoids during subsequent heat treatment, and in deforming the powders from their as-atomized spherical condition, the diffusion distance for the oxygen to travel from the surface Cr-oxides to the now-dispersed Y-containing intermetallics during heat treatment is reduced. This study aimed to further validate use of CS deposition for GARS precursor powders. Much of the initial work is described in reference [54], and was completed in collaboration with the Applied Research Laboratory of Pennsylvania State University.

#### 6.1.1 Cold Spray Deposition

CS is a solid-state deposition process that is completed well below the material's melting point by injecting metal powders into heated supersonic gasses and depositing them onto a



substrate (figure 6.1). Powders are commonly injected into a  $N_2$  or He (or  $N_2 + He$ ) gas stream reaching speeds of up to 1000 m/s, and may be heated up to 1000°C, depending on furnace capacity [55]. Upon impact, the powder particles experience plastic flow, promoting full densification and cold welding of the deposition [55]. Thin oxide films on powder particles are disrupted during the extensive plastic flow upon impact, allowing for metallurgical and mechanical bonding [55].

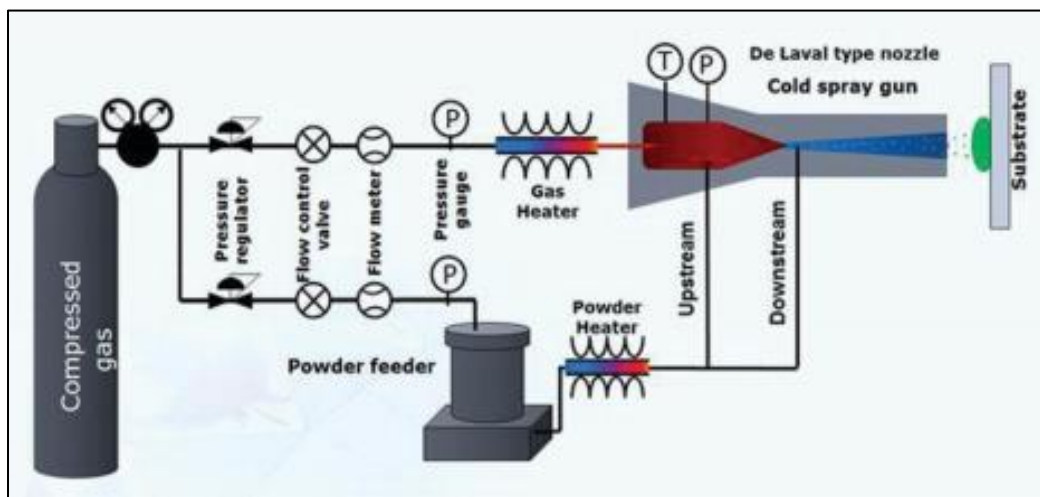


Figure 6.1: Schematic of CS deposition process [55]

Cold spray (CS) deposition would allow for formation of pre-forms in near-net shape that are ready for processing into thin-wall (dia. = 0.5  $\mu\text{m}$ ) cladding tubes by depositing powder onto an Al mandrel that can later be removed. Recent work with NFAs for next generation nuclear applications used CS-deposition to make near-net shape tubes from conventional inert gas atomized 14YWT (Fe-14.8Cr-0.9W-0.5Ti-0.1Y-0.03O at%) from Los Alamos National Laboratory (LANL) by depositing onto an Al mandrel [56]. The researchers were successful in generating near-net shape tubing, but the O content of the feedstock powder (without GARS processing) was lower than needed for sufficient formation of (Y, Ti)-O nanoclusters, and

consequently hardness decreased below desired lower limits after annealing due to recrystallization [56]. Fe-ODS alloys have been successfully applied as a surface coating to existing Zircaloy-4 cladding tubes, and improved mechanical properties were seen at room temperature, 500°C, and under LOCA simulation conditions [20]. However, CS tubing entirely made from Fe-ODS materials of the desired hardness, density, and proper stoichiometry has yet to be generated.

CS of GARS Fe-ODS precursor powders is attractive because of the low hardness of the powders in their as-atomized state. It is expected that the powders would deform easily onto a removable Al mandrel to form tubing, and then through further TMT the desired dislocation densities and hardness may be achieved. A flat coupon of CR-200 alloy was generated for the purpose of this limited study to explore this concept.

## **6.2 Experimental Methods**

### **6.2.1 CS Sample Generation**

Ames Lab GARS Fe-ODS precursor powder CR-200 with composition Fe-16Cr-12Al-0.9W-0.25Hf-0.2Y (at%) and size cut -53/+20 $\mu$  (D50=35.91 $\mu$ m) was sent to the Applied Research Laboratory for CS deposition. The powder was cold sprayed onto an Al 6061 build plate with N<sub>2</sub> accelerating gas heated to 575°C. One pass was made at 60° to the build plate, and 93 passes were made at 90°, with the powder feeder at 1.1 and 3 rpm, respectively. The completed deposition was sectioned into smaller samples for analysis. Unfortunately, no record of sample location on the build plate was kept. A stitched cross sectional cut of the build revealed a density gradient. The gradient was quantized via ImageJ threshold analysis [52].

### 6.2.2 Microscopy and Microhardness

Cut sections of the as-built sample were imaged in the SEM, including EDS and EBSD map analysis, and analyzed via differential scanning calorimetry (DSC). Vickers microhardness measurements were taken on the top surface of the build (// to build direction) after removal from the Al6061 substrate (figure 6.2).

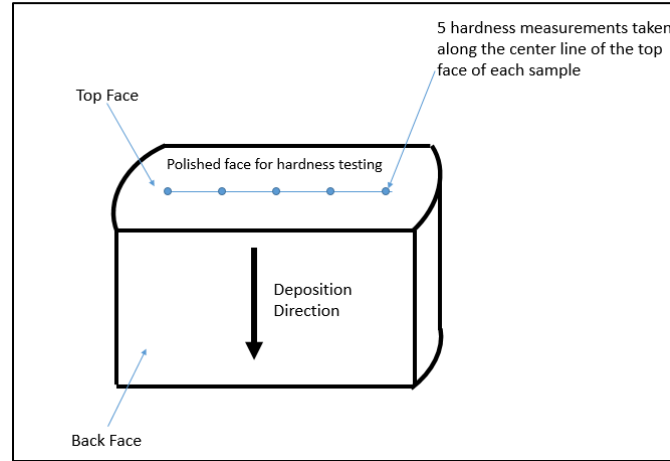


Figure 6.2: Schematic of five hardness measurements taken along the top face of sample cut from as-CS specimen

#### 6.2.2.1 Deadweight annealing

A deadweight anneal was conducted on one sample at 750°C for 3 hours with a 3 MPa load, and again at 1000°C with a 5 MPa load for 3 hours. The resulting sample was sectioned and polished for EDS analysis and hardness testing. Further results of the dead weighting treatments can be found in reference [54].

#### 6.2.1 Differential Scanning Calorimetry

Two samples cut from the as-built specimen were analyzed via DSC in a Netzsch DSC 404 C calorimeter at heating rate of 20K/min. The samples were cut using a low-speed diamond saw to reduce the deformation introduced by the cutting process. Unfortunately, no record was

kept mapping where the sample was located in the original build specimen. Sample 1 weighed 166.6 mg, and Sample 2 weighed 176.3 mg. To avoid oxidation during DSC analysis, the experiments were carried out under a He atmosphere. The maximum temperature of the DSC scans was 1200°C, with a one-hour hold, and then the sample cooled to room temperature (figure 6.3). After the first scan, the measurement was repeated to allow for observation of differences in the as- built and annealed microstructures [57]. The change in heat released or absorbed by the sample allowed for experimental determination of dislocation/stored energy release. Due to the global pandemic, the DSC run of sample 2 was delayed until stay at home orders were over, and consequently a new baseline was run for sample 2 as baseline correction procedures are critical for the small heat effects of solid state reactions [57].

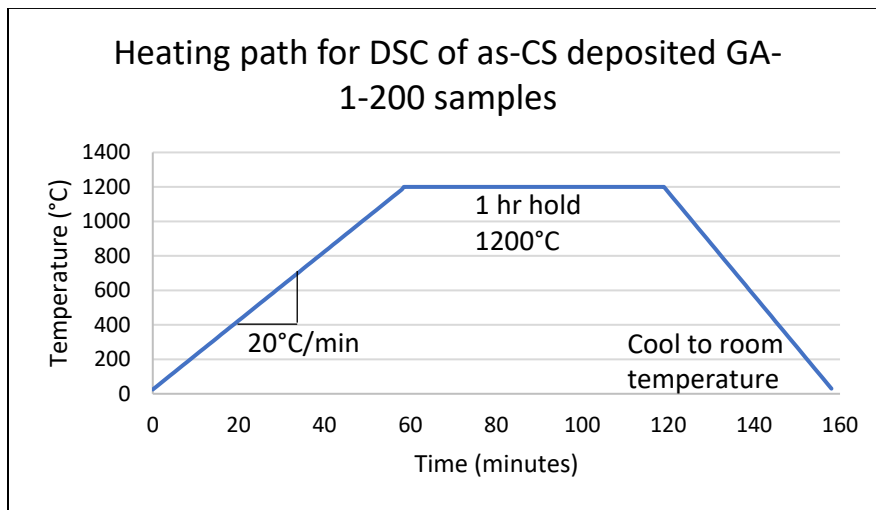


Figure 6.3: Heating path for DSC of as-CS deposited GA-1-200 samples. This path was repeated twice for each sample.

## 6.3 Results

### 6.3.1 CS Sample Generation

The CS specimen had CR-200 deposition thickness of 4.318 mm. An image of the sample was taken after a cross section cut (figure 6.4).

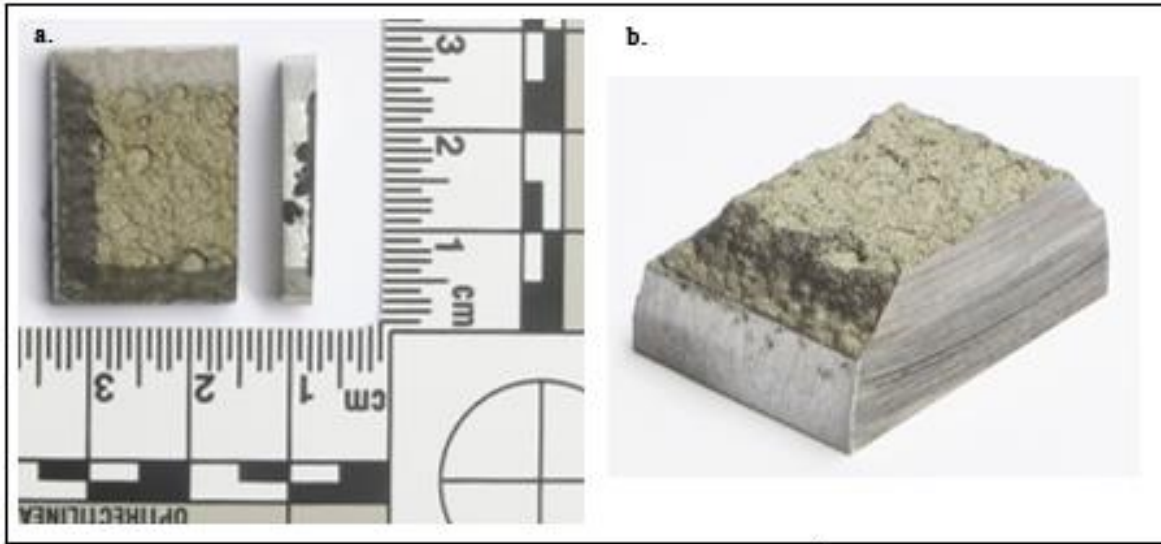


Figure 6.4: As-deposited cold sprayed sample of GARS powder onto aluminum substrate, (a) showing top down view of deposit and slice off of deposit, and (b) showing cross sectioned surface as-cut [54]

One sample cut from the CS deposited specimen had average porosity of 7%. A stitched secondary electron image was generated to capture the entire cross section of the deposition, and revealed a porosity gradient in the deposition direction, with the densest layers at the bottom. ImageJ was used to calculate the porosity gradient across the sample in 1 mm slices on the YZ plane (figure 6.5). The results of the ImageJ analysis are reported in table 6.1. Sections 1-4 are 1 mm in height, but section 5 is 0.73 mm in height.

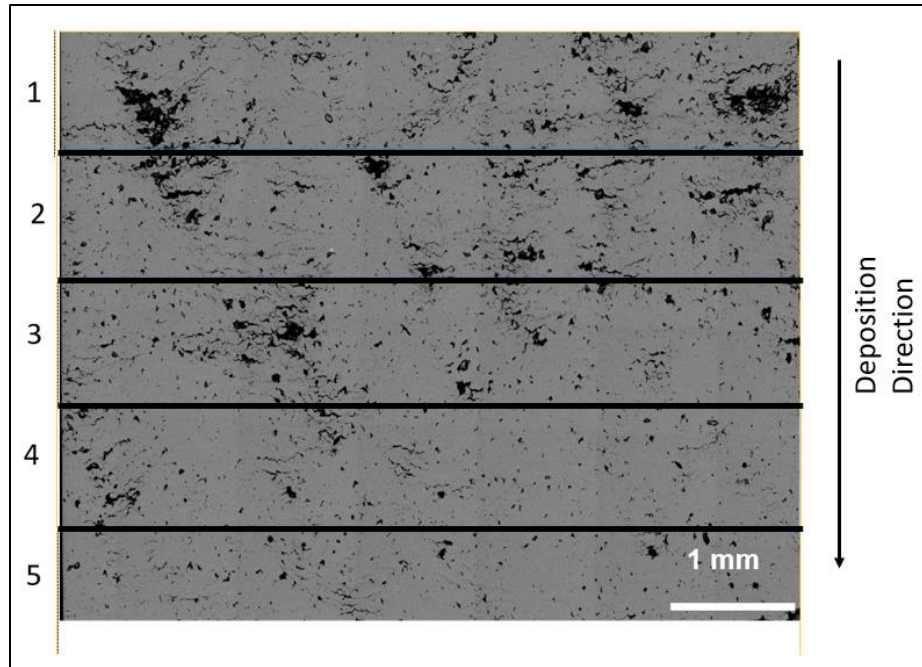


Figure 6.5: GA-1-200 CS Deposited Sample Porosity Gradient. Sections 1-4 are 1 mm in height, section 5 is 0.73 mm high.

Table 6.1: GA-1-200 CS deposited sample porosity gradient by section area

Section	% Porosity
1	10.5%
2	8.43%
3	6.80%
4	4.41%
5	3.85%
Average	6.79%

### 6.3.2 Microscopy and microhardness

The powders in the specimen were plastically deformed beyond their yield stress, as shown by drastic change from their as-atomized spherical morphology in figure 6.6, below.



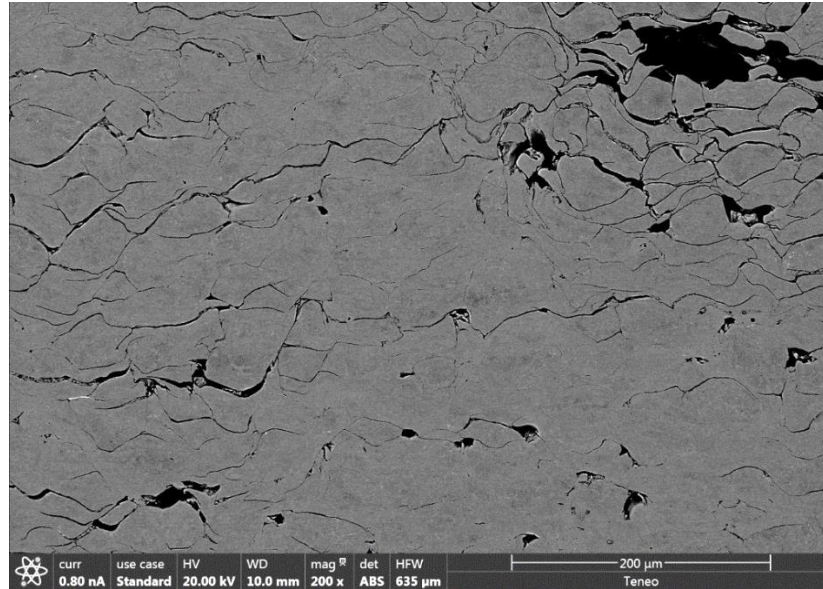


Figure 6.6: Backscattered SEM image of as-CS deposited CR-200 powder. Deposition direction points down in plane with the page [54]

The interior “web” of IMCs that follow the interdendritic or intercellular boundaries that are characteristic of the solidification microstructure of the as-atomized Fe-ODS GARS powders was still visible at higher magnifications, though highly stretched and deformed (figure 6.7).

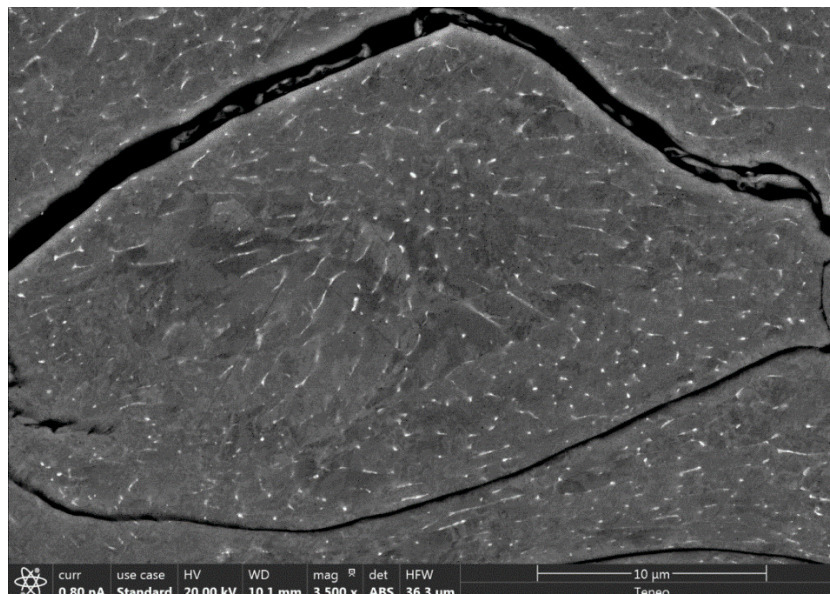


Figure 6.7: BSE SEM image of deformed CR-200 alloy powder particle in the as-CS deposited sample. Deposition direction points down in plane with the page [54]

A EBSD map of as-CS grain structure (figure 6.8) also showed significant deformation.

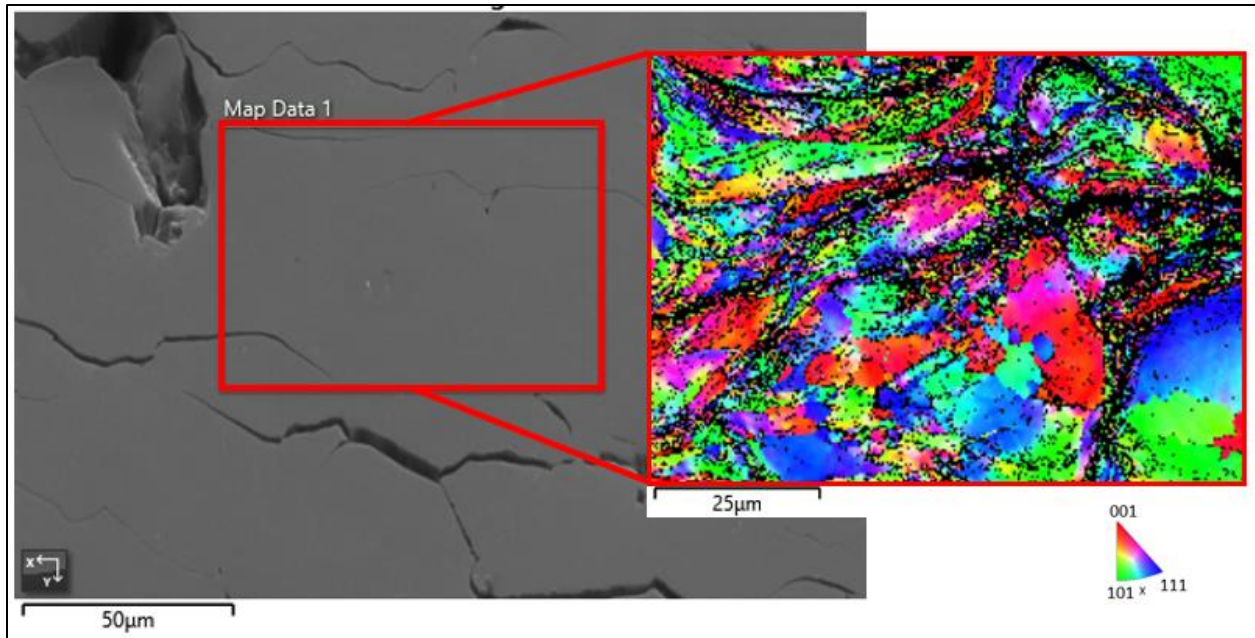


Figure 6.8: EBSD of as-CS grains from CR-200

#### 6.3.2.1 Deadweight annealing

One sample was deadweight annealed at 750°C for 3h with a 3 MPa load, then again at 1000°C with a 5 MPa load. Stacked EDS and EBSD data of the as-annealed microstructures are shown below (figures 6.9 and 6.10).

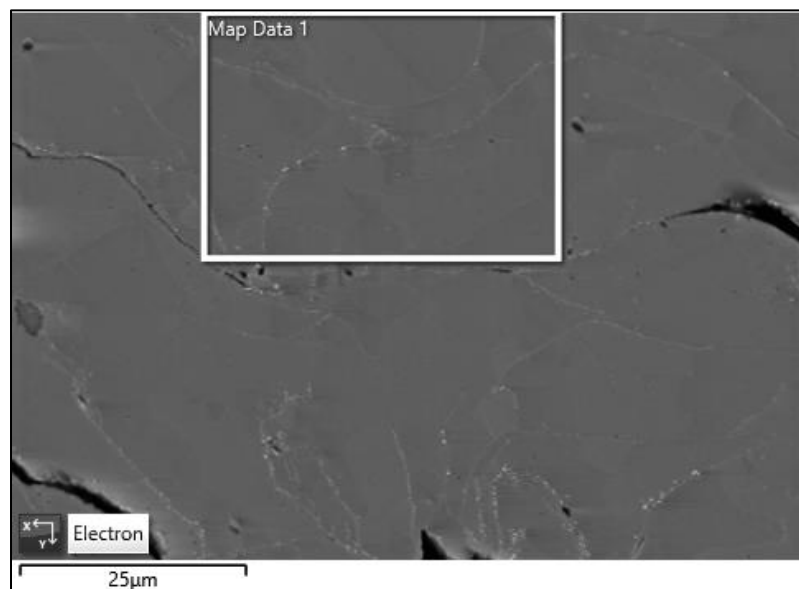


Figure 6.9: Reference location for the annealed EDS/EBSD data. Scale bar is 25μm



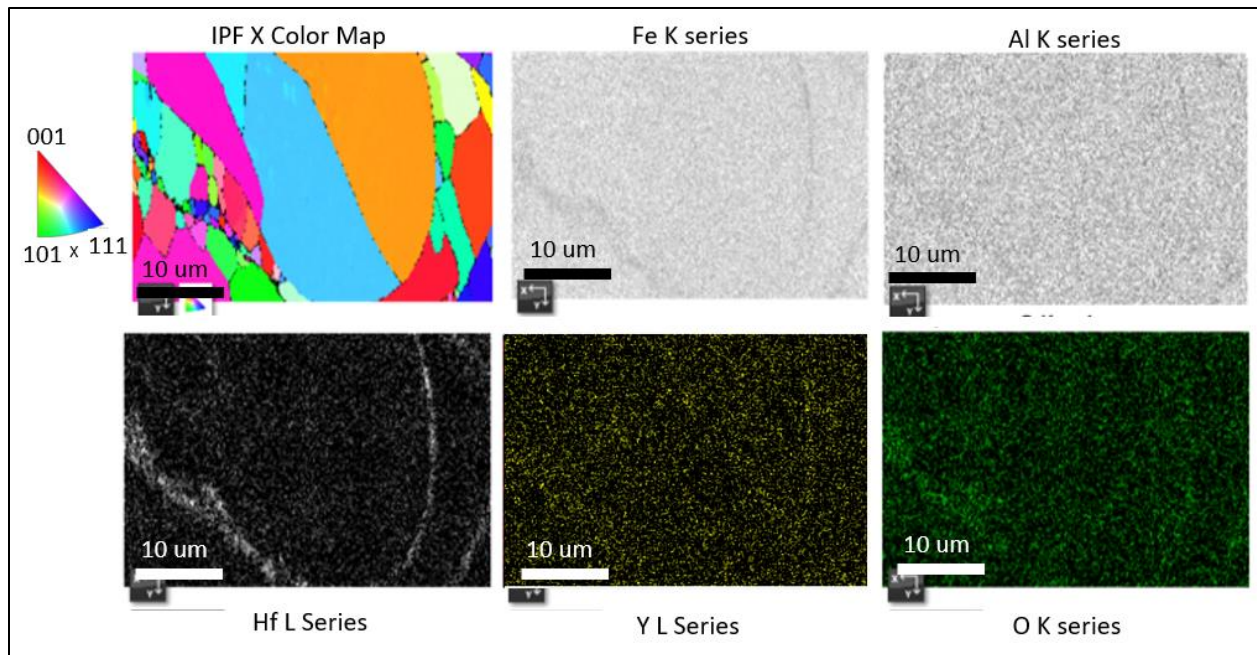


Figure 6.10: EBSD map and EDS series spectra for annealed CR-200 sample. W, Cr, and C series were also captured, but showed even distribution across the scan, and thus are not included here.

Point spectrum EDS analysis (table 6.2) was conducted to further identify the phases present in the annealed microstructure (figure 6.11)

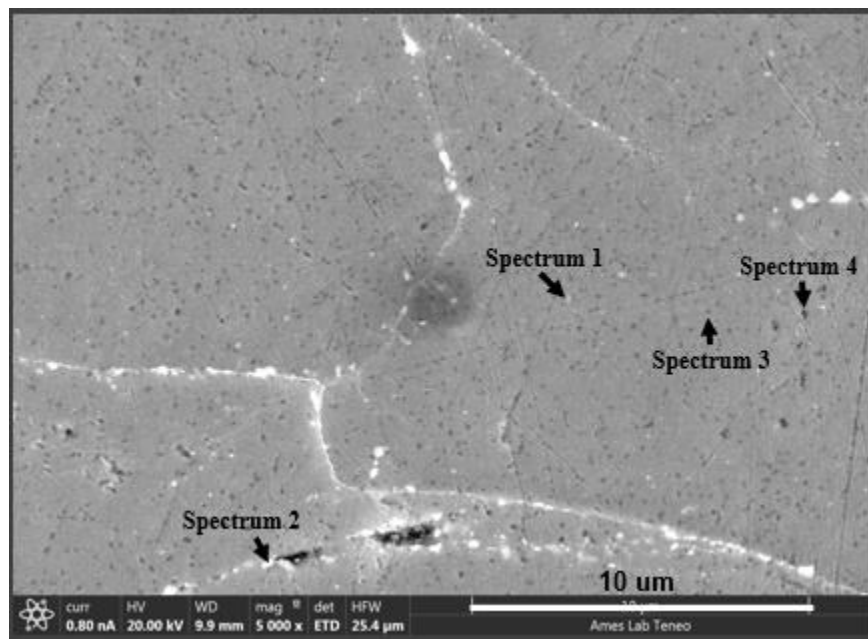


Figure 6.11: Post-CS annealed BSE image with EDS spectra noted

Table 6.2: Point Spectrum EDS analysis of post-CS annealed microstructure

Spectrum	Fe (at%)	Cr (at%)	Al (at %)	W (at%)	Hf (at%)	Y (at%)	O (at %)
Spectrum 1	69.03	15.28	10.9	1.13	1.71	0.21	1.74
Spectrum 2	68.02	16.07	12.02	0.94	0.08	0	2.86
Spectrum 3	66.42	15.69	11.8	0.86	0.09	0	5.14
Spectrum 4	50.47	13.12	7.78	0.61	9.93	0	18.1

### 6.3.2.2 Differential Scanning Calorimetry

For DSC Sample 1, only the heating portion of the scan was recorded. Consequently, only the heating portion of DSC sample 1 data are reported here (figures 6.12 and 6.13). For DSC sample 2 both the heating and cooling curves were collected (figures 6.14, 6.15, and 6.16). The heating and cooling curves already have the baseline data (empty pan) subtracted. However, the baseline run is included on some plots to identify any bumps on the baseline scan to prevent misinterpreting as signal from the sample.

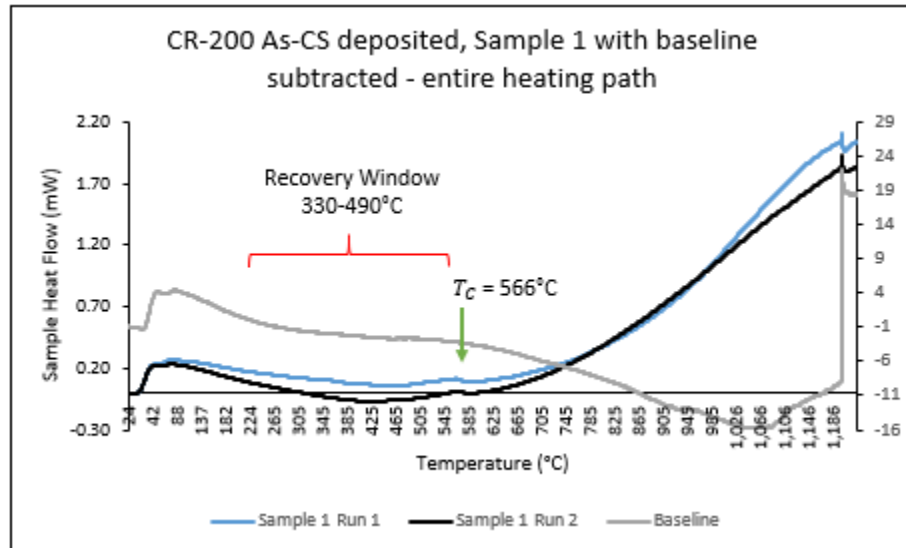


Figure 6.12: CR-200 As-CS deposited, DSC sample 1 with baseline subtracted, entire heating path. Suspected dislocation recovery window and curie temperature marked

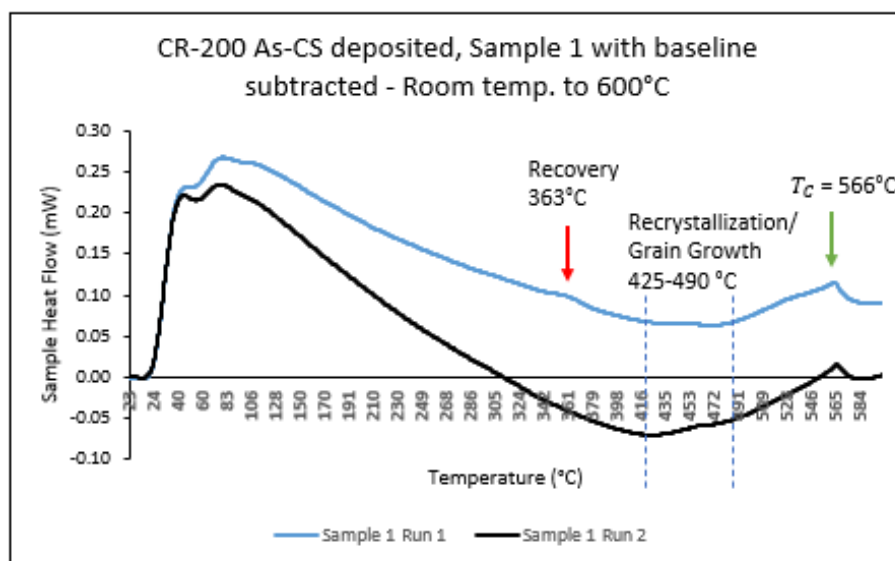


Figure 6.13: CR-200 As-CS Deposited, DSC sample 1 with baseline subtracted, room temperature to 600°C. Suspected dislocation recovery and recrystallization/grain growth marked, in addition to  $T_c$

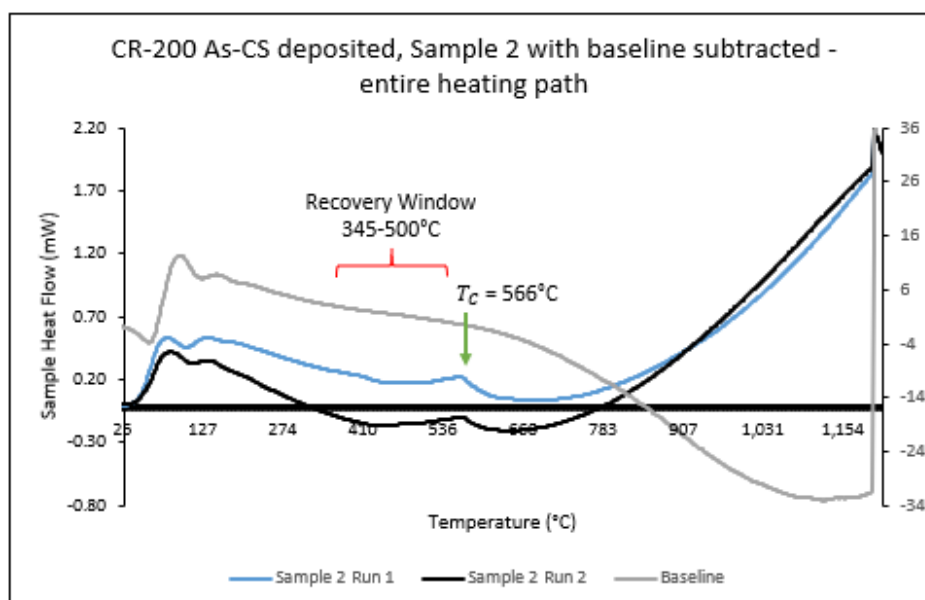


Figure 6.14: CR-200 As-CS DSC sample with baseline subtracted, entire heating path. Suspected dislocation recovery window and curie temperature marked

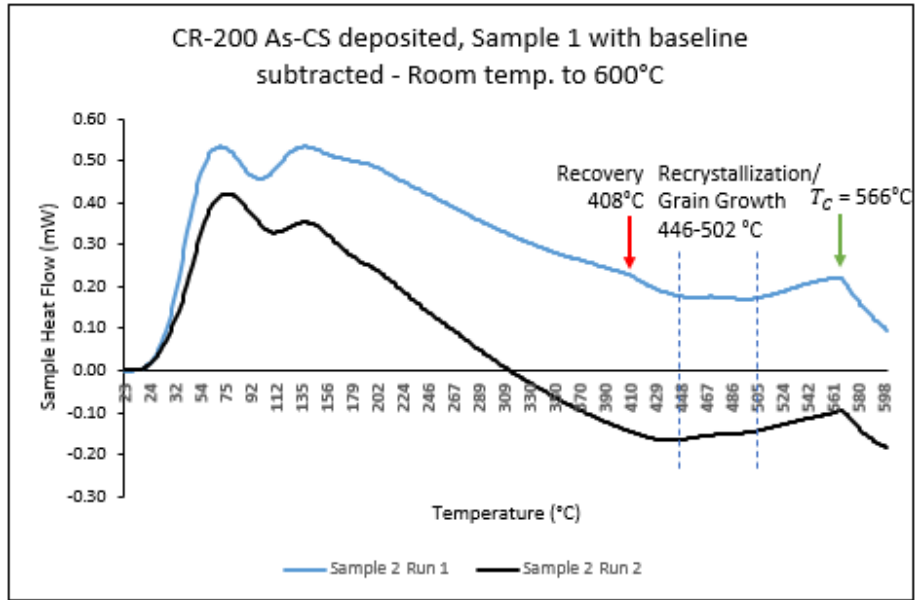


Figure 6.15: CR-200 As-CS Deposited, DSC sample with baseline subtracted, room temperature to 600C. Suspected dislocation recovery and recrystallization/grain growth marked, in addition to  $T_c$

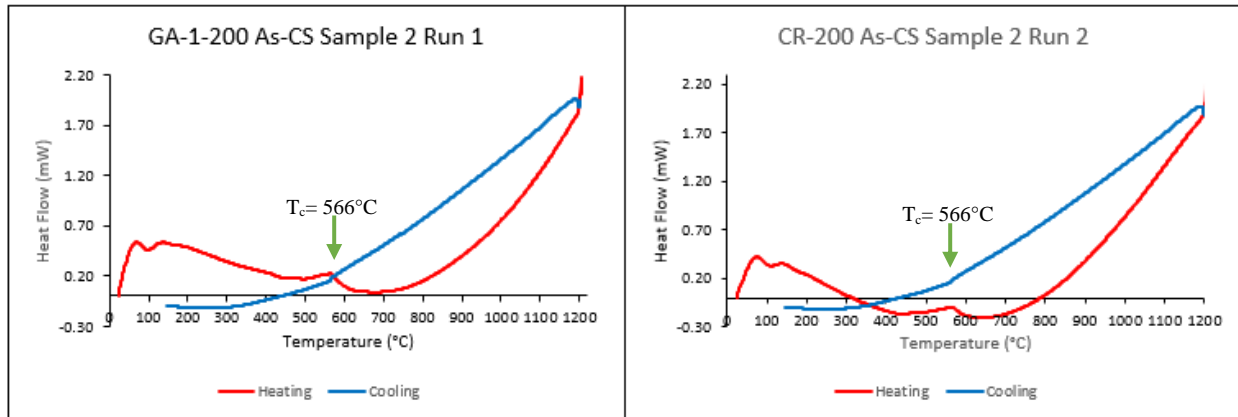


Figure 6.16: CR-200 As-CS Deposited DSC sample 2 heating and cooling for runs 1 and 2.

There is no noise in the cooling curve that matches suspected the recovery and recrystallization/grain growth from the heating curve.  $T_c$  is present in the heating and cooling curves.

## 6.4 Discussion

### 6.4.1 Cold Spray Coupon Generation

A flat coupon sample of CR-200 was successfully cold sprayed to a thickness of 4.318 mm. However, the average porosity of the specimen was ~7%. With HIP consolidation of MA materials, densities of 98% can be achieved, and consequently, a greater density was desired for the CS sample, especially to obtain meaningful hardness measurements to track oxide dispersoid nucleation [44]. In order to achieve a greater density, the CS deposition process could be tuned to a higher temperature of deposition, or a faster propellant gas (i.e. He) (figure 6.17) [41]. Unfortunately, the furnace at Penn State ARL could not go beyond 575°C. In an effort to save He, a 50-50 mix of He and N<sub>2</sub> has been shown to be effective for increasing deposition density at 4MPa pressure as compared to 100% N [41]<sub>2</sub>. Addition of He to the propellant gas did require lower temperatures for deposition, due to the higher specific heat ratio and molecular weight of He than N<sub>2</sub> [41].

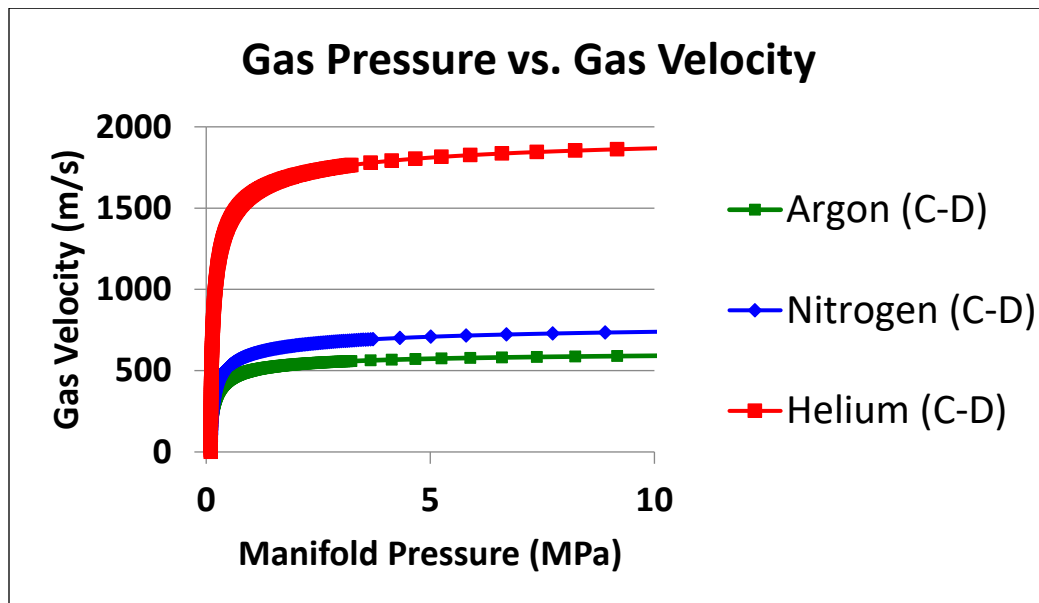


Figure 6.17: Gas manifold pressure vs. gas velocity for He, N<sub>2</sub> and Ar [58]

Also, although early literature on CS reported spherical powders as superior feedstock [59], more recent studies have found that more abnormally shaped powders are accelerated to greater velocities in the propellant gas, and consequently deform more upon impact, generating a denser compact [60, 61]. Other works have studied the influence of the substrate material, and have found that a harder substrates allow for greater particle deformation upon impact, thus generating a denser sample [41]. Overall, there are several variables that could be adjusted to increase the density of the as-CS deposited sample.

#### **6.4.2 Microscopy and Microhardness**

EBSD of the as-deposited sample showed a dramatically bimodal grain size distribution, with observed grain sizes varying from 10's of  $\mu\text{m}$  down to  $<1\mu\text{m}$ . EDS showed a greater concentration of Fe, Hf, and O around areas with smaller grain sizes, and Y showed a fairly even distribution across the entire map. This suggests that the high deformation from the CS process distributed the segregated Y in the matrix, whereas the Hf may have been mainly in on the PPBs before CS, as it is now located primarily along deformed PPBs. Further work with CS of Fe-ODS GARS precursor powders should include higher resolution EBSD and EDS analyses to identify with greater precision the location of the elements in the as-atomized powder and where they go after CS deposition.

##### **6.4.2.1 Vickers Microhardness**

Although the as-deposited sample had an average of 7% porosity, hardness measurements were taken from the top of the sample down parallel to the deposition direction. Unsurprisingly, the CS process dramatically changed the hardness of the sample due to the high level of retained cold work in the as-deposited sample (as-CS) (figure 6.18). The hardness was compared to the

annealed state, which saw significant reduction, but is still higher than that of the as-vacuum hot pressed hardness given in chapter 5.

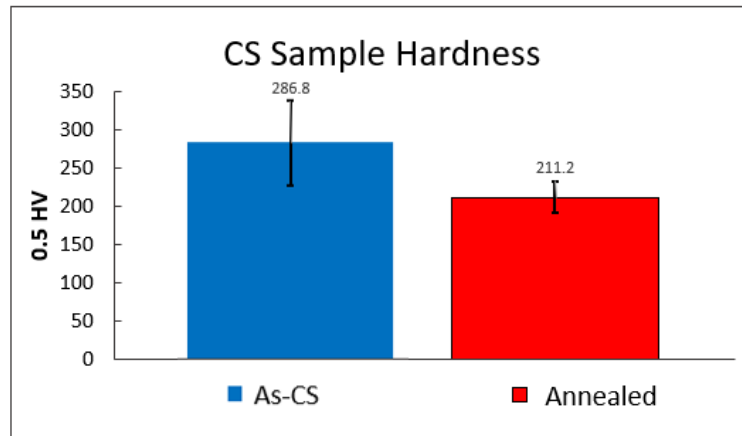


Figure 6.18: Vickers microhardness of CR-200 alloy as-CS and as-annealed

The large standard deviation in hardness measurement for the as-CS samples is attested to the high porosity of the sample, and also to a lesser degree due to the dynamic recrystallization that occurs at particle and particle-substrate interfaces due to severe plastic deformation (SPD) during the CS process, resulting in local increases in hardness, which may be isolated in pockets along the hardness trace [61]. The overall increase in hardness is caused by the heavy work hardening and plastic deformation beyond the yield stress of the powder during the CS process, resulting in dramatically increased dislocation densities.

Post-CS, depositions are typically annealed to release some of the stored energy to increase ductility and grain growth to improve creep resistance [55]. EDS analysis of the annealed microstructure revealed Al on the PPBs and in the interior of the previous particles, and some O containing phases in the interior of PPBs, including Y-Hf-O phases. This result is promising, as very little O-dispersion away from the PPBs was seen in the VHP sample of CR-

200. DSC analysis revealed the temperature at which stored energy in the CS sample was released.

### 6.4.3 DSC Analysis

DSC is often used with severe plastic deformation (SPD) of materials to identify solid state reactions in materials processed via SPD methods, and also can be used to evaluate the effectiveness of new processing method for improving the thermomechanical properties of materials [57, 62]. In this case, DSC was used to verify the presence of stored energy from the CS process without using TEM to image dislocations, and to identify the temperature at which the stored energy was released from the material.

DSC sample 1 and sample 2 had a strongly observable curie temperature at 566°C, which was lower than shown on the Fe-Cr phase diagram (figure 6.16) [47]. However, it is suspected that the alloying additions, especially W and Al suppressed the transformation from ferromagnetic to paramagnetic from the temperature of the binary Fe-Cr system. The  $T_c$  ordered to disordered transformation is present on both the heating and cooling curves for sample 2 (figure 6.19) due to slight hysteresis of the transformation.

This temperature range for observed recovery and recrystallization is similar to a study of Fe<sub>3</sub>Al alloy (bcc), where recovery was observed at about 300°C, and recrystallization took place at  $T \geq 570^\circ\text{C}$  [63]. In another study, DSC analysis of a cold rolled ferritic steel showed exothermic heat release of stored energy from the 85% reduction over a range of temperatures from 400-580°C [64].



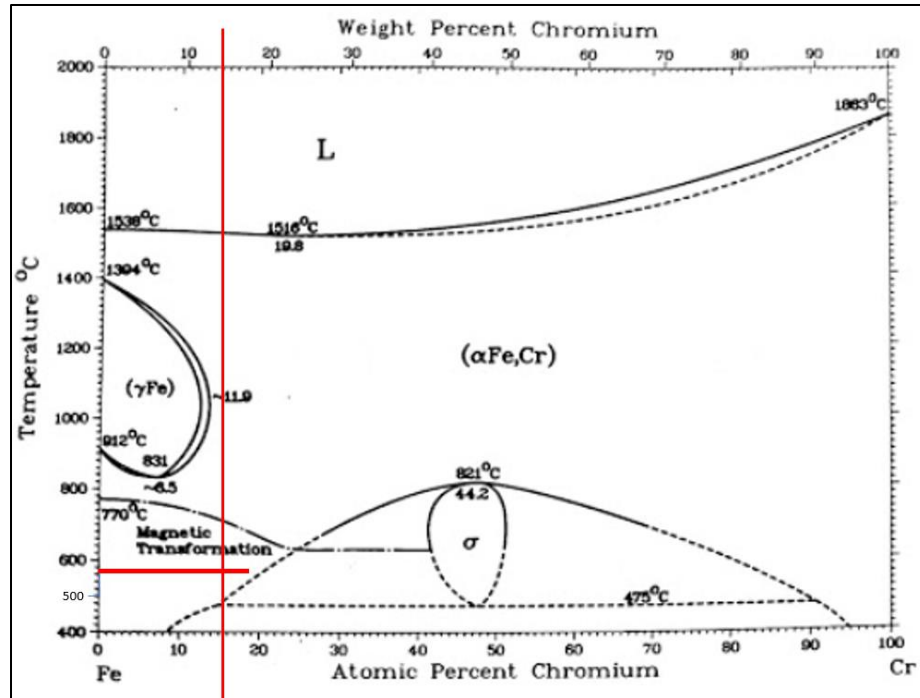


Figure 6.19: Fe-Cr phase diagram. Adapted from [47]

Unfortunately, the location from which each of the CS samples was cut from the original deposition was not recorded. Geometric effects on particle velocity and deformation have been well defined [61], but were not known to the author at the time of cutting the CS sample. However, it is highly probable that the two samples submitted for DSC analysis were not cut from the same area of the CS deposited coupon. The observed difference in recovery temperatures between the two DSC samples is within range for samples deformed to different amounts of cold work. The difference in the amount of deformation in one sample could have been due to varying CR-200 particle sizes that are known to have varying surface oxide layer thickness [9], spray angle, and the position of particles in the jet, among other variables (figures 6.20 and 6.21) [61].

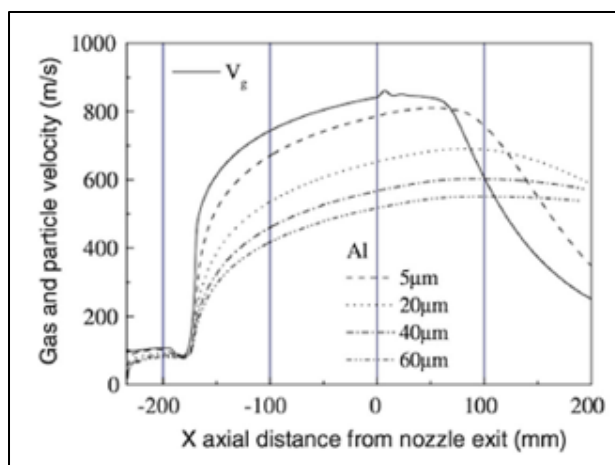


Figure 6.20: Axial gas and particle velocity of Al powders of different sizes [61]

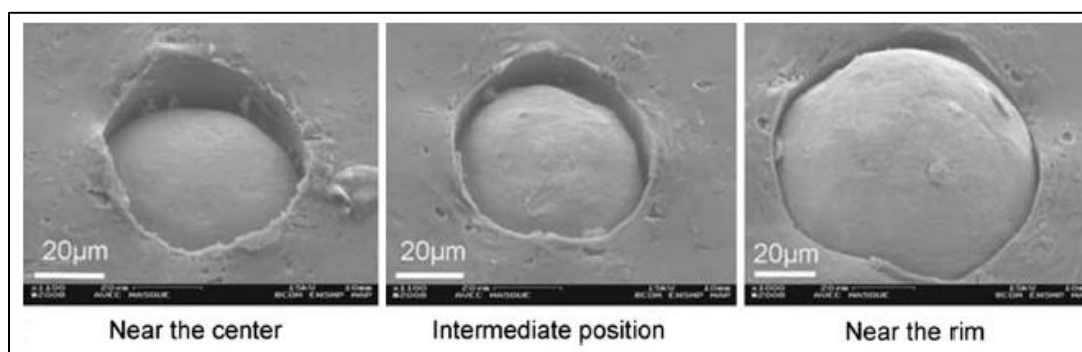


Figure 6.21 : Different splat morphologies and substrate penetration depth as a function of spraying positions in the propellant gas jet [61]

## 6.5 Conclusion

Cold spray deposition of CR-200 GARS Fe-ODS precursor powder was successful in generating a 93% dense coupon. The hardness of the as-deposited sample increased 1.5x beyond that of the as-VHP sample. DSC analysis revealed an independent recovery event when dislocations accumulated during CS deposition were released and able to annihilate. There are many variables that should be improved moving forward with CS of the powder, including increasing impact velocity of the powder by using He as the propellant gas or by increasing the temperature of the propellant gas. Similarly, the substrate material could be exchanged from Al-

6061 to a harder material to increase the deformation of the CR-200 powder, and the adjustments of temperature of the substrate material could also be explored.

## CHAPTER 7. CONCLUSIONS

First-generation Fe-ODS GARS precursor powders have been extensively researched to characterize their behavior both in the as-atomized state and after HIP consolidation with further processing (e.g., hot or cold rolling). In this study, two first-generation Fe-ODS GARS precursor powders were consolidated via methods novel to GARS processing, i.e., vacuum hot press consolidation and cold spray deposition. The effects of the two processing methods on ODS alloy microstructure were evaluated in order to extend understanding of the consolidation behaviors of these alloys and in hopes of identifying a potential consolidation method that is ideally suited for Fe-ODS GARS precursor powders. Both alloys selected for the experiments had been previously developed under DOE-Fossil Energy Office funding and, consequently, the alloys contained Hf for  $\text{Y}_2\text{Hf}_2\text{O}_7$  dispersoids to develop after hot consolidation (i.e. HIP) or post consolidation and heat treatment as the strengthening dispersoid phase. Work by Kimura et al. has shown that either Hf or Zr additions can be added to Fe-ODS alloys produced by traditional MA routes in order to act as dispersion strengthening components to prevent formation of Y-Al oxides subject to coarsening at elevated temperatures [48, 49], and thus the existing CR-200 (Fe-15.5Cr-12.1Al-0.98W-0.24Hf-0.09Y-0.14O at%) and CR-204 (Fe-15.5Cr-0.91W-0.24Hf-0.24Y-0.14O at%) powders were used for this study of consolidation behaviors with the understanding that new, Zr-modified (non-Hf) containing Fe-ODS GARS precursor powder alloys would need to be generated for application in nuclear power plant environments, due to the detrimental effects of Hf in radiation environments.

Vacuum hot press consolidation generated powder compacts with ~90% density, and a procedure was written for consolidating the powders at 100MPa for 850°C for 4 hours. The as-pressed alloys retained the as-atomized cellular structure of segregated Y-Hf IMC in the particle

interiors. Heat treatment at 1100°C and 1200°C resulted in reduction in hardness, due to insufficient oxygen content of the alloys for generation of the desired oxide dispersoid content, which allowed for unhindered grain growth. IMCs and some oxide phases developed on PPBs, and coarsened to sizes on the order of  $\mu\text{m}$  with the 12hr heat treatment at 1200C. Overall, it was recommended that if vacuum hot pressing is going to be pursued in the future for consolidation of Fe-ODS GARS precursor powders, higher pressures will need to be applied ( $\geq 200 \text{ MPa}$ ) to promote full densification and non-reactive die liners not subject to crushing during pressing will need to be identified. If these are found, larger scale production of ingots or billets could be explored for rolling into Fe-ODS sheet materials.

CR-200 was deposited via cold spray deposition at the Applied Research Laboratory. The test coupon was sectioned for hardness, microscopy, and DSC analysis. The as-deposited specimen was shown to have ~93% density. DSC analysis showed evidence of recovery and recrystallization taking place between  $\sim 345^\circ$  and  $500^\circ\text{C}$ . Cold spray literature confirms that deformation of powders during the CS process is heavily dependent on powder position geometrically on the build substrate and also within the powder accelerating gas. DSC applications in SPD literature have shown an increase in recovery temperature with increased deformation. Consequently, of the two samples, the 2<sup>nd</sup> was likely deformed to a higher degree during the CS process, resulting in a higher temperature recovery. CS showed promise for introducing deforming Fe-ODS GARS powders to a sufficiently to generate necessary dislocation densities for adequate nano-metric oxide dispersion nucleation sites. If CS is to be pursued as a method of generating Fe-ODS GARS alloy materials, the CS process must be tuned (accelerating gas composition, temperature, substrate type, temperature) to generate a higher density as-deposited specimen.

## REFERENCES

- [1] G.R. Odette, M.J. Alinger, B.D. Wirth, *Annual Review of Materials Research* 38 (2008) 471-503.
- [2] E. Aydogan, S. Pal, O. Anderoglu, S.A. Maloy, S.C. Vogel, G.R. Odette, J.J. Lewandowski, D.T. Hoelzer, I.E. Anderson, J.R. Rieken, *Materials Science & Engineering A* 661 (2016) 222-232.
- [3] C.P. Massey, S.N. Dryepondt, P.D. Edmondson, K.A. Terrani, S.J. Zinkle, *Journal of Nuclear Materials* 512 (2018) 227-238.
- [4] M.A. Auger, V. de Castro, T. Leguey, S. Lozano-Perez, P.A.J. Bagot, M.P. Moody, S.G. Roberts, *Materials Science & Engineering A* 671 (2016) 264-274.
- [5] R. Klueh, J.P. Shingledecker, R. Swindeman, D. Hoelzer, *Journal of Nuclear Materials* 341 (2005) 103-114.
- [6] I.E. Anderson, B.K. Lograsso, T.W. Ellis, Gas atomization synthesis of refractory or intermetallic compounds and supersaturated solid solutions, in: U.S. Patent (Ed.) 1993.
- [7] I.E. Anderson, R.L. Terpstra, Dispersoid reinforced alloy powder and method of making, in: U.S. Patent (Ed.) 2014.
- [8] I.E. Anderson, J.R. Rieken, Dispersoid reinforced alloy powder and method of making, in: U.S. Patent (Ed.) 2008.
- [9] J.R. Rieken, Gas atomized precursor alloy powder for oxide dispersion strengthened ferritic stainless steel, *Materials Science and Engineering*, vol Doctor of Philosophy, Iowa State University, Graduate Theses and Dissertations, 2011, p. 335.
- [10] A. Spicher, Effects of aluminum additions to gas atomized reaction synthesis produced oxide dispersion strengthened alloys, Iowa State University Digital Repository, 2014.
- [11] IEA, *World Energy Outlook*, 2017.
- [12] IEA, *Global Energy Review 2020*, International Energy Agency, Paris, 2020.
- [13] *Electricity Explained: Electricity generation, capacity, and sales in the United States*, vol 2020, U.S. Energy Information Administration, eia.gov, 2020.
- [14] IEA, *Sustainable Recovery*, International Energy Agency, Paris, 2020.

- [15] P.M. Forster, H.I. Forster, M.J. Evans, M.J. Gidden, C.D. Jones, C.A. Keller, R.D. Lamboll, C.L. Quéré, J. Rogelj, D. Rosen, C.-F. Schleussner, T.B. Richardson, C.J. Smith, S.T. Turnock, *Nature Climate Change* (2020).
- [16] Pocket Guide, in: W.N. Association (Ed.) 2018-2019.
- [17] W.N. Association, *Nuclear Power Reactors*, vol 2020, World Nuclear Association, 2020.
- [18] W.N. Association, *Physics of Uranium and Nuclear Energy*, vol 2020, Word Nuclear Association.
- [19] U.S.N.R. Commission, *Safety of Spent Fuel Storage Brochure*, 2017.
- [20] H.-G. Kim, I.-H. Kim, Y.-I. Jung, D.-J. Park, J.-H. Park, J.-H. Yang, Y.-H. Koo, *Additive Manufacturing* 22 (2018) 75-85.
- [21] F.E.M. Institute, *Unit 4: Nuclear Power Plant Accidents, Power Plant Safety Features*, vol 2020.
- [22] W.N. Association, *Fukushima Daiichi Accident*, vol 2020.
- [23] K.A. Terrani, *Journal of Nuclear Materials* 501 (2018) 13-30.
- [24] L.J. Ott, K.R. Robb, D. Wang, *Journal of Nuclear Materials* 448 (2014) 520-533.
- [25] R.E. Reed-Hill, *Physical metallurgy principles* / Robert E. Reed-Hill, Reza Abbaschian, Boston : PWS-Kent Pub., Boston, 1992.
- [26] A. Kelly, *Strengthening methods in crystals*. Edited by A. Kelly and R. B. Nicholson, New York, Halsted Press Division, Wiley, New York, 1972.
- [27] T.H. Courtney, *Mechanical behavior of materials* / Thomas H. Courtney, Long Grove, Ill. : Waveland Press, Long Grove, Ill., 2005.
- [28] M.A. Meyers, K.K. Chawla, *Mechanical Behavior of Materials*, Cambridge: Cambridge University Press, Cambridge, 2008.
- [29] A.M. Russell, *Structure-property relations in nonferrous metals* / Alan M. Russell, Kok Loong Lee, Hoboken, NJ : John Wiley, Hoboken, NJ, 2005.
- [30] J. Rösler, E. Arzt, *Acta Metallurgica et Materialia* 38 (1990) 671-683.
- [31] S. Ukai, S. Kato, T. Furukawa, S. Ohtsuka, *Materials Science and Engineering: A* 794 (2020) 139863.

- [32] A. Wasilkowska, M. Bartsch, U. Messerschmidt, R. Herzog, A. Czyrska-Filemonowicz, *Journal of Materials Processing Technology* 133 (2003) 218-224.
- [33] M. Zhang, S.E. Broyles, J.C. Gibeling, *Acta Materialia* 196 (2020) 384-395.
- [34] G.S. Was, *Fundamentals of Radiation Materials Science: Metals and Alloys*, New York, NY: Springer, New York, NY, 2016.
- [35] J. Brodrick, D.J. Hepburn, G.J. Ackland, *Journal of Nuclear Materials* 445 (2014) 291-297.
- [36] P.S. Gilman, J.S. Benjamin, *Annual Review of Material Science* 13 (1983) 279-300.
- [37] *Materials and Processing Report* 5 (1990) 5-6.
- [38] Y. Yamamoto, B.A. Pint, K.A. Terrani, K.G. Field, Y. Yang, L.L. Snead, *Journal of Nuclear Materials* 467 (2015) 703-716.
- [39] K.G. Field, M.A. Snead, Y. Yamamoto, K.A. Terrani, *Handbook on the material properties of FeCrAl alloys for nuclear power production applications*, vol FY18 Version, Oak Ridge National Laboratory, 2018.
- [40] M.E. Alam, S. Pal, K. Fields, S.A. Maloy, D.T. Hoelzer, G.R. Odette, *Materials Science & Engineering A* 675 (2016) 437-448.
- [41] M. Lenling, H. Yeom, B. Maier, G. Johnson, T. Dabney, J. Graham, P. Hosemann, D. Hoelzer, S. Maloy, K. Sridharan, *JOM* 71 (2019) 2868-2873.
- [42] A.S.M. International, *ASM handbook*. 7 (1992).
- [43] D.T. Hoelzer, K.A. Unocic, M.A. Sokolov, T.S. Byun, *Journal of Nuclear Materials* 471 (2016) 251-265.
- [44] C. Capdevila, H.K.D.H. Bhadeshia, *Advanced Engineering Materials* 3 (2001) 647-656.
- [45] J. Meyer, *Advanced gas atomization production of oxide dispersion strengthened (ODS) Ni-base superalloys through process and solidification control*, Iowa State University Digital Repository, 2013.
- [46] G. Zonfrillo, I. Giovannetti, M. Manetti, *Meccanica* 43 (2008) 125-131.
- [47] A. International, *Alloy Phase Diagrams*, Cu (Copper) Binary Alloy Phase Diagrams, 1992, pp. 2.167-162.182.
- [48] A. Kimura, R. Kasada, N. Iwata, H. Kishimoto, C.H. Zhang, J. Isselin, P. Dou, J.H. Lee, N. Muthukumar, T. Okuda, M. Inoue, S. Ukai, S. Ohnuki, T. Fujisawa, T.F. Abe, *Journal of Nuclear Materials* 417 (2011) 176-179.



- [49] P. Dou, S. Jiang, L. Qiu, A. Kimura, *Journal of Nuclear Materials* 531 (2020).
- [50] I. Barin, *Thermochemical properties of inorganic substances* [by] I. Barin [and] O. Knacke. With a pref. by O. Kubaschewski, Berlin, New York, Springer-Verlag, Berlin, New York, 1973.
- [51] I. TexSEM Laboratories, *Specimen Preparation for Electron Backscatter Diffraction (EBSD) Analysis*, in: EDAX (Ed.) 2016.
- [52] J. Schindelin, I. Arganda-Carreras, E. Frise, V. Kaynig, M. Longair, T. Pietzsch, S. Preibisch, C. Rueden, S. Saalfeld, B. Schmid, J.-Y. Tinevez, D.J. White, V. Hartenstein, K. Eliceiri, P. Tomancak, A. Cardona, *Nature Methods* 9 (2012) 676-682.
- [53] *Standard Test Methods for Determining Average Grain Size*.
- [54] R.L. Whitesell, I.E. Anderson, E.A. Rinko, E.M.H. White, T.E. Prost, T. Eden, T.A. Palmer, *Results of experiments with cold spray deposition of Fe-based ODS alloys using as-atomized spherical GARS powder.*, Powdermet 2019, Metal Powder Industries Federation APMI International, Phoenix, AZ, 2019.
- [55] A. Vardelle, C. Moreau, J. Akedo, H. Ashrafizadeh, C.C. Berndt, J.O. Berghaus, M. Boulos, J. Brogan, A.C. Bourtsalas, A. Dolatabadi, M. Dorfman, T.J. Eden, P. Fauchais, G. Fisher, F. Gaertner, M. Gindrat, R. Henne, M. Hyland, E. Irissou, E.H. Jordan, K.A. Khor, A. Killinger, Y.-C. Lau, C.-J. Li, L. Li, J. Longtin, N. Markocsan, P.J. Masset, J. Matejcek, G. Mauer, A. McDonald, J. Mostaghimi, S. Sampath, G. Schiller, K. Shinoda, M.F. Smith, A.A. Syed, N.J. Themelis, F.-L. Toma, J.P. Trelles, R. Vassen, P. Vuoristo, *Journal of Thermal Spray Technology* 25 (2016) 1376-1440.
- [56] B. Maier, M. Lenling, Y. Hwasung, G. Johnson, S. Maoy, K. Sridharan, *Nuclear Engineering and Technology* 51 (2019) 1069-1074.
- [57] N. Gao, M.J. Starink, T.G. Langdon, *Using differential scanning calorimetry as an analytical tool for ultrafine grained metals processed by severe plastic deformation*, vol 25, 2009, pp. 687-698.
- [58] I.E. Anderson, R.L. Terpstra, J.A. Cronin, R.S. Figliola, *Advances in powder size control and ultrafine powder production by gas atomization*, 3rd International Conference on Spray Deposition and Melt Atomization and ICSF VI, 6th International Conference on Spray Forming, SDMA, Universitat Bremen, Germany, 2006, pp. 1-14.
- [59] W. Wong, P. Vo, E. Irissou, A.N. Ryabinin, J.G. Legoux, S. Yue, *Journal of Thermal Spray Technology* 22 (2013) 1140-1153.
- [60] V.N.V. Munagala, V. Akinyi, P. Vo, R.R. Chromik, *Journal of Thermal Spray Technology* 27 (2018) 827-842.

- [61] R. Rokni, S. Nutt, C. Widener, V. Champagne Jr, R.H. Hrabe, *Journal of Thermal Spray Technology* (2017) 1-48.
- [62] J. Skiba, M. Kulczyk, W. Pacha, J. Smalc-Koziorowska, M. Kubis, M. Wroblewska, *Journal of Nanomedicine & Nanotechnology* 9 (2018).
- [63] J. Ritherdon, A.R. Jones, I.G. Wright, *Materials science forum* 360-362 (2001) 217-222.
- [64] R. Wawszczak, A. BACZMANSKI, M. MARCISZKO, M.X. WRÓBEL, T. Czeppe, K. SZTWIERTNIA, C. Braham, K. BERENT, *Materials Characterization* 112 (2016) 238-251.
- [65] C.F.V. Industries, *Instruction Manual*, Serial #: HP-2820, Model #: HP-4x8-G-G-VPO4-A-16, vol 1, Prepared for Ames Laboratory, December 1991.
- [66] C.F.V. Industries, *Instruction Manual Supplement: Component Maintenance and Instruction Manuals*, Serial #: HP-2820, Model #: HP-4x8-G-G-VPO4-A-16, vol 2, Prepared for Ames Laboratory, December 1991.
- [67] P.R. Brewin, O. Coube, P. Doremus, J. Hayward Tweed, *Modelling of Powder Die Compaction*, Springer Science & Business Medi, 2007.

## APPENDIX. STANDARD OPERATING PROCEDURE FOR CENTORR HOT PRESS

### Introduction

The following SOP describes operations for generating fully dense powder compacts from GARS CR-200 and CR-204 Fe-ODS precursor powders under vacuum using the Centorr Hot Press Furnace located in 150 MD. This document was generated as a reference to compile various sources of information for this furnace into one place. Consequently, some information listed in the instructions here may overlap that existing in other documents. The existing documents are listed as references or as appendices to this SOP. Users should read the Centorr Users' Manual [65] and Supplement material [66] for more information about operating this furnace. Print copies of these manuals can be found in the binder next to the press in 150MD. This SOP describes the steps followed by Rebecca Fer for her M.S. thesis work, **pressing under vacuum only. If pressing under inert gas is desired, please refer to the Centorr User's Manual [65].** She hopes that this document will aid future users of this furnace.

### Important Notes:

Maximum operating temperature of this furnace is 1650°C in inert gas (Ar, N<sub>2</sub>, He) and vacuum.

Maximum pressing force: 5 tons

**\*\*Please note:** Centorr documentation for this furnace states the system was designed for application of 20 ksi on a ½" diameter sample, but as of 2/16/2005 this had never been achieved without die failure. The maximum pressure successfully applied on ½" diameter samples was 12 ksi (~83 MPa)**\*\***

Thermocouple: Type "C" W5%Re/W25%Re thermocouple with moly sheath, 1/8" (3.2 mm) diameter by 8" (204.0 mm) long

\*\* Please note: The top ram on the Centorr Press as of 6/23/2020 is *not* original to the Centorr machine. It is a lower quality graphite, has a larger diameter than that provided by Centorr, and has a machined ½” diameter hole in its center. *If you plan to use a ¼” or ½” diameter top punch, you will need a machined platen to transfer force from the top ram to your top punch.* If you do not use a platen, pressure may not be applied to your punch. Check the top ram before use for a hole in the center. \*\*

### **Die Set Requirements**

Centorr reports the Hot Press (HP) hot zone as cylindrical 4” x 8” in the furnace chamber, but also recommends using only a 2” diameter by 2” tall die set as the “usable size” [65]. Consequently, users should limit their die set dimensions to the usable size. Graphite dies, pushrods, and TZM pushrods are to be used in the press. For pushrods <0.5” in diameter, it is recommended to use TZM or stronger alloys to avoid breakage. The die will need to be lined with a non-reactive material such as hard fired alumina or boron nitride (BN) to avoid carbide formation and microstructure contamination with the GARS alloys. Ta sheet disks may also be used to line punch ends without diffusing into the GARS powder to form undesirable contamination.

### **Graphite Requirements**

Low grades of graphite cannot be used for load bearing elements at high temperatures and under the applied pressures of this furnace. High density graphite, such as Poco graphite grade HDP-1 is preferred and was purchased from Entegris Inc. (Decatur, TX) in April of 2020. Users might also visit [www.poco.com](http://www.poco.com) to find a vendor for this graphite.

The following elements will be needed for generating pressed samples:

1. Graphite bottom punch

The following reference tables should be used to calculate the maximum pressure a die can withstand, and the corresponding applied pressure as read in psi on the HP digital pressure gauge. The following equation can be used to determine the maximum internal pressure,  $p_{i,max}$  the die can withstand based on the geometry of the die radii,  $C_{ti}$ , and the tensile strength of the die material,  $\sigma_T$  [67]. Pre-calculated  $C_{ti}$  ratios are given in table A1.

Where  $C_{ti}$  given in Table 1 is given by Equation 13 [68]:

Table A1: Die wall radius ratios for  $C_{ti}$

[illegible]

The maximum internal pressure,  $p_{i,max}$ , is equal to the negative of the maximum radial stress,  $\sigma_{R,max}$ , that can be applied to the die before failure. Please note: This die pressure calculation does NOT account for any factor of safety. The necessary applied stress,  $\sigma_a$ , to reach this maximum pressure is then found by calculating the hydrostatic stress component (Equation 14) [67].

$$\sigma_a = 3p_{i,max} - 2\sigma_{R,max} \quad \text{Equation 14 [67]}$$

The desired applied pressure,  $\sigma_a$ , should be used to find the corresponding HP Line Pressure gauge reading in Table A2. The gauge reads the line pressure, NOT the applied force. To calculate the force, the line pressure is multiplied by the effective area of the actuator, 6.5 in<sup>2</sup> [65].

Table A2: Applied Pressure vs. HP Line Pressure Gauge

Applied Pressure on Sample		Line Pressure (PSI) for Circular Die Diameters (inch)	
Mpa	PSI	0.25	0.5
0.0	0	-	-
6.9	1000	8	30
13.8	2000	15	60
20.7	3000	23	91
27.6	4000	30	121
34.5	5000	38	151
41.4	6000	45	181
48.3	7000	53	211
55.2	8000	60	242
62.1	9000	68	272
68.9	10000	76	302
75.8	11000	83	332
82.7	12000	91	362
89.6	13000	98	393
96.5	14000	106	423
103.4	15000	113	453

### Vacuum System Operation

V1 – high vacuum valve

V2 – Roughing valve

V3 – Backing valve

Chamber admission: Black knob on left side of furnace chamber, as shown in schematic of figure A1.

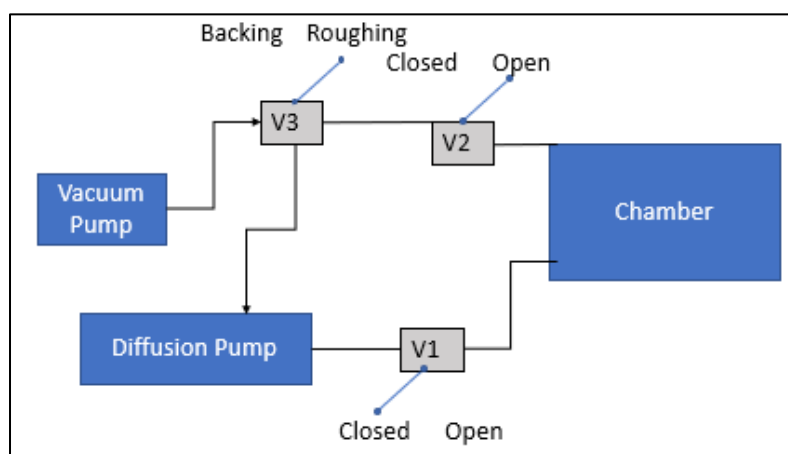


Figure A1: Schematic of vacuum system for Centorr Hot Press

### Opening Furnace Chamber

1. V1, V2 closed, V3 to backing. Chamber admission valve closed
2. If chamber pressure not equalized backfill the chamber:
  - i. open Ar tank main valve
  - ii. Open Ar tank regulator flow valve (~1/2 turn or less)
  - iii. Open chamber admission valve
  - iv. Shut chamber admission valve if only backfilling chamber, leave open Ar flow.
  - v. Shut Ar main valve and regulator valve when chamber backfilled and flow no longer needed.

3. Loosen chamber door clamps
4. Open chamber door and restrain with chain
5. Clean chamber door o-ring and mating surface

### **Closing Furnace Chamber**

Initial valve conditions: V1 closed, V2 closed, V3 on backing

1. Close chamber door and tighten clamps
2. Move V3 to roughing
3. Slowly open V2, let chamber pressure reach  $10^{-2}$  Torr (gauge on control panel) before proceeding, ~30-45 min
4. Close V2
5. Move V3 to backing
6. Open V1
7. Pump overnight (usually) before pressing sample

### **Furnace Operation**

Furnace operation is covered in more detail in the Centorr provided manual for operation, and also in the accompanying Honeywell Digital Control Programmer (DCP) 700 product manual. Please read these before operating.

### **Cu and Sb Calibration**

The following “Quick Calibration” steps were used to identify the number of degrees hotter the furnace was running than what the thermocouple reading reported. Cu and Sb were selected as their melting temperatures were similar to the desired experiment temperatures, at 1083 and 631°C, respectively.



1. Using die set like one you plan to use, place a small amount of pure copper in the bottom of the die.
2. After opening furnace box, advance the bottom ram to its highest position in the furnace chamber.
3. Set crucible containing Cu on top of bottom ram. Place a small lid/covering on top of the crucible.
4. Advance the top ram to be just above - but not touching - the crucible. Make sure that clutches for both rams are in neutral position before proceeding
5. Close the furnace door and pull vacuum for 3-4 hours. Be sure to open V2 very slowly to avoid displacing the lid on the crucible.
6. Run the furnace up to 1065°C. Hold for 1 hour.
7. Turn off the furnace and allow the chamber to cool for 2 hours before opening.
8. Open the chamber and retract the top ram. Remove the crucible. Observe the state of the Cu. Grains will have grown, and the material will appear shinier.
  - a. If the Cu piece still has sharp edges, repeat steps 1-8 with a new piece of Cu, but run at 1075°C, 1080°C, etc. until melting described in step b is observed.
  - b. If the Cu piece has slightly rounded edges, melting began at that temperature. Report temperature “Calibration” in the log book as  $\Delta T$  value above/below the melting temperature of Cu.
  - c. If the Cu piece has become completely molten and melted into a pool, the melting temperature of Cu was exceeded. Repeat steps 1-8 with a new Cu piece, but reduce the temperature to 1060°C, 1055°C, etc. until melting as described in step b is observed.

## **Furnace Operation and Programming**

Detailed instructions on furnace operation and programming can be found in the DCP700 manual in the supplement supplied by Centorr [66]. A brief explanation for operation can be found in the Centorr manual as well but is not complete [65].

### **Die Pressing**

#### **Loading and Unloading Samples**

To load the die into the furnace chamber, insert the small ½” insert on the bottom punch (or spacer, if using) into the mating hole on the bottom graphite hot rod. Note that, contrary to the drawings provided by Centorr, the graphite pedestal which was to allow for hot ejection must not be used. Poor design on Centorr’s part does not allow this feature to be used; the die support fails very easily which leads to breakage of the die as well as other components.

Once the die is in place, bring the top ram down until slight pressure is applied to the die (20-30 psi), i.e. until it is just touching. Be sure to read the Centorr and Enterpac instruction manuals and also see section 5.2 for instructions for hydraulic system operation.

### **Hydraulic System Operation**

The Enterpac system is located to the right of the HP and a picture of this system is in figure A2.

To operate:

1. Flip switch to “RUN”
2. Push lever to the right to engage system
3. Adjust the position of the top or bottom ram with the corresponding clutch. Pushing a clutch lever to the right will retract the ram (release pressure on sample), and to the left will advance its position (compress sample). Displacement of the top ram can be measured with the linear displacement reader on the top left of the HP furnace box. Be sure to zero out displacement or

record initial displacement before starting experiments. Move clutch arms slowly! The rams move suddenly.

4. Adjust system pressure by turning pressure control bolt clockwise or counterclockwise.

Pressure reads on the digital pressure gauge on the top right of the HP furnace box in PSI.

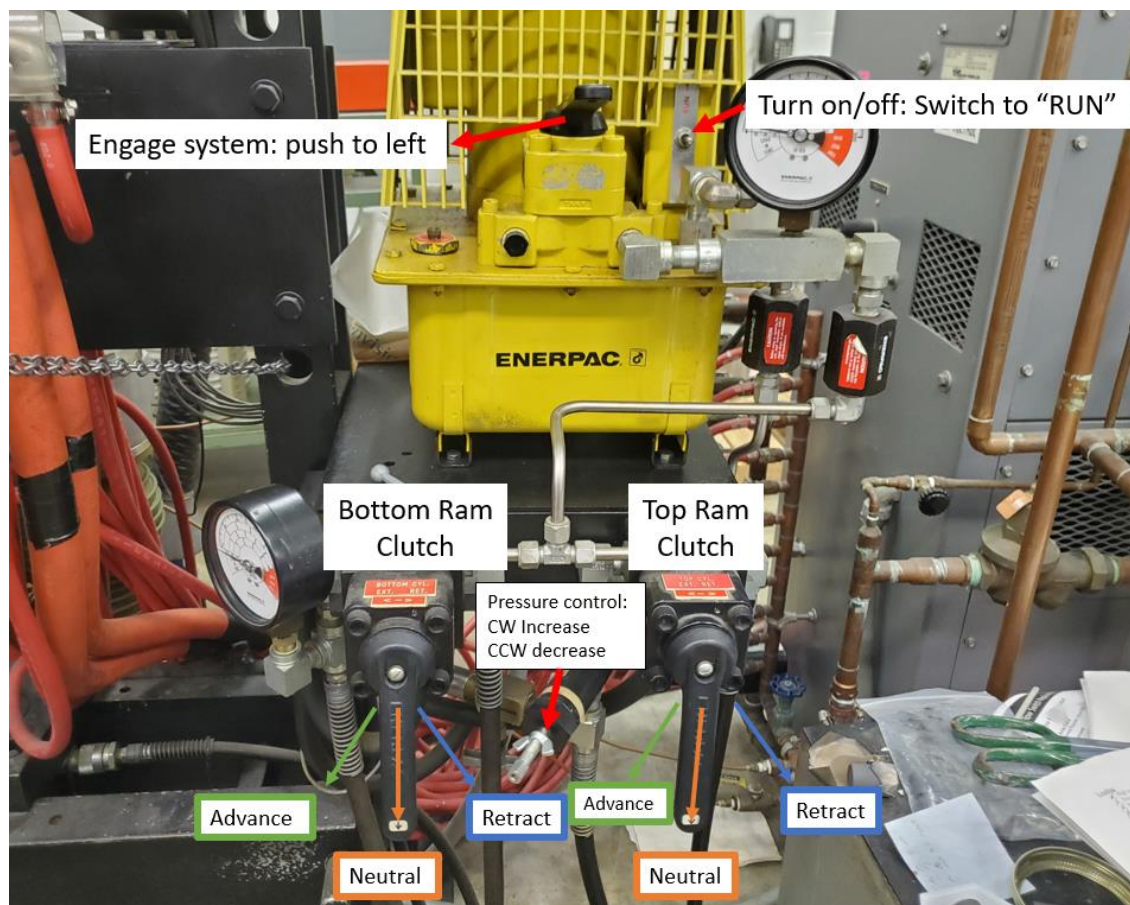


Figure A2: Enterpac Hydraulic System

### Alignment and Troubleshooting

Correct alignment of the rams is absolutely necessary to achieve dense samples and to avoid breaking die components. The following figures were provided by Centorr to show misaligned and correctly aligned top and bottom ram assembly (Figure A3).

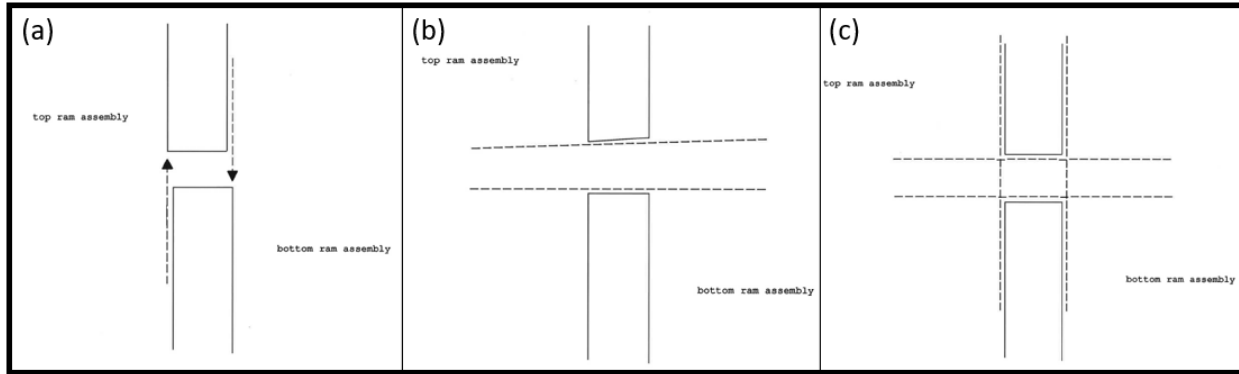


Figure A3: (a, b) Incorrect ram assembly showing non-concentric alignment (a) and non-parallel ram surfaces. (c) Correct hot rod alignment

There is a Centorr provided alignment tool, shown at right (Figure A4), that can be used to align the hot rods before the graphite rams have been attached. It has machined depressions in either end for the hot rods to sit in when they are properly aligned. If the hot rods are aligned properly, then the graphite rams should also align properly (as in (c) in figure A3) if Centorr provided rams are used.

Within the documents provided by Centorr [65, 66] the only information provided on ram alignment is provided on page 11 [65], with instructions on hot rod installation (Figure A5). Because the alignment of the rams is controlled by the hot rods – aka the steel rods outside of the furnace chamber, it is unlikely that the rams will be unaligned. However, if the press has been moved or the graphite studs or rams have recently been replaced, it is recommended to verify the alignment using the provided tool.



Figure A4: Centorr provided ram alignment tool

**WARNING:** It is extremely important that the top and bottom hot rods be aligned precisely -- even a small misalignment during pressing can destroy hot zone components.

If the above test shows the top and bottom rams to be misaligned, the cold rods and bellows have shifted during shipment and will require some re-adjustment. Contact CENTORR for details.

Figure A5: Warning from Centorr manual reiterating the importance of proper ram alignment